IDENTIFICATION AND CHARACTERIZATION OF GENES INVOLVED IN SUBCELLULAR LUMEN FORMATION IN THE *DROSOPHILA* LARVAL TRACHEAL SYSTEM

by

Oscar Eugenio Ruiz

A dissertation submitted to the faculty of
The University of Utah
in partial fulfillment of the requirements for the degree of

Doctor of Philosophy

Department of Human Genetics

University of Utah

August 2012

The University of Utah Graduate School

STATEMENT OF DISSERTATION APPROVAL

The dissertation of **Oscar Eugenio Ruiz**

has been approved by the following supervisory committee members:

Mark Metzstein	, Chair	**4/16/2012** Date Approved
Carl Thummel	, Member	**4/16/2012** Date Approved
Charles Murtaugh	, Member	**4/16/2012** Date Approved
Gillian Stanfield	, Member	**4/16/2012** Date Approved
Erik Jorgensen	, Member	**4/16/2012** Date Approved

and by **Lynn Jorde** , Chair of

the Department of **Human Genetics**

and by Charles A. Wight, Dean of The Graduate School.

ABSTRACT

A common pattern in systems designed to transport liquids and gases, such as the vascular and respiratory systems, is the use of branched tubular structures to create a network that interconnects the entire body. The cellular cues required for generating these complex networks are not well understood. To identify components involved in generating branched tubular networks we are studying the *Drosophila melanogaster* tracheal (respiratory) system. The *Drosophila* larval tracheal system is composed of approximately 10,000 interconnected tubes which serve to transport oxygen and other gases throughout the body. The branching and tubulogenesis (the formation of an open space or lumen that extends throughout the length of a branch to make it a tube) seen during *Drosophila* tracheal system development may parallel similar processes seen in other organisms. The molecular and genetic tools available for *Drosophila* provide us an excellent opportunity to identify factors required in branching and lumen formation.

A forward genetic screen of the X chromosome was conducted to isolate lethal mutations affecting branching and lumen formation in tracheal terminal cells of *Drosophila*. Tracheal terminal cells are specialized cells that undergo subcellular branching and tubulogenesis, and are responsible for transporting gases and exchanging gases in hypoxic tissues. Thirty-two lines with mutations affecting different aspects of branching and lumen formation were identified. Of these 32 we focused on five

lines in which tracheal terminal cells undergo essentially normal branching, but are unable to generate a functional lumen. These mutants have been mapped to discrete genetic intervals using a recombination mapping strategy. The mapping has been further refined for two of these five lines by using a combination of single nucleotide polymorphisms (SNP) and P-element recombination frequencies allowing us to identify a small number of candidate genes for each of these mutations. Additionally, for one of these mutants we have identified the causative gene as *Zpr1* (*Zinc-finger protein 1*), an evolutionarily conserved protein characterized by two C4 zinc fingers and two conserved homology domains.

This thesis is dedicated to my wife and daughter.

TABLE OF CONTENTS

LIST OF TABLES

LIST OF FIGURES

ACKNOWLEDGEMENTS

I would like to first thank my advisor Mark Metzstein for both his mentorship and friendship. His mentorship has been more than I could have ever asked for. He has been instrumental in my development and training as a scientist. Mark has always had high expectations and has showed me how to think like a scientist. He is the quintessential scientist and I will forever aspire to be as great a scientist as he is. For all of the knowledge that Mark has shared with me during our time in lab together I am most appreciative of his advice and help with life in general. His door has always been open for scientific discussions, but maybe more importantly, he has always been there to give encouragement and talk about life.

I would also like to thank my committee, Charlie Murtaugh, Gillian Stanfield, Erik Jorgensen, and Carl Thummel. They have been very helpful in guiding and helping me focus my project during committee meetings, as well as being invaluable in journal clubs and research in progress meetings. They have also been helpful outside of our regular interactions, and their doors have always been open for me. I can say that every one of them has personally helped me in one way or another during my graduate career.

I would like to thank Dr. Gerardo Flores Gutierrez who was one of my master's thesis advisors. He always encouraged me to continue my education and helped guide me to the area of genetics. I will always be in debt to you and your family.

I would like to thank the entire Metzstein lab, you have all played a huge role in my life here in Utah. Despite our many heated discussions and disagreements over the years I consider all of you my dear friends and look forward to seeing you succeed in life. You have been my surrogate family here in Utah and for that the entire Ruiz-Berman household thanks you and loves you.

I want to thank my entire family for their support during this tremendous rollercoaster ride called graduate school. Thank you for your love and understanding throughout my life. I would like to especially thank my mother and father, Aide and Eugenio, for teaching me the importance of an education, as well as showing me that hard work and determination are the keys to success. Both of you are my heroes and are the reason for all of my success in life. I love you and thank you for all the knowledge and love you have given me.

Lastly, and most importantly, want to thank my wife Karen, and my daughter Frida. I am happy to say that you are the best wife and daughter that anyone could ever have. Thank you for allowing me to be a part of your lives. You are the best and most important parts of my life. I thank you for being there to celebrate our successes, and love you for being there for during hard times. I thank you for helping me get my Ph.D., although the diploma will have my name on it, it belongs to you just as much as it belongs to me. I love and thank both of you with all my heart and look forward to the rest of our adventurous lives.

To the many other people that have helped me along the way, thank you.

CHAPTER 1

INTRODUCTION

A common architecture in systems designed for the transport of liquids and gases, such as the vascular and respiratory systems, is the use of branched, tubular structures to create a network that interconnects the entire organism. To establish these complex networks, groups of cells must undergo a variety of morphological and cellular changes that result in the assembly of the functional fully-interconnected tubular network. Despite the widespread use this common structural design, the cellular and molecular mechanisms required for establishing these transport networks are not well understood. To gain insight into the genes required to achieve the morphological and cell rearrangements used for generating interconnected tubular networks we are studying the development of the larval tracheal (respiratory) system of the fly *Drosophila melanogaster*. The larval tracheal system in *Drosophila* is a network of thousands of interconnected tubes that serve to transport oxygen and other gases throughout the body.

Development of the *Drosophila* embryonic tracheal system

The construction of the *Drosophila* tracheal system begins early in embryogenesis, when 10 bilateral segmentally repeated groups of ~80 cells within the embryonic ectoderm are fated to become tracheal tissue through the expression of the

bHLH-PAS domain transcription factor *trachealess* (Samakovlis et al., 1996A and Wilk et al., 1996*)*. Expression of *trachealess* is followed by the invagination of these tracheal placodes to form tracheal sacs. Soon after formation, each sac undergoes a series of coordinated and stereotyped branching and tubulogenesis events, starting at mid-embryogenesis. These early outgrowth events are mediated through the secretion of the FGF ligand, Branchless (Bnl) by cells surrounding the tracheal sacs (Sutherland et al., 1996). Tracheal cells respond to these signaling cells through the ligand-dependent activation of the tracheal specific FGF receptor Breathless (Btl) (Lee et al., 1996). Activation of the Btl receptor in tracheal cells results in the coordinated and stereotypical branching pattern that forms the embryonic tracheal system. Within the embryonic tracheal system, specialized cells at the ends of branches called terminal cells are specified through the expression of the transcription factor *blistered*, the *Drosophila* homolog of the mammalian serum response factor (Guillemin et al., 1996).

Development of the *Drosophila* larval tracheal system

During larval development a second wave of Bnl signaling from hypoxic cells induces additional branching and outgrowth in terminal (Jarecki et al., 1999). Once the initial branching required for tracheal cells to reach their target tissue is completed, the tracheal terminal cells must undergo a subsequent lumenogenesis step to create the hollow space, or lumen, through which the gas must travel (Reviewed in Ghabrial et al., 2003). This lumen formation step is cellularly distinct from the tubes that form during the development of the embryonic tracheal system. The embryonic tracheal system is comprised of two basic tube types. The first type (primary branches) of tube in the

tracheal system are multicellular structures that are comprised of a single layer of epithelial cells wrapped into a tubular shape (Figure 1.1). Because primary branches arise through migration and intercalation of small clusters of cells that can organize themselves into tubes, cross section of these branches reveals many intercellular junctions that provide an airtight seal for the lumen (Samakovlis, et al., 1996A). Secondary branches are unicellular tubes that are made from extended individual cells that wrap around the long axis of the cell to create a single autocellular junction, or seam, which runs the entire length of the cell (Samakovlis, et al., 1996B).

The last tube type in the tracheal system is comprised by terminal cells. Terminal cells, where gas exchange between the tracheal system and hypoxic tissues takes place (Figure 1.2), are characterized by having a completely subcellular lumen with no cellular junctions. Also, in contrast to the entirely stereotyped branching and lumen formation observed during early tracheal morphogenesis, terminal cell branch outgrowth is a dynamic process that is mainly controlled by the extent of hypoxia a target tissue is experiencing (Jarecki, 1999 and Ghabrial and Krasnow, 2006). This final growth ensures that terminal cells that provide oxygen to hypoxic tissue will have sufficient branches that can be utilized for efficient gas exchange.

Lumen formation

The establishment of a functional lumen is an important step in achieving the interconnectivity required for efficient transport of liquids or gases in branched tubular networks. Despite the wide variety of branched tubular networks seen in nature, it is thought that the organization of most tubular structures involves a layer of polarized cells

in which the apical surface of the cells faces the lumen. Groups of cells can undergo a variety of morphological and cell rearrangements to generate a tube with a functional polarized apical lumen. The primary branches in the *Drosophila* tracheal system are created through a process called wrapping (Lubarsky and Krasnow, 2003). In this process a polarized epithelial sheet curls until its edges meet, forming a seal. In this case, the apical surfaces of all cells encompassing this sheet now face the hollow end or lumen of this tube, and the basal surface is exposed to the inside of the animal (Shim, et al., 2001). The secondary branches in the *Drosophila* tracheal system employ a type of tube formation process called budding. As in wrapping, this type of tube also arises from a polarized epithelial sheet. In this case, movement of cells in an outward direction from the sheet creates the tubular structure. The creation of tubes through a wrapping or budding process depends on a previously established polarized epithelial sheet of cells. Tubes can also arise from unpolarized cells cells in a processes called cavitation, cord hollowing and cell hollowing (Lubarsky and Krasnow, 2003). The final products of these processes are structurally similar to the tubes created by wrapping or budding, in that they all result in the creation of a polarized tubular structure. In cavitation and cord hollowing, a hollow structure arises from inside a mass of unpolarized cells through either the specific elimination of cells (cavitation) or cell movement and rearrangements (cord hollowing) (Lubarsky and Krasnow, 2003). All of the previously described tube formation processes require the use of groups of cells to establish a lumen.

In contrast to these multicellular tubes, *Drosophila* terminal cells are able to create a completely subcellular lumen. To create a such a lumen, terminal cells employ a process called cell hollowing. In cell hollowing, a single cell establishes a lumen in the

absence of cell-cell junctions or positional cues from neighboring cells. The specific instructional components involved in the creation, maintenance and remodeling of a completely subcellular lumen are not well characterized.

The observation that most tubular structures display polarized apical lumen has led to the idea that although tubular structures can be created through distinct morphological and cell rearrangements, all seem to depend on a similar set of cellular cues. The first of these cellular cues involves the establishment of apical and basal polarity. This early polarization step ensures that all cellular components involved in lumenogenesis target the future lumen to the same location. Although this had been proposed as an important step in the creation of a subcellular lumen, the specific role of molecules known to effect the establishment of apical/basal polarity in various cell types has not been described in tracheal terminal cells. Recent work has shown that components of PAR-polarity complex are required for proper terminal cell branching and lumen formation (Jones and Metzstein, 2011). This suggests that terminal cells must establish an apical/basal identity in order for development to occur. Recent evidence also suggests that once polarized, cells may utilize changes in the localization of different cytoskeletal components, such as microtubules, to establish a scaffold upon which the lumen can be built (Schottenfeld-Roames and Ghabrial, 2012). The idea that a molecular scaffold must be created to establish a site for the generation of a nascent lumen has been argued from experiments showing that during the initial steps in lumen formation in cell culture experiments and the vascular development in zebrafish, vacuolar structures can be seen diffused throughout the cell, but later in the lumenogenesis process, these structures seem to fuse and coalesce to form the lumen (Kamei et al., 2006). Additional work has

shown that various components known to be involved in general vesicle trafficking also play a role in generating a functional lumen in an *in vitro* model of lumenogenesis (Bayless and Davis, 2002). More recent work has show that the GTPase Rab35 is a key regulator of lumen formation in terminal cells and that changes in its subcellular localization have striking effects on lumen growth (Schottenfeld-Roames and Ghabrial, 2012). Despite our expanding knowledge of general lumen formation, many of the components required to specifically generate a subcellular lumen remain uncharacterized.

Summary

In this thesis, I present my studies on mapping and identifying lethal mutations on the *Drosophila* X chromosome that have an affect on lumen formation in tracheal terminal cells. In Chapter 2, I describe the mapping strategies and data we obtained by mapping five genes that are required for lumen formation and one gene that is required for proper branch/lumen coordination obtained from a previously conducted screen. In Chapter 3, I describe my molecular studies on one of these lumenless genes *Zpr1* (*Zinc-finger protein 1*) and the role that it plays in mediating RTK (receptor tyrosine kinase) signaling in the tracheal system. In Chapter 4, I analyze proteins that have been previously shown to interact with Zpr1 by cell culture experiments, and test their specific roles in the development of the tracheal system of *Drosophila*. Lastly, in Chapter 5, I describe the use of the *Drosophila* larval tracheal system as a model for the study of the cerebral cavernous malformations, a human genetic disease characterized by defects in vascular tube formation in the brain.

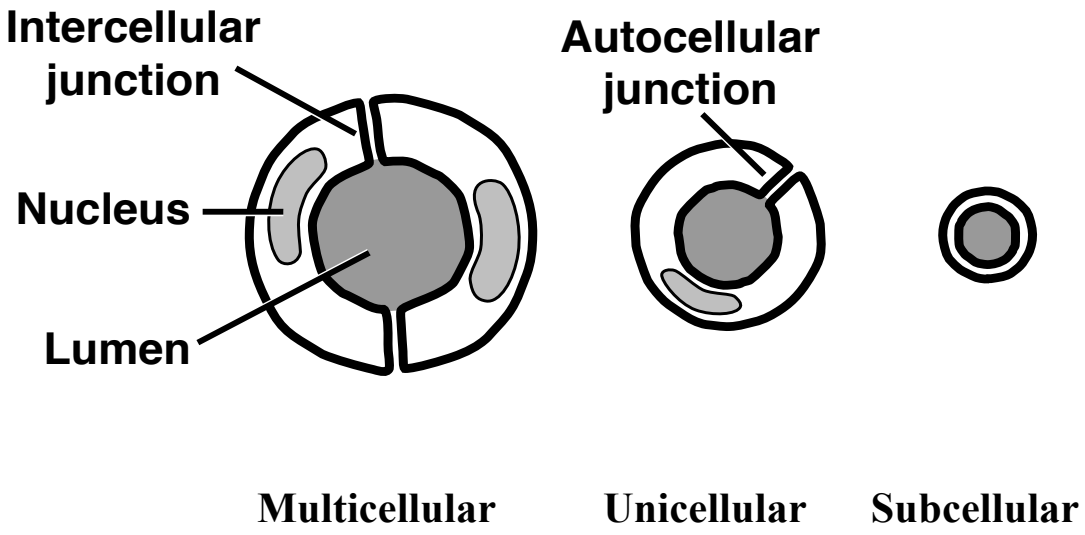

Figure 1.1. Cross-section of the three types of tubes that comprise the *Drosophila* larval tracheal system. Multicellular tubes contain multiple cell-cell junctions. Unicellular tubes are made from single cells and contain a single autocellular junction. Terminal cells generate branches that contain a completely subcellular lumen, and do not contain autocellular junctions. Modified from: Samakovlis et al., 1996A.

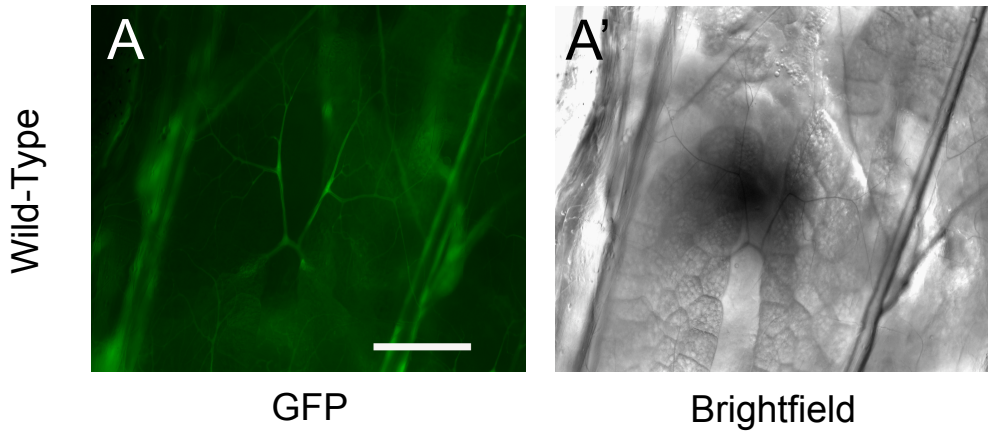

Figure 1.2. ***Drosophila*** **larval tracheal terminal cells**. Branching patterns of terminal cells can be assayed by cytoplasmic GFP-labeling (A). Subcellular gas-filling in terminal cells can be visualized with brightfield optics (A'). Scale bar 200μm.

References

Bayless, K.J. and G.E. Davis (2002). The Cdc42 and Rac1 GTPases are required for capillary lumen formation in three-dimensional extracellular matrices. J Cell Sci *115*, 1123-36.

Ghabrial, A., et al. (2003). Branching morphogenesis of the Drosophila tracheal system. Annu Rev Cell Dev Biol *19*, 623-47.

Ghabrial, A. and M.A. Krasnow (2006). Social interactions among epithelial cells during tracheal branching morphogenesis. Nature *441*,746-749.

Chung S, et al. (2009). Serrano (sano) functions with the planar cell polarity genes to control tracheal tube length. PLoS Genet. *5*, e1000746

Guillemin, K., et al. (1996). The pruned gene encodes the Drosophila serum response factor and regulates cytoplasmic outgrowth during terminal branching of the tracheal system. Development *122*, 1353-62.

Jarecki, J., E. Johnson, M.A. Krasnow (1999). Oxygen regulation of airway branching in Drosophila is mediated by branchless FGF. Cell *99*, 211-20.

Jones, T. and M. Metzstein (2011). A novel function for the PAR complex in subcellular morphogenesis of tracheal terminal cells in Drosophila melanogaster. Genetics *189,* 153-64.

Kamei, M., et al. (2006). Endothelial tubes assemble from intracellular vacuoles in vivo. Nature *442*, 453-6.

Lee, T., et al. (1996). Regulated Breathless receptor tyrosine kinase activity required to pattern cell migration and branching in the Drosophila tracheal system. Genes and Development *10*, 2912-2921

Levi, B.P., A.S. Ghabrial and M.A. Krasnow (2006). Drosophila talin and integrin genes are required for maintenance of tracheal terminal branches and luminal organization. Development *133*, 2383-93.

Lubarsky, B. and M.A. Krasnow (2003). Tube morphogenesis: making and shaping biological tubes. Cell *112*, 19-28.

Samakovlis, C., et al. (1996). Development of the Drosophila tracheal system occurs by a series of morphologically distinct but genetically coupled branching events. Development *122*, 1395-407.

Samakovlis, C., et al. (1996). Genetic control of epithelial tube fusion during Drosophila tracheal development. Development *122*, 3531-6.

Schottenfeld-Roames J, Ghabrial AS. (2012). Whacked and Rab35 polarize dynein-motor-complex-dependent seamless tube growth. Nat Cell Biol. March 11.

Shim, K., K. Blake, J. Jack, and M.A. Krasnow. (2001) The Drosophila ribbon gene encodes a nuclear BTB domain protein that promotes epithelial migration and morphogenesis. Development *128*, 4923-4933.

Sutherland, D., et al. (1996). branchless encodes a Drosophila FGF homolog that controls tracheal cell migration and the pattern of branching. Cell *87*, 1091-101.

Wilk R., Weizman I. and Shilo BZ. (1996). trachealess encodes a bHLH-PAS protein that is an inducer of tracheal cell fates in Drosophila. Genes and Development *10*, 93-102

CHAPTER 2

MAPPING AND IDENTIFICATION OF MUTATIONS AFFECTING GAS-FILLING IN *DROSOPHILA* TRACHEAL TERMINAL CELLS

Introduction

The *Drosophila* larval tracheal system provides an excellent opportunity to identify novel genes involved in the establishment of branched tubular networks. Branched tubular networks such as the vascular and respiratory systems are a common organ architecture that function to transport liquids and gases. To identify components involved in generating these types of branched tubular networks, a forward genetic screen of the *Drosophila* X chromosome aimed at identifying lethal mutations that have defects in tracheal terminal cell development was performed previously (Metzstein and Krasnow, unpublished). Terminal cells are specialized cells that undergo subcellular branching and tubulogenesis, and are responsible for transporting gases and exchanging gases in hypoxic tissues (Guillemin et al., 1996; Jarecki et al., 1999). The screen identified 32 lines with mutations affecting different aspects of branching and lumen formation. Of these 32, we focus here on five lines in which tracheal terminal cells undergo essentially normal branching, but are unable to generate a functional lumen, and one line which displays a branch/lumen coordination defect. We have mapped five of these mutants to

discrete genetic intervals using a visible marker recombination mapping strategy. The mapping has been further refined for two of these five lines by using a combination of single nucleotide polymorphisms (SNP) and transposable element (TE) markers and has allowed us to identify a small number of candidate genes for each of these mutations.

Materials and methods

Identification of lethal mutations on the *Drosophila* X chromosome affecting lumen formation in tracheal terminal cells

EMS-generated lethal mutations on the *Drosophila* X chromosome were identified by the inability of homozygous mutants to live to the wandering L3 stage (Metzstein and Krasnow, unpublished results). Individual lethal mutations were then assayed for terminal cell defects by using clonal analysis. For all clonal analysis, we used the mosaic analysis with a repressible cell marker (MARCM) system to generate positively marked, homozygous mutant cells within heterozygous animals (Lee and Luo, 1999). Briefly, mutant X chromosomes containing the Flippase recombination target site (FRT) FRT^{19A} were placed in *trans* to a wild-type chromosome containing the same FRT (Xu and Rubin, 1993). The clone generating stock also contains the tracheal-specific driver *btl-GAL4* a *UAS-GFP* reporter as well as the repressor of GAL4-mediated transcription *btl-Gal80* (Shiga et al., 1996). We then induced recombination by heat shocking 0-6 hour old embryos containing the heat-shock inducible flippase $hsFLP^{122}$ at 38° for 45 minutes. This heat shock induces the expression of the flippase which mediates recombination between FRT sites and generates homozygous mutant cells that are positively marked by GFP. For all clonal experiments control chromosomes are

FRT^{19A}. MARCM analysis was done on the following X-linked lethal alleles, *13A*, *31ZZ*, *33UU*, *5A*, *17CC* and *25C*. The tracheal specific promoter *breathless* (*btl*) was used to positively mark homozygous mutant cells in the following stock: *y w btl-Gal80, FRT*^{19A}, *hsFLP*^{122}; *btl-Gal4, UAS-GFP* (Metzstein and Krasnow, unpublished results).

Mapping lethal mutations on X chromosome

The lethality associated with mutations on the X chromosome was mapped by first crossing each lethal X chromosome to an X chromosome carrying multiple visible markers (*sc cv ct v g*^{2} *f FRT*^{19A}). Trans-heterozygous F1 females were mated to males of genotype *Df(1)64c18, g*^{1} *sd*^{1}*/Dp(1;2;Y)w*$^{+}$. Viable hemizygous male progeny from this cross were scored for the visible markers (Figure 2.1). Males used in the F1 cross contained a genomic duplication of the *white* gene allowing us to identify recombinants occurring between the *v* and *g* genes (which are eye color markers). This strategy allowed us to map each mutation to a discrete genetic interval on the X chromosome.

Identifying single nucleotide polymorphisms (SNPs) in recombinant animals

Our initial mapping strategy allowed us to place individual lethal mutations within specific genetic intervals. To further refine the location of each mutation we used our recombination strategy to identify viable male flies that had undergone a single recombination event within the genetic interval previously identified as containing the lethal allele. The position of the single recombination event from the original viable marker was determined by using single nucleotide polymorphisms (SNPs) which differed

between the lethal containing chromosome and the multiply-marked chromosome. To identify these SNPs we first designed ~1000bp PCR amplicons (using Primer 3) within intergenic regions spanning the interval between the visible markers that contained the lethal of interest. After the amplicon PCR conditions were optimized for each primer pair, the amplicons from both marked and mutant chromosomes were sequenced and the sequences compared for differences including SNPs and InDels. We then examined if the polymorphisms altered restriction digest enzyme sites in the amplicons, and if so we used restriction digest of amplicons for genotyping. For SNPs identified in which restriction digest enzyme sites were not altered, we used sequencing to type the markers. For mutant lines *33UU* and *31ZZ* (both of which mapped between *ct* and *v*) we identified 22 informative marker amplicons, and used each to map the relative position of each lethal mutation (Table 2.1).

Mapping lethality with respect to transposable element insertions

To further refine the position of the lethal mutation associated with mutant lines within the *ct* and *v* genetic interval, we employed a meiotic recombination mapping strategy similar to the previous mapping experiments, but in this case we mapped the position of the lethal mutation with respect to transposable element (TE) insertions. Fly stocks harboring single visibly marked transposable element insertions are available from various *Drosophila* stock centers. The exact genomic position for each of these transposable elements has been characterized (Table 2.2). Combining the position and the visible marker (typically a w^+ eye color or y^+ body color marker) allows for efficient identification of recombinant events close to the lethal allele. For lethal mutants that

were mapped to the *ct* and *v* genetic interval, we obtained TE lines whose location had also been mapped to the same interval, and used these lines to refine our mapping data (Table 2.2). We first produced *trans*-heterozygote females by crossing each lethal mutant line to individual TE lines. We then crossed approximately 400 of these *trans*-het F1 females to males, and scored for the absence of marker (w^+ or y^+) associated with each TE line in individual viable hemizygous male progeny. Finally, by scoring flanking genetic markers, this allowed us to map the genomic position of lethal mutation as being to the left or right of each individual TE insertion.

Candidate gene RNAi analysis

The tracheal specific *breathless* promoter was used to drive UAS-RNAi transgenes directed against individual candidate genes in the tracheal system. Lethality was assayed by using *Act5C-GAL4* to ubiquitously drive the expression of each RNAi transgene (Ito et al., 1997). Candidate genes were identified by searching FlyBase for genes located within the previously identified genomic regions whose gene ontology terms and lists of biological processes include cellular pathways thought to be involved in mediating subcellular lumenogenesis. Candidate genes tested are listed in Table 2.3.

Results

Mutations required for branching and lumen formation in *Drosophila* terminal tracheal cells

A forward genetic mosaic screen of lethal mutations on the X chromosome was conducted by using the MARCM system to generate positively (GFP) marked homozygous mutant cells in heterozygous animals. Homozygous mutant cells were then scored for tracheal branching or air-filling defects by using a combination of fluorescence microscopy and brightfield optics to visualize terminal branching patterns and air-filling, respectively. Of the 900 lines that were scored, a class of mutations, that we refer to as lumenless was identified by their inability to generate gas-filled lumens. From this lumenless class of mutants, we focused on five individual mutant lines. In addition, we examined one mutant line in which lumen formation occurred, showed a defect in branch/lumen coordination. To map and clone these six mutants, we first mapped the lethality associated with each mutation to a discrete genetic interval (Figure 2.2). For two of these mutants, we refined this interval further by using a combination of SNP mapping and mapping relative to available TE insertions.

Mutant line *5A*

Homozygous *5A* mutant cells display seemingly wild-type branching patterns, but are unable to generate a gas-filled lumen (Figure 2.3). For preliminary mapping of this mutant line, 85 individual recombinants were scored from *trans*-heterozygous females carrying the *5A* lethal chromosome. Viable recombinants placed the *5A* lethal mutation

in the genetic interval between the *cv* and *ct* genes, representing a ~1.9 Mb region of DNA. Previously, a lethal mutation affecting gas-filling in tracheal terminal cells was identified in a mutant line designated *oog (out of gas)* which also mapped to the same *cv* and *ct* interval as *5A*, and subsequently identified as a mutation in *rabconnectin-3α* (Metzstein, et al., unpublished results). To test for the possibility that *5A* may represent a new allele of *oog* we performed a complementation test. Since the *oog* mutation had been mapped and cloned, transgenic flies carrying a transgene containing the *oog* genomic locus on the 2nd chromosome were available. We crossed males of genotype *oog/Y*; *P{oog*$^{+}$*}/+* to *5A/FM7c* virgins and scored nonbalancer containing F1 females. Of the 87 *oog*/*5A* females scored, 39 were w^{+} genotype (indicating the presence of the oog^{+} transgene) and 48 were w^{-} (indicating the absence of the oog^{+} transgene). These results indicate that *5A* and *oog* are not allelic and represent mutations in distinct genes.

Analysis of the *5A* interval led us to identify candidate genes within the genetic interval (Table 2.3). We then tested the function of four candidate genes by RNAi knock-down. Of the four genes tested (*Marf*, *Pat1*, *CG3973* and *CGC*), only *Marf (mitochondrial assembly regulatory factor)* was lethal when driven by the Actin promoter, and produced a variable lumenless phenotype when driven by the tracheal specific driver *breathless*. The Marf protein is predicted to have GTPase activity and could play a role in terminal cell lumenogenesis as a regulator of vesicle trafficking and is a candidate gene for sequence analysis in the *5A* mutant line.

Mutant line *33UU*

Homozygous *33UU* mutant cells show branching defects and are unable to generate a functional lumen (Figure 2.4). For the initial mapping analysis, 88 individual recombinants were scored from *trans*-heterozygous females carrying the lethal *33UU* chromosome and the marker chromosome. Viable recombinants placed the *33UU* lethal mutation in the genetic interval between the *ct* and *v* genes, representing a ~3.2Mb interval. We refined this mapping by SNP analysis in recombinants in which a single recombination event had occurred within the *ct*-*v* interval (see Materials and Methods). A total of 99 single recombinant flies were collected from each recombination class (46 v^+ *ct* and 53 *v* ct^+) and subsequently tested for single nucleotide polymorphisms that would allow us to distinguish between the mutagenized chromosome and the chromosome used for our mapping studies. This analysis placed our mutation between SNPs XD4 and XD10 (Table 2.1), a region of ~189kb. To further refine the position of the lethal mutation associated with *33UU*, we mapped the position of the lethal mutation with respect to transposable element insertions (see Materials and Methods). Using a combination of SNPs and TE lines, described in Table 2.2, we were able to further narrow the interval containing the lethal mutation in *33UU* to a ~100kb region. During the time this data was obtained, the current version of the *Drosophila* genome assembly predicted multiple genes within this 100kb region. We obtained lines containing UAS-RNAi constructs for all these predicted genes and used these to assay gene function in the tracheal system (Table 2.3). However, tracheal terminal cells expressing any of these constructs exhibit a wild-type phenotype. Recently, this region within the *Drosophila* genome has been re-annotated to now include portions of a single 140kb gene named

megalin. The *megalin* gene encodes a low-density lipoprotein receptor and experimental evidence suggests that it may be involved in chitin-based cuticle development and endocytosis (Riedel, et al. 2011); functions which have been shown to be essential in tracheal development (Devine et al., 2005, Tonning et al., 2005). Our mapping data suggest that the causative mutation in mutant line *33UU* lies somewhere within the *megalin* gene and provides an excellent starting point for its discovery.

Mutant line *13A*

Terminal cells homozygous mutant for 13A display an inability to generate functional air-filled lumens. Fifty-nine individual recombinants were scored from trans-heterozygous females carrying the lethal *13A* chromosome and the marker chromosome. Viable recombinants placed the *13A* lethal mutation in the genetic interval between the *sc* and *cv* genes, representing a ~3Mb region. We examined the interval for possible candidate genes and used a RNAi strategy to test their function in tracheal terminal cells (Table 2.2). Of the five genes (*rala*, *cut up*, *vap33-1*, *lava lamp* and *fd3f*) assayed by RNAi using dsRNA expressed from the ubiquitous Actin promoter, all except *cut up* showed a lethal phenotype. When RNAi was performed in a tissue-specific manner using the *breathless* promoter, the gene *rala* (*ras- related protein*) was the only gene in which tracheal cells showed defects in gas-filling. The Rala protein is predicted to have GTPase activity and PDZ-binding properties and these functions may be involved in processes that may also play a role in terminal cell development (Jones and Metzstein, 2011, Schottenfeld-Roames and Ghabrial, 2012). This result now provides a reasonable candidate gene for sequence analysis in the *13A* mutant line.

Mutant line *17CC*

Eighty-six individual recombinants were scored from trans-heterozygous females carrying the lethal *17CC* chromosome and the marker chromosome. We were unable to place the lethal mutation in a specific genetic interval because no lethality was observed in the F2 generation. The source of this surprising result is that the w^+ genomic duplication used to score eye color markers in recombinant animals, also rescues the lethality of *17CC*. This allows us to place the lethal mutation associated with *17CC* in the duplicated chromosomal region. This duplication encompasses the cytological bands 2D2-3D3. We then examined the duplicated segment for possible candidate genes, and used a RNAi strategy to test their function in tracheal terminal cells (Table 2.2). Disruption of all six genes (*vinculin*, *egghead*, *syntaxin4*, *klp3A*, *CG3071* and *CG14054)* resulted in viable animals when function was assayed by RNAi using dsRNA expressed from the ubiquitous Actin promoter. Interestingly, when RNAi was performed in a tissue-specific manner using the *breathless* promoter, the gene *CG14054* showed a variable gas-filling defect. This result is intriguing, in that it suggests that *CG14054* may be solely required in the tracheal system. Follow up experiments should be aimed at confirming the degree of RNAi knockdown that is being achieved as well as a quantification of this variable defect to confirm this result. Nevertheless, *CG14054* provides an interesting gene to investigate by sequence analysis in the *17CC* mutant line.

Mutant line *31ZZ*

One hundred ten individual recombinants were scored from trans-heterozygous females carrying the lethal *31ZZ* chromosome and the marked chromosome. Viable

recombinants placed the *31ZZ* lethal mutation in the genetic interval between the *ct* and *v* genes, a ~3.2Mb region. We refined this mapping by performing SNP analysis in recombinants in which a single recombination event had occurred within the *ct*-*v* interval (See Materials and Methods). A total of 38 single recombinant flies were collected from each recombination class (8 *ct* v^+ and 30 ct^+ *v*) and subsequently tested for SNPs that would allow us to distinguish between the mutagenized chromosome and the reference chromosome used for our mapping studies. We followed this by mapping with respect to transposable element insertion sites. By combining our SNP mapping data with our TE mapping results we were able to narrow the *31ZZ* genetic interval from a ~115kb region (between the SNPs XD11 and XA37, Table 2.1) to a ~72kb region (between TE insertion *PBac{WH}-f02398* and SNP XA37). The genes included in this interval were then assayed for mutations by sequencing. A single mutation was identified in the gene *Zinc-finger protein 1 (Zpr1)*. Additional sequencing and cloning data of mutant line *31ZZ* will be discussed in the following chapter.

Initial SNP mapping placed the *31ZZ* mutation in the same genetic interval with a previously identified lethal mutation, *25C,* allowing for the possibility that these mutations may represent different alleles of the same gene. *25C* (also called *crazy lumens*) was originally identified by a lumenal over-growth and excessive gas-filling phenotype in tracheal terminal cells **(**Metzstein and Krasnow, unpublished**)**. By additional SNP and transposable element mapping we have ruled out the possibility that *31ZZ* and *crazy lumens* are allelic as we placed the mutations on opposite sides of the TE insertion *P{XP}-d06942*.

Mutant line *25C*

Previous mapping data on the *crazy lumens* mutant line had placed the causative mutation in a region between the TE insertions *KG00121* and *KG0172*. This ~65kb region encompassed 14 genes and was small enough to try to identify the causative mutation in this mutant line by sequencing. We subsequently attempted to sequence all of the genes within this region but were unable to find mutations in any of the genes for which we were able to obtain quality sequence data (Table 2.4). We were unable to obtain quality sequence data for three remaining genes, probably due to the duplicated nature of these genes. Instead, we tested for function using an RNAi approach targeted at two of the three genes. Of both assayed genes, one line displayed a strong lumenless phenotype when the RNAi construct was expressed in the tracheal system (Table 2.6). This phenotype is distinct from the lumenal overgrowth defect seen in the mutant line. Since our RNAi knock-down is likely to represent the loss-of-function phenotype the mutant line may represent a gain-of-function phenotype. These results place *CG32708* as likely to harbor the causative mutation, and present the possibility that *25C* may be a neomorphic allele of this gene. Additional sequencing and rescue experiments must be performed to identify the mutation in the *crazy lumens* mutant line, but the possibility that the distinct mutant and RNAi knockdown phenotypes may represent important allelic differences and may provide powerful genetic tools for the dissection of the molecular pathway and function of this gene.

Discussion

Mutants isolated from a forward genetic screen of the *Drosophila* X chromosome were mapped to discrete genetic intervals using a visible marker recombination mapping strategy. For some of these mutants the mapping has been further refined using a combination of single nucleotide polymorphisms and transposable element mapping. These mapping experiments have led to the molecular cloning of one mutant line 31ZZ, which will be discussed in the following chapter. Additionally specfic candidate genes were identified for the remaining lumenless class of mutant lines . In particular, the mapping data and recent re-annotation of the *Drosophila* genome provide a single candidate gene for mutant line *33UU*. Sequence analysis should identify the lesion in the mutant line and may place the previously uncharacterized *megalin* gene in the lumenogenesis pathway. Recent evidence suggests that Megalin is involved in chitin-based cuticle development and regulation of endocytosis, processes which have both been shown to be important for the creation of a lumen and the regulation of lumen size (Riedel, et al., 2011). These two processes may occur at different times during lumenogenesis. Ultrastructural analysis of this mutant line will provide clues as to whether Megalin is playing a role early in the lumenogenesis process through specific endocytic activity, or relatively late in the lumen development through its role in regulating chitin development.

Additionally, the sequencing and candidate gene analysis performed for mutant line *25C* also provides a single candidate gene and may also provide an allelic series that can be used to elucidate the molecular function of *CG32708*. Together, these three mutant lines now offer uncharacterized novel genes, or annotated genes whose function

has not been previously implicated in the development of tracheal terminal cells. Interestingly, many of these uncharacterized genes may have mechanistic functions that have not been previously implicated in lumenogenesis.

Table 2.1. Primer sequences and positions of identified SNPs used for mapping genes within the *ct* and *v* interval.

ID	Forward primer	Reverse primer	Position	Restriction Enzyme
XA35	AATGAGGGTGGAACAACAGC	ACGCCAAGTCCTTGCATTAC	8,602,357	HpyCH4IV
XA36	TCAGAAGCCACACGTTGAAG	GCGTTTGCCTTCCAGTTAAG	8,855,190	RsaI
XB22	GCTGCCATTAGTGGCTCTTC	AACTGGAGCAATGGAACCTG	8,953,086	NlaIV
XD11	TGCCTTCTTATTTGGACCAC	GCAGCTATTTTACAGCGACAAC	8,986,868	AluI
XD12	TTTGGCTCTTGGATGGAAAC	AACACGTATCCTGGGAGTGG	9,034,427	NspI
XB23	AGCTTGTGGGATGCATTTTC	TCTCACAAACCGAACAGCAG	9,056,658	SfaNI
XD13	CCGAAAGCTGCATAAAAAGC	CTTACATCCGCACGAAAGTG	9,069,631	Seq.
XA37	CTGGCAGCGAATTAAAAAGC	TTCCCAACGCCTACTACACC	9,102,640	DraI
XD1	TGGAGGTGAAACCCTCACTC	ACCGCGTTCAACTTTAATGG	9,186,760	HpyCH4III
XD2	GCCAATGTTGTTGCAGTGTC	GCAAACGCAAGGCTAGAATC	9,248,679	HpyCH4IV
XD9	ACGCTTAAATGAAGGGAAGC	CAATTTTTGTAGCCCACTGTTC	9,252,816	Seq.
XD10	CCATCCACCGACATATTGC	CGGAGTTCACTTGTGTGGAG	9,258,870	RsaI
XD5	TGGGTTCTCTGGTTCTTTCG	CGACAGAGTGATGTGGGATG	9,272,560	Seq.
XD6	CCCTTGCCCCCTTTACTAAC	TCATCTTTTGCGTTGCTTTG	9,313,455	MluI
XB25	CCTGTCATGTTTTCCGTGTG	TTACGCTGTGCCTCAAACAG	9,336,673	MfeI
XD7B	CTTCTTTCTGCGGCTCATTC	AAGCGAAAAATGGCAATGTC	9,371,304	Seq.
XD3A	AGATGGCAGGGTGAATAACG	AACATCTGCGTTGCCTTTTC	9,414,689	Seq.
XD8	AGAGCCTTGATTGTGGATGG	TGTGGCAGAGAGTCCTTGTG	9,436,596	Seq.
XD4	TCGATCCGTAGGTCAATTACTC	CTGGTTTGTCCATGTTAGATCG	9,447,815	XmnI
XB26	GGAGAAGCACGAGACTTTGG	CCTGCGCCTTATCACTAAGC	9,488,764	NcoI
XB32	TTGTCTGGCTGACTGGACTG	ATCTGGAACCAAAGCCAATG	10,389,240	HpyCH4III
XB33	TGTTCGCGCATAAATCAGAG	GTTGTTGGTGCTTTGTGGTG	10,537,641	BstXI

Based on *Drosophila* reference genome release 5.44. Restriction enzyme list indicates enzyme site polymorphism identified, Seq. indicates sequencing polymorphism.

Table 2.2. Transposable element insertions used for mapping genes within the *ct* and *v* interval.

Mutant	Transgene Insertion	FlyBase ID	Position	Recombinants	Direction
25C	*P{SuPor-P}-KG00121*	FBst0013043	8,961,856	N.D.	N.A.
	P{SuPor-P}-KG01702	FBst0013473	9,026,634	N.D.	N.A.
31ZZ	*P{XP}-d06942*	FBst1011231	6,875,836	1/8,400	Right
	PBac{WH}-f02398	FBst1017711	9,030,683	3/9,000	Right
	PBac{WH}--f06347	FBst1020516	9,081,578	9/51,200	Left
33UU	*PBac{RB}-e03903*	FBst1015338	9,228,462	6/N.D.	Right
	PBac{WH}-f05850	FBst1020151	9,230,574	5/N.D.	Right
	PBac{WH}-f04515	FBst1019207	9,359,639	4/N.D.	Left
	PBac{XP}-d01684	FBst1009351	9,391,423	4/N.D.	Left
	P{SuPor-P}-KG03908	FBst0013969	9,404,760	5/N.D.	Left

Based on *Drosophila* reference genome release 5.44. Direction indicates position of lethal mutation with respect to transgene insertion. N.D. =not determined

Table 2.3. List of candidate genes assayed by RNAi for lethality and tracheal defects.

Mutant	Candidate Gene	VDRC Number	Lethality*	Tracheal Defects †
5A	*Marf*	V40478	Yes	Variable
	Pat1	V27308	No	WT
	CG3973	V34772	No	WT
	C3G	V21306	No	WT
13A	*Lava lamp*	V40382	Yes	WT
	Vap-33-1	V30404	Yes	WT
	Fd3f	V37745	Yes	WT
	Cut up	V43115	No	WT
	Rala	V43622	Yes	Lumenless
17CC	*Vinculin*	V34585	No	WT
	CG3071	V29588	No	WT
	CG14054	V32088	No	Variable
	Egghead	V10137	No	WT
	Klp3A	V35974	No	WT
	Syntaxin4	V32413	No	WT
33UU	*Bcl7-like*	V20410	Yes	WT
	CG15316	V32560	No	WT
	CG12650	V22783	No	WT
	CG12654	V1109	Yes	WT
25C	*Bx42*	8264R-1	No	WT
	CG7039	V26007	No	WT
	CG7766	V52572	No	WT
	CG6999	V41828	No	WT
	CG7033	V41190	No	WT
	CG32708	V49325	No	Lumenless
	CG7246	V34256	No	WT

*Lethality tested with *Act5C-GAL4*
†Tracheal defects tested with *btl-GAL4*
WT= wild-type
Variable= low penetrance lumenless

Table 2.4. List of *25C* candidate genes sequenced and assayed by RNAi for tracheal defects.

Candidate Gene	Sequenced	Mutation	RNAi Phenotype
CG10970	Yes	No	N.D.
CG7267	Yes	No	N.D.
CG15366	Yes	No	N.D.
CG7246	Yes	No	N.D.
HP1b	Yes	No	N.D.
APC4	Yes	No	WT
CG32708	No	N/A	Lumenless
CG32706	No	N/A	N.D.
CG6999	No	N/A	WT
CG7033	Yes	No	WT
CG7766	Yes	No	WT
Bx42	Yes	No	WT
CG7039	Yes	No	WT
AP-1gamma	Yes	No	N.D.

N/A = indicates quality sequencing results could not be obtained

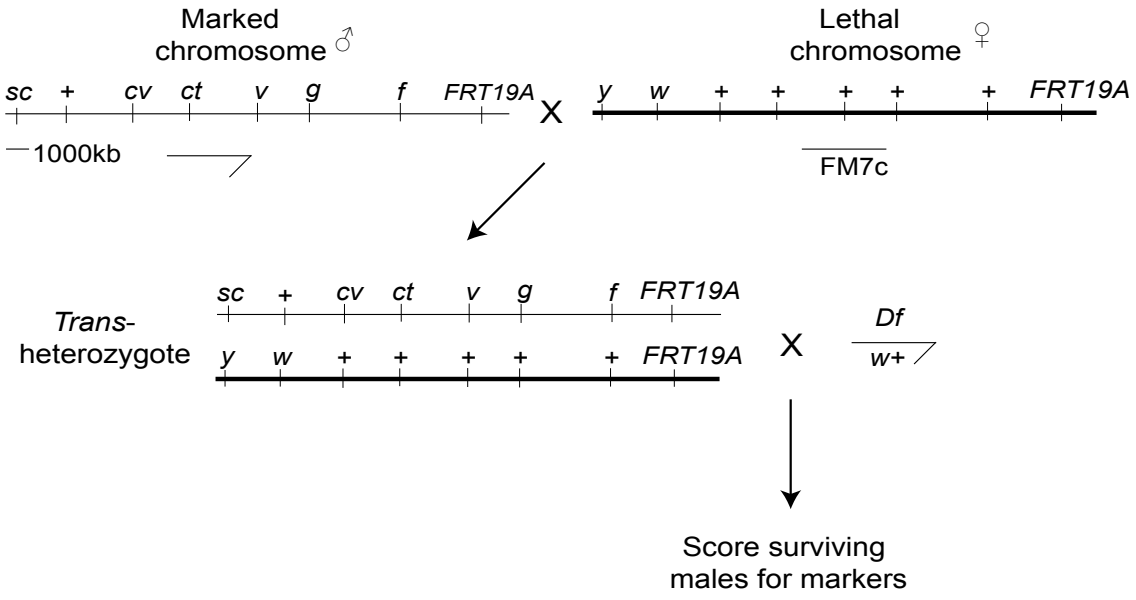

Figure 2.1: Genetic map of the *Drosophila* X chromosome and recombination mapping scheme. *Drosophila* X chromosome harboring multiple visible markers was used to create trans-heterozygote females containing a marked chromosome and a lethal chromosome (in bold). *Trans*-heterozygote females were then crossed to males containing a duplication of the w^+ gene, and viable progeny were scored for presence or absence of visible markers. The genes *sc* and *y* are not allelic, but are so close they essentially do not undergo recombination.

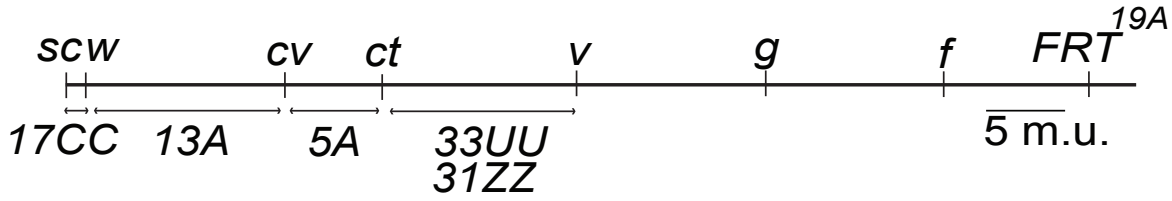

Figure 2.2: Genetic map of the *Drosophila* X chromosome. Mutants recovered from forward genetic screen of the X chromosome were mapped to discrete genetic intervals using a multipoint recombination mapping strategy. Genetic loci for five mutants comprising a subset from the lumenless class of mutants isolated were mapped to discrete intervals.

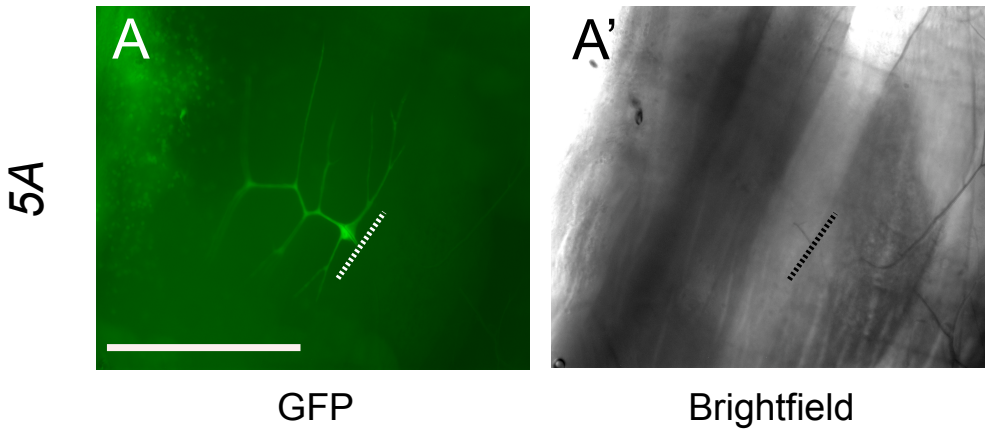

Figure 2.3. *5A* homozygous mutant terminal cells display a normal branching, but fail to make gas-filled lumen. Wild-type branching is assayed by cytoplasmic GFP (A) and brightfield optics are used to visualize gas-filling defect (A'). Bar, 200μm, dashed lines indicate proximal end of mutant cell.

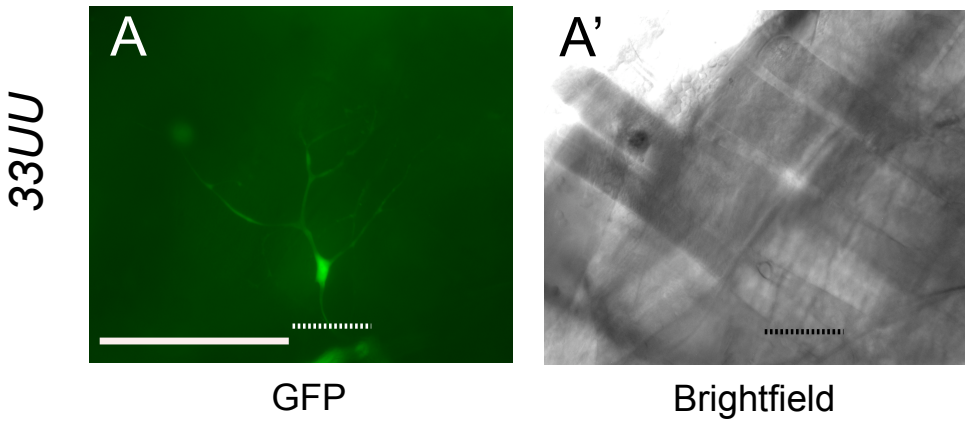

Figure 2.4. ***33UU*** **homozygous mutant terminal cells display a variable branching defects and are unable to generate functional gas-filled lumens.** Branching is assayed by GFP (A) and brightfield optics are used to visualize gas-filling defect (A'). Bar, 200μm, dashed lines indicate proximal end of mutant cell.

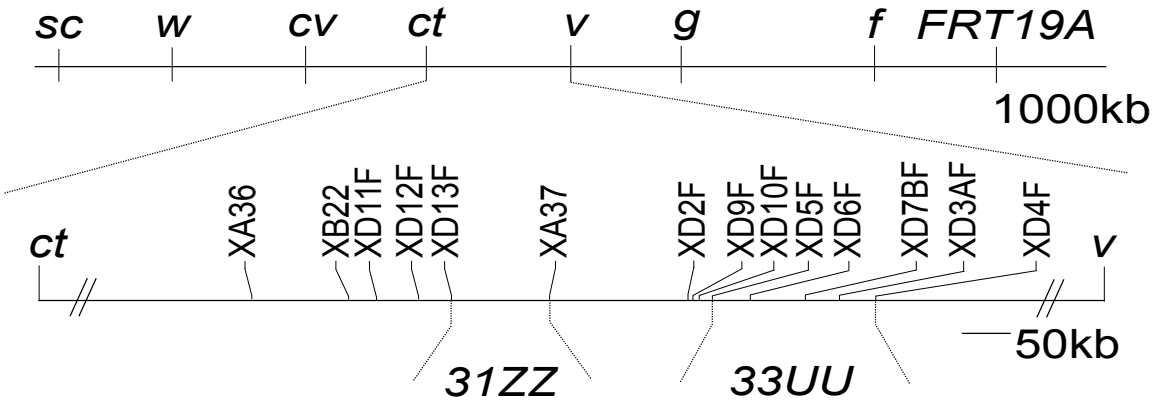

Figure 2.5: Identified SNPs within *ct* and *v* genetic interval. Single Nucleotide Polymorphism (SNP) mapping of lumenless mutant lines *31ZZ* and *33UU*.

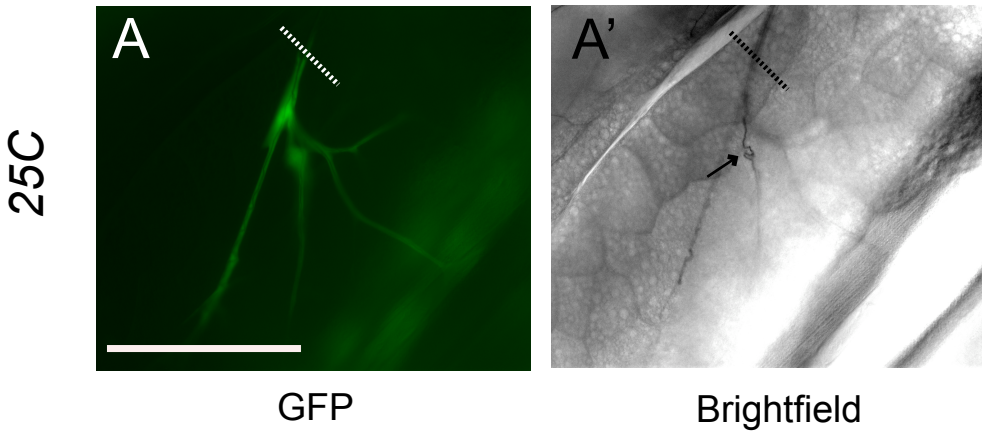

Figure 2.6. *25C* homozygous mutant terminal cells display a branch/lumen coordination defect. *25C* mutant cells display branching defects (A) and convoluted lumens (arrow) in some branches (A'). Bar, 200μm, dashed lines indicate proximal end of mutant cell.

References

Devine, W.P., et al., (2005). Requirement for chitin biosynthesis in epithelial tube morphogenesis. Proc. Natl. Acad. Sci. *102*, 17014-19

Guillemin, K., et al., (1996). The pruned gene encodes the Drosophila serum response factor and regulates cytoplasmic outgrowth during terminal branching of the tracheal system. Development *122*, 1353-62.

Ito, K., et al., (1997). The Drosophila mushroom body is a quadruple structure of clonal units each of which contains a virtually identical set of neurons and glial cells. Development *124*, 761-71.

Jarecki, J., et al., (1999). Oxygen regulation of airway branching in Drosophila is mediated by branchless FGF. Cell *99*, 211-20.

Jones, T. and M. Metzstein (2011). A novel function for the PAR complex in subcellular morphogenesis of tracheal terminal cells in Drosophila melanogaster. Genetics *189,* 153-64.

Lee, T., and L. Luo (1999). Mosaic analysis with a repressible cell marker for studies of gene function in neuronal morphogenesis. Neuron *22*, 45-61.

Riedel, F., D. Vorkel, and S. Eaton (2011). Megalin-dependent Yellow endocytosis restricts melanization in the Drosophila cuticle. Development *138*, 149-58

Schottenfeld-Roames J, Ghabrial AS. (2012). Whacked and Rab35 polarize dynein-motor-complex-dependent seamless tube growth. Nat Cell Biol. March 11

Shiga, Y., M. Tanaka-Matakats and S. Hayashi (1996). A nuclear GFP/β-galactosidase fusion protein as a marker for morphogenesis in living Drosophila. Dev. Growth Differ. *38*, 99-106.

Tonning A., et al., (2005). A transient luminal chitinous matrix is required to model epithelial tube diameter in the Drosophila trachea. Dev. Cell *9*, 423-30.

Xu, T., and G.M. Rubin (1993). Analysis of genetic mosaics in developing and adult Drosophila tissues. Development *117*, 1223-37.

CHAPTER 3

DROSOPHILA ZPR1 (ZINC FINGER PROTEIN 1) IS REQUIRED DOWNSTREAM OF BOTH EGFR AND FGFR SIGNALING FOR SUBCELLULAR LUMEN FORMATION

Introduction

Branched tubular networks, such as the vascular and respiratory systems, are a common structural design used to facilitate the transport of liquids and gases throughout the body. The cellular cues and signaling required for generating these complex networks, and tailoring each structure for a specific need (e.g., transporting liquid vs. transporting gases) are not well understood. To identify components involved in tubular network formation we are studying the *Drosophila melanogaster* tracheal (respiratory) system. The larval tracheal system in *Drosophila* is composed of a network of approximately 10,000 interconnected tubes which serve to transport oxygen and other gases throughout the body (Ghabrial et al., 2003). To construct this elaborate tubular network, cells within the tracheal epithelium first undergo a series of coordinated and stereotyped branching and tubulogenesis events during mid-embryogenesis. These events are primarily regulated by a Fibroblast Growth Factor ligand (FGF) and receptor (FGFR), encoded by the *branchless* (*bnl*) and *breathless* (*btl*) genes respectively (Sutherland et al., 1996, Lee et al., 1996). These Bnl and Btl mediated early outgrowth

events provide a cellular framework for what will eventually be the larval tracheal system, through which gases can enter the body and diffuse to target tissues. The mature larval tracheal system can be subdivided into three morphologically distinct tube types (Lubarsky and Krasnow, 2003). The first type are multicellular structures in which a polarized layer of epithelial cells is shaped to create a tube (Shim et al., 2001). Cross section of these branches reveals intercellular junctions that maintain a permeability barrier for the lumen, the hollow space through which gases are transported (Samakovlis et al., 1996A). The second type of tubes are unicellular and are made from single cells that wrap around their long axis and form an autocellular junction. The third type of tracheal tubes form in a specific cell type named terminal cells (Guillemin et al. 1996). Terminal cells are characterized by their extensive subcellular branching and their completely subcellular lumens, that form without cell junctions. In contrast to the stereotyped branching and lumen formation observed during early tracheal morphogenesis, terminal cell branch outgrowth is a dynamic process and is controlled by the extent of hypoxia in target tissues (Jarecki et al. 1996 and Ghabrial and Krasnow, 2006). Thus, terminal may provide a model for understanding the development of fine capillaries within the vertebrate vasculature whose development also depends on tissue oxygen status (Ghabrial et al., 2003). To identify factors required for branching and lumen formation specifically in terminal cells, we have analyzed a mutant obtained in a forward genetic mosaic screen of the X chromosome (Metzstein and Krasnow, unpublished results). We show here that this screen has identified a mutation in the gene *Zpr1* (*zinc-finger protein 1*). *Zpr1* is an evolutionarily conserved protein characterized by two C4 zinc fingers and two Zpr1-specific conserved homology domains and was first

identified in mammalian cells as a cytoplasmic protein that was capable of binding the intracellular domain of the unactivated EGF receptor (Galcheva et al., 1996). We find that Zinc Finger Protein 1 (Zpr1) is required for terminal cell lumen formation and also show that Zpr1 function lies downstream of both the FGF receptor (FGFR) and the epidermal growth factor receptor (EGFR).

Materials and Methods

Fly stocks and genetics

All flies were reared on standard media and raised at 25ºC. Control chromosomes used for clonal analysis were FRT^{19A} or FRT^{G13}. MARCM (Lee and Luo, 1999) analysis was done on the following alleles, $Zpr1^{31ZZ}$, $EGFR^{K05115}$ (Bloomington 10385), $EGFR^{f2}$ (Bloomington 2768), and $EGFR^{top\text{-}co}$(a gift from M. Fuller). The *btl-GAL4* driver was used for all tissue-specific experiments (Shiga et al., 1996). Positively marked homozygous mutant cells were generated using the stocks: *y w P{w+ btl-Gal80},* FRT^{19A}, $hsFLP^{122}$; *btl-Gal4, UAS-GFP* and *y w* $hsFLP^{122}$*; P{w+ tub-Gal80},* FRT^{G13}*; btl-Gal4, UAS-GFP* (a gift from S. Luschnig). The following EGFR RNAi and dominant negative transgenic lines were used in the gas-filling assays: y^1 v^1*; P{TRiP.JF01368}attP2*, (Bloomington 25781), y^1 v^1*; P{TRiP.JF01084}attP2*, (Bloomington 31526), y^1 v^1*; P{TRiP.JF02384}attP2*, (Bloomington 36773), and y^1 *w*; P{UAS-Egfr.DN.B}29-77-1; P{UAS-Egfr.DN.B}29-8-1*, (Bloomington 5364). For all receptor tyrosine kinase epistasis experiments a *y w P{w+ tub-Gal80},* FRT^{19A}, $hsFLP^{122}$; *btl-Gal4, UAS-DsRed* was used to generate MARCM clones that were homozygous mutant for *Zpr1*. The following over-expression transgenes were used for epistasis experiments: *w*;*

P{w[+mC]=Egfr.2.UAS}7-10, (Bloomington 9535), *w*; P{w[+mC]=Egfr.2.A887T.UAS}8-2* (Bloomington 9533) and *UAS*-λbtl (Lee et al., 1996). The presence or absence of these transgenes in the MARCM mutants was determined by scoring the presence of either of the following YFP-expressing balancer chromosomes: *w*; ry^{506} Dr^{1}/TM3, P{Dfd-GMR-nvYFP}3, Sb^{1}* (Bloomington 23231) *w*; sna^{Sco}/CyO, P{Dfd-GMR-nvYFP}* (Blomington 23230).

Identification of mutation in mutant line *31ZZ*

The lethality associated with mutant line *31ZZ* was mapped to ~72kb region (between TE insertion *PBac{WH}-f02398* and SNP XA37) using multiple meiotic recombination mapping strategies and has been described in more detail in Chapter 2. All genes lying within this genetic interval were examined for mutations by sequencing *trans*-heterozygous females carrying the *31ZZ* chromosome over a wild-type chromosome. A single non-synonymous mutation was identified in the gene *Zinc-finger protein 1* (*Zpr1*).

Transgenes and cloning

A 3.2 kb rescue transgene spanning the entire *Zpr1* genomic locus as well as 949 bp (base pairs) upstream of the gene was amplified by PCR (Primers in Table 3.1) and cloned into the *NotI* and *PmeI* restriction enzyme sites in the P[acman] transformation vector (Venken et al., 2006) and injected into flies carrying the VK00026 attB docking site on the 3rd chromosome for site-specific integration (Venken et al., 2006). We obtained a plasmid containing *Drosophila Zpr1* cDNA (LD37736, Gold Collection) from

the *Drosophila* Genomics Resource Center and PCR amplified the coding sequence for subsequent cloning (primers in Table 3.1). The coding sequence of *Zpr1* was then cloned into the pUAST+attP (a gift from Carl Thummel) transformation vector using the *NotI* and *EcoRV* restriction sites and injected into flies carrying the VK00027 attB docking site on the 3rd chromosome. All transgenic injections were done by Genetic Services Inc.

Terminal cell branching and lumen quantification

To determine the number of branches in both wild-type and mutant cells, we collected fluorescence images of GFP-labeled dorsal terminal cells. Branches from these cells were traced manually using the NeuronJ plug-in for ImageJ (Meijering et al., 2004). Branch order was assigned by the following scheme: the single central branch encompassing the nucleus was designated as the primary branch of each cell; secondary branches arise directly from that primary branch; branches that arise from secondary branches were categorized as tertiary branches, which in turn give rise to quaternary branches. To assay lumen formation in terminal cells, we used brightfield optics to visualize gas-filling. Since mutants were either completely gas-filled or completely empty and we did not see partial gas-filling we used a binary scoring system in which individual cells were scored as either wild-type gas-filling or lumenless. In experiments using tracheal specific RNAi or dominant negative transgenes we scored the lateral terminal cells in the Tr 3 and 4 tracheal hemisegments of individual animals.

Results

A mutant required for branching and lumen formation in *Drosophila* terminal tracheal cells

To identify genes involved in tracheal terminal cell development, a forward genetic mosaic screen of lethal mutations on the X chromosome was performed by using the MARCM system to generate positively (GFP) labeled homozygous mutant cells in heterozygous animals (Lee and Luo, 1999). Homozygous mutant cells were then scored for tracheal branching and air-filling defects by using a combination of fluorescence microscopy and brightfield optics to visualize terminal branching patterns and air-filling, respectively. Among the 900 lines that were scored, a mutant designated *31ZZ* was identified by its complete failure to generate air-filled lumens (Figure 3.1). *31ZZ* mutant cells also show a significant but variable branching defect (Figure 3.1). Wild-type terminal cells have a single central terminal branch from which secondary branches sprout, subsequent branching occurs from these secondary branches to generate tertiary branches and from these form quaternary branches. Wild-type cells also possess a single gas-filled lumen that runs through every branch class. We find that *31ZZ* mutants are able to generate a central branch and secondary branches, but fail to undergo tertiary and quaternary branching (Figure 3.1). Additionally, we find that *31ZZ* mutants fail to generate gas–filled lumen in all branch classes. While the branching phenotype was variable, gas-filling was completely abrogated in *31ZZ* mutant cells.

31ZZ* is an allele of *Drosophila Zpr1

To identify the causative mutation in *31ZZ* we mapped the lethality to a discrete genetic interval on the X chromosome using a multipoint recombination mapping strategy. This analysis allowed us to place the mutation in *31ZZ* to the 3.3Mb (megabase) interval between the *ct* and *v* genes. The interval containing *31ZZ* was then refined by using available transposable element insertions as molecular markers of meiotic recombination events. Lastly, to further refine our interval, single nucleotide polymorphisms (SNPs) were identified and scored in recombinants between *ct* and *v* allowing us to map the *31ZZ* mutation to a 72kb interval containing nine genes. Sequencing of the genes in this region identified a single point mutation (an A to T transversion) in the first exon of the gene *Zpr1*. The mutation results in a premature termination codon at amino acid position 58. To confirm this mutation as the causative allele in *31ZZ*, a 3.2 kb transgene spanning the *Zpr1* genomic locus as well as 949 base pairs upstream of the gene was transformed into flies and subsequently tested for rescue of the lethality and gas-filling defect associated with *31ZZ*. We found a single copy of this transgene was able to rescue the lethality associated with *31ZZ*, as well as the terminal cell lumenless defect (data not shown). Additionally, we generated transgenic flies carrying a UAS-Zpr1-cDNA or UAS-Zpr1-cDNA-N-terminal tagged GFP transgene and found both were able to rescue the lumenless phenotype in *31ZZ* mutant cells (data not shown).

EGFR loss-of-function phenocopies the Zpr1 lumenless defect

Zpr1 was first identified as a cytoplasmic protein that was capable of binding the intracellular domain of the unactivated EGF receptor (Galcheva et al., 1996). Additional work later showed a role for EGFR signaling in the development of the embryonic tracheal system, therefore we hypothesized that Zpr1 was mediating an EGFR signaling cascade required for subcellular lumenogenesis (Jeon and Zinn, 2009). This led us to test whether mutations in the EGFR would also have an effect on lumenogenesis. We tested the effect of EGFR mutations on terminal cell development by examining terminal cells mutant for loss-of-function EGFR alleles. Terminal cells mutant for any of these three null alleles of the EGFR ($EGFR^{K05115}$, $EGFR^{f2}$, and $EGFR^{top\text{-}co}$) resulted in some lumenless terminal cells. In contrast to the robust lumenless phenotype of *Zpr1* mutants, in which all mutant cells are lumenless, only a small percentage (around 15%) of terminal cells mutant for the EGFR display a lumenless phenotype (Figure 3.2D). To determine whether this was a characteristic of the particular EGFR alleles used, or a broader phenomenon of EGFR signaling, we conducted a series of experiments using different manipulations to remove EGFR function (Figure 3.2). We removed EGFR specifically in the tracheal system by using the tracheal specific *btl-GAL4* driver to express multiple available EGFR-RNAi lines, as well as an EGFR Dominant negative transgene. Surprisingly, all methods used to remove EGFR function displayed at most a similar penetrance to the loss-of-function mosaic experiments. These data suggest that other factors such as pathway redundancy through other RTKs or environmental factors such as hypoxic conditions may also function in regulating the lumen formation process.

We next tested if an increase in EGFR activity could induce lumen formation in tracheal terminal cells by over-expression of a wild-type version of the receptor as well as a constitutively active version. We find that over-expression of either the wild-type or activated versions of the EGFR result in an increase in lumen formation, characterized by multiple air-filled lumens within a single cell, a finding consistent with previously published data (Jeon and Zinn, 2009) indicating a role for EGF signaling in tracheal cell development (Figure 3.3, A and B). We decided to test whether *Zpr1* lies downstream of the EGFR by testing the epistatic relationship of *Zpr1* and the various EGFR over-expression transgenes. To test whether loss of *Zpr1* could suppress either of the EGFR mediated overgrowth phenotypes, we made *Zpr1* MARCM mosaics in which we employed the *btl-GAL4* that positively marks mutant cells to simultaneously drive the expression of either of the *UAS-EGFR* transgenes. We found that *Zpr1* mutant cells that over-express either the wild type or activated form of the EGFR are lumenless (Figure 3.3, D and E). This finding is consistent with Zpr1 functioning downstream of the EGFR, which was first proposed from cell culture experiments (Galcheva et al., 1996)and now provides the first *in vivo* evidence for this pathway.

Zpr1 lies downstream of multiple RTKs

The weak penetrance of our EGFR loss of function experiments led us to consider the possibility that other active RTKs could be feeding into the Zpr1 pathway. To test this, we tested the most well-studied active RTK in the *Drosophila* tracheal system, the FGFR Btl. Tracheal cells mutant for FGFR loss of function alleles fail to outgrow or undergo branching, hindering our ability to test these alleles in the larval terminal cells

(Glazer and Shilo, 1991). To bypass the early requirement of Btl, we tested the epistatic relationship of Zpr1 and FGFR by employing an activated form of the Btl receptor (*λbtl*). Overexpression of this activated form of the FGFR results in increased lumen formation which can be visualized by multiple air-filled lumens within single cells (Figure 3.3C). To test whether loss of Zpr1 could suppress this FGFR mediated overgrowth we made *Zpr1* MARCM mosaics in which the *btl-GAL4* which positively marks mutant cells also drives the expression of the *UAS-btlλ* transgene. We find that all *Zpr1* homozygous mutant cells display a *Zpr1* lumenless phenotype indicating that Zpr1 is epistatic to the luminal overgrowth phenotype observed in FGFR overexpression (Figure 3.3F).

Discussion

To achieve complete interconnectivity, a branched tubular network such as the *Drosophila* larval tracheal system must first undergo extensive branching and fusion steps that begin during embryogenesis and continue throughout larval development (Samakovlis et al., 1996B). Terminal cells must then undergo an additional intracellular lumen formation step to promote gas exchange. We show here that Zpr1 is required for this lumenogenesis process, and is also involved in regulating branch outgrowth of terminal cells. Zpr1 was initially identified as a protein that was able to bind the intracellular tail of the inactive EGFR, an interaction necessary for cell growth and division (Gangwani et al., 2005, Gangwani, 2006). Although the EGFR has previously been shown to be involved early in tracheal cell migration, and is necessary for maintaining the structural of the tracheal system, specific downstream effectors have not been identified in the tracheal system (Cela and Llimargas, 2006, Nishimura et al., 2007).

To our knowledge, this is the first *in vivo* evidence that demonstrates that Zpr1 functions downstream of the EGFR, and that Zpr1 activity is required for a specific developmental process. Additionally, our epistasis experiments show that Zpr1 lies downstream of multiple RTKs. Initial experiments aimed at mapping the EGFR-Zpr1 binding domains showed that Zpr1 binds to the subdomains X and XI of the EGFR (Galcheva-Gargova et al., 1996). This region is composed of three α helices and is well conserved in other RTKs such as the platelet-derived growth factor (PDGF) and the FGFR (Hubbard, et al., 1994). The binding of Zpr1 to this conserved motif on different RTKs was confirmed for the PDGF but not the FGFR (Galcheva-Gargova et al., 1996). Here we present the first genetic evidence that Zpr1 functions downstream of the FGFR in mediating lumen formation in terminal cells. Although the amount of conservation at subdomains X and XI of the FGFR suggest that the downstream function of Zpr1 is mediated through their direct physical interaction, we have yet to test this hypothesis through co-immunoprecipitation (Co-IP) experiments.

The finding that Zpr1 lies downstream of multiple RTKs allows us to propose a model that provides the cell with a method for interpreting various positional cues that help the cell determine whether it has reached hypoxic target tissue (Figure 3.4). In our model, hypoxic tissue secreting FGF serves as a long-range signaling molecule that instructs the outgrowth and active migration of terminal cells towards hypoxic tissue. Hypoxic tissue additionally secretes EGF as a short-range signaling molecule that induces lumen formation. Since lumen formation is an important step in mediating gas exchange between hypoxic tissue, the possible cross talk or redundancy between the FGFR and EGFR signaling cascades provide the cell with, a fail safe that can ensure

lumen formation occurs as well as an alternative method for modifying the amount of lumenogenesis that occurs during hypoxic conditions.

Table 3.1. List of primer sequences used for generating transgenic constructs.

Primer name	Sequence	Purpose
GAPIF	CGGGATGGGGCTATTAGTTC	Genomic Zpr1
GAPJ3R	TCATTTCCGCATGCATATTT	Genomic Zpr1
eGFP ForwardZPR1	AGGGCTACGAGGAGAAGGCGGTGAGCAAGGGCGAGGAGCT	UAS-Zpr1-GFP
eGFPRev	CTTGTACAGCTCGTCCATGCCGAG	UAS-Zpr1-GFP
Zpr1 RevGFP	GAACAGCTCCTCGCCCTTGCTCACCGCCTTCTCCTCGTAGCCCT	UAS-Zpr1-GFP
ZprcDNAF	GCGGCCGCAAACAGGAACTTTCGTGTGGA	UAS-Zpr1-GFP
ZprcDNAR	GATATCGGAAGAGTTTCCGACCATCC	UAS-Zpr1-GFP
ZPROUTF	ATGTCCACCGTGAGCGACCCCAACA	UAS-Zpr1
ZPROUTR	ATGAATTAATTGCTATATTTTTGCGAAT	UAS-Zpr1-GFP

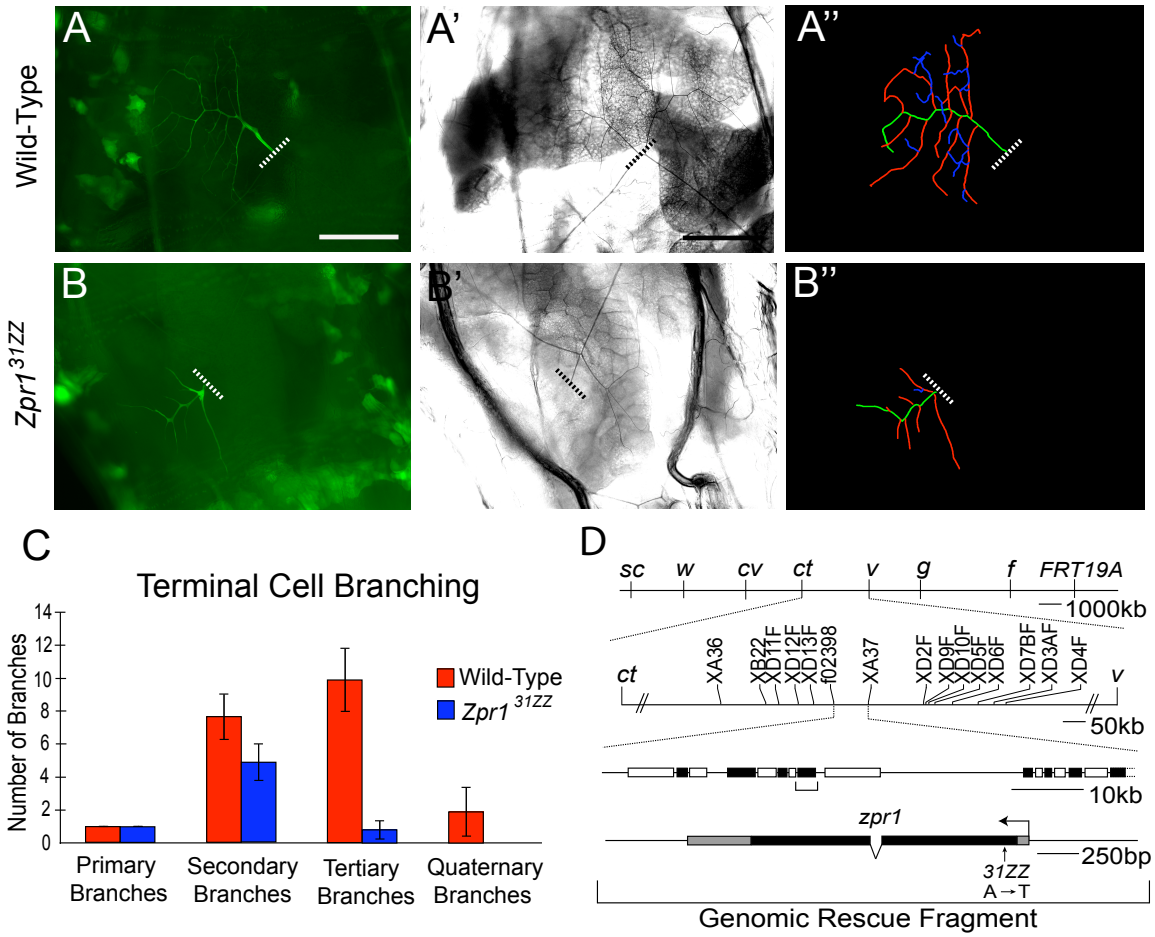

Figure 3.1: Zpr1 is required for branching and lumen formation in terminal cells. Mosaic L3 larvae were generated using the MARCM system. Homozygous mutant cells are positively marked by the expression of GFP. Tracheal cell branching and gas-filling patterns are characterized by using GFP (A, B) and brightfield microscopy (A', B'), respectively. (A'' and B'') Tracing of the branching patterns of cells in A and B. Wild-type terminal cells undergo extensive branching and have a single air-filled lumen in each branch (A-A''). *Zpr1* homozygous mutant cells exhibit branching defects and fail to generate a gas-filled lumen (B-B''). Dashed lines represent proximal end of cell. (C) Branching was quantified by designating branches of terminal cells as primary (green), secondary (red), tertiary (blue), or quaternary branch and totaling all branches. Tertiary and quaternary branching is affected in *Zpr1* mutants. Error bars are ±2 S.E.M of each class (n=9). (D) Mapping and identification of *31ZZ* mutant. Genetic map of the X chromosome and the *ct*-*v* interval. A combination of visible markers and single nucleotide polymorphisms were used to map the lethality associated with *31ZZ* to a 72 kb interval. Black and white boxes represent individual genes within the region. Subsequent sequencing of genes in the region identified a single A to T transversion at base pair position 172 of the *Zpr1* coding sequence. *Zpr1* coding region represented by black boxes, gray boxes represent 5' and 3' untranslated regions. Bar, 200μm.

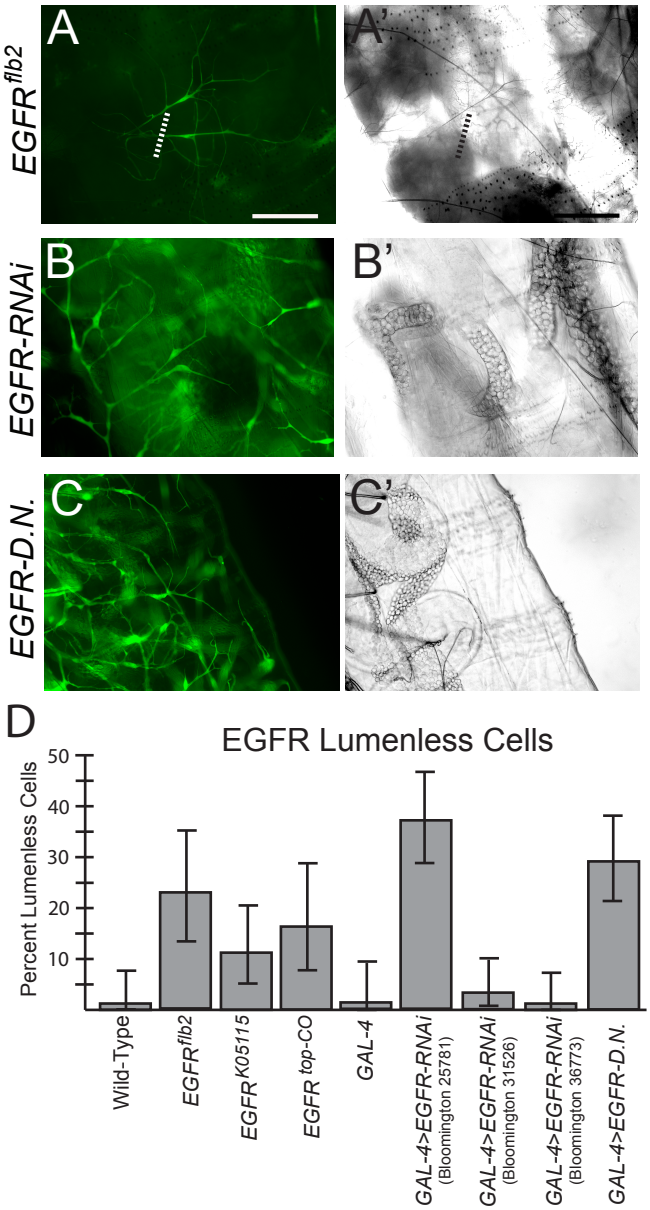

Figure 3.2: EGFR loss-of-function phenocopies *Zpr1* mutants. (A) Homozygous mutant cells are marked by the expression of GFP. (B) Tracheal specific expression of EGFR-RNAi (Bloomington 25781) (B) and dominant negative EGFR (C). Tracheal cell branching patterns and air-filled lumens are characterized by using GFP (A, B and C) and brightfield microscopy (A', B' and C'). *EGFR*^{flb2} loss-of-function homozygous mutants display a lumenless phenotype (A-A'). Depletion of EGFR by RNAi results in gas-filling defect (B-B'). Expression of a dominant negative form of the EGFR also results gas-filling defect (C-C'). (D) Quantification of pentrance of EGFR lumenless phenotype. For all conditions quantified a minimum of 55 cells were scored. For all RNAi and DN experiments terminal cells in the third and fourth metameres of single animals were scored. Error bars represent 95% confidence interval of the binomial distribution.

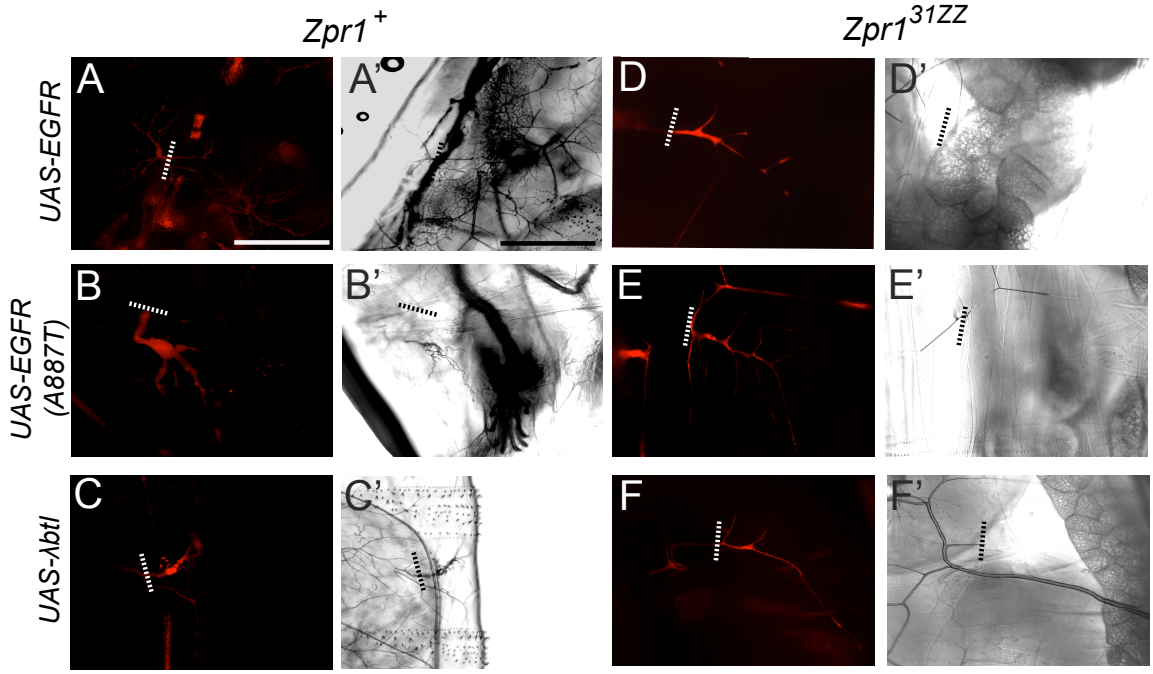

Figure 3.3: Zpr1 is epistatic to both EGFR and FGFR signaling in terminal cells. The tracheal specific *btl* promoter is used to positively label *Zpr1* homozygous mutant cells through the expression of a UAS-DsRed transgene and simultaneously drive the expression of other transgenes. Tracheal cell branching patterns and air-filled lumens are characterized by using DsRed (A-F) and brightfield microscopy (A'-F'). Over-expression the wild-type form of the EGF receptor in terminal cells is sufficient to drive luminal overgrowth (A-A'). Over-expression of an activated form of the EGF receptor in wild-type terminal cells results in extensive overgrowth of lumens and defects in branching (B-B'). Over-expression of an activated form of the FGF receptor in wild-type terminal cells results in extensive overgrowth of lumens and defects in branching (C-C'). *Zpr1* mutants are epistatic to the extensive luminal growth caused by wild-type EGFR overexpression (D-D') and activated EGFR (E-E'). *Zpr1* mutants are epistatic to the extensive luminal growth caused seen in *λblt* (FGFR*)* overexpression (F-F')
Dashed lines represent the proximal end of the DsRed labeled cells. Bar, 200μm.

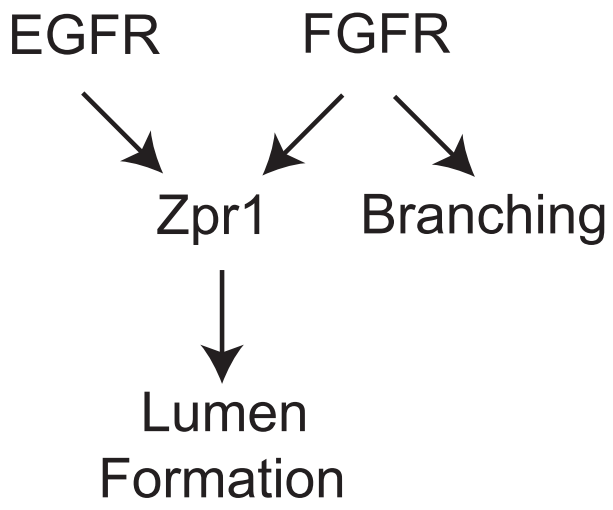

Figure 3.4: Model of Zpr1 function downstream of both EGFR and FGFR signaling in terminal cells. FGF signaling is required for early outgrowth and branching, and EGF signaling may used as a lumen formation cue during later stages in development.

References

Cela, C., M. Llimargas (2006). Egfr is essential for maintaining epithelial integrity during tracheal remodeling in Drosophila. Development *133*, 3115-3125.

Galcheva-Gargova, Z., et al., (1996). Binding of zinc finger protein ZPR1 to the epidermal growth factor receptor. Science *21*, 1797-802.

Gangwani, L. (2006). Deficiency of the zinc finger protein ZPR1 causes defects in transcription and cell cycle progression. Journal of Bio Chem *52*, 40330-40340.

Gangwani, L., R. Flavell and R.J. Davis (2005). ZPR1 is essential for survival and is required for localization of survival motor neurons (SMN) protein to Cajal bodies. Mol and Cell Bio *25.7*, 2744-2756.

Ghabrial, A. and M.A. Krasnow (2006). Social interactions among epithelial cells during tracheal branching morphogenesis. *Nature 441*,746-749.

Ghabrial, A., et al., (2003). Branching morphogenesis of the Drosophila tracheal system. Annu Rev Cell Dev Biol *19*, 623-47.

Glazer, L., B.Z. Shilo (1991). The Drosophila FGF-R homolog is expressed in the embryonic tracheal system and appears to be required for directed tracheal cell extension. Genes and Dev *5*, 697-705.

Guillemin, K., et al. (1996). The pruned gene encodes the Drosophila serum response factor and regulates cytoplasmic outgrowth during terminal branching of the tracheal system. Development *122*, 1353-62.

Hubbard, S.R., et al. (1994). Crystal structure of the tyrosine kinase domain of the human insulin receptor. Nature *372*, 746-54.

Jarecki, J., et al. (1999). Oxygen regulation of airway branching in Drosophila is mediated by branchless FGF. Cell *99*, 211-20.

Jeon, M and K. Zinn (2009). Receptor tyrosine phosphatases control tracheal tube geometries through negative regulation of EGFR signaling. Development *136*, 3121-3129.

Kamei, M., et al. (2006). Endothelial tubes assemble from intracellular vacuoles in vivo. Nature *442*, 453-56.

Lee, T., et al., (1996) Regulated Breathless receptor tyrosine kinase activity required to pattern cell migration and branching in the Drosophila tracheal system. Genes and Development *10*, 2912-2921

Lee, T., and L. Luo (1999). Mosaic analysis with a repressible cell marker for studies of gene function in neuronal morphogenesis. Neuron *22*, 45-61

Lubarsky, B. and M. A. Krasnow (2003). Tube morphogenesis: making and shaping biological tubes. Cell *112*, 19-28.

Mayuko, N., Y. Inoue and S. Hayashi (2007). A wave of Egfr signaling determines cell alignment and intercalation in the Drosophila tracheal placode. Development *134*, 4273-4282.

Meijering E., et al., (2004). Design and validation of a tool for neurite tracing and analysis in fluorescence microscopy images. Cytometry A *58*, 167-76

Samakovlis, C., et al. (1996). Development of the Drosophila tracheal system occurs by a series of morphologically distinct but genetically coupled branching events. Development *122*, 1395-407.

Samakovlis, C., et al. (1996). Genetic control of epithelial tube fusion during Drosophila tracheal development. Development *122*, 3531-6.

Shiga, Y., M. Tanaka-Matakats and S. Hayashi (1996). A nuclear GFP/β-galactosidase fusion protein as a marker for morphogenesis in living Drosophila. Dev. Growth Differ. *38*, 99-106.

Shim, K., K. Blake, J. Jack, and M.A. Krasnow. (2001) The Drosophila ribbon gene encodes a nuclear BTB domain protein that promotes epithelial migration and morphogenesis. Development *128*, 4923-4933.

Sutherland, D., C. Samakovlis, et al. (1996). branchless encodes a Drosophila FGF homolog that controls tracheal cell migration and the pattern of branching. Cell *87*, 1091-101.

.

Venken K.J., Y. He, R.A. Hoskins and H.J. Bellen (2006). P[acman]: a BAC transgenic platform for targeted insertion of large DNA fragments in D. melanogaster. Science *15*, 1747-51.

CHAPTER 4

ANALYSIS OF ZPR1-INTERACTING PROTEINS

Introduction

In a forward genetic screen of the X chromosome for mutations disrupting different aspects of branching and lumen formation in *Drosophila* tracheal terminal cells, mutations in the gene *Zpr1* (*zinc-finger protein 1*) were identified by their primary effect on lumenogenesis. Zpr1 is an evolutionarily conserved protein characterized by two C4 zinc fingers and two conserved homology domains. In mammals, Zpr1 was first identified as a cytoplasmic protein that was capable of binding the intracellular domain of the unactivated EGF receptor (Galcheva-Gargova et al., 1996). Upon EGFR activation the EGFR-Zpr1 complex dissociates and Zpr1 can interact with the eukaryotic translation elongation factor 1A (eEf1α) (Gangwani et al., 1998) or bind multiprotein complexes formed by the survival motor neurons 1 (SMN1) protein (Gangwani et al., 2005). The significance of these interactions remains unclear but are thought in part to help localize Zpr1 to the nucleus.

The effect of active EGF signaling on the subcellular localization of Zpr1 suggests that there may be factors that can negatively regulate this interaction. Recent evidence has shown that the receptor tyrosine phosphatases, Ptp4E and Ptp10D (the only two phosphatases known to be expressed in tracheal system) play a role in regulating

tracheal lumen formation during *Drosophila* embryogenesis (Jeon and Zinn, 2009). Additional experiments have shown that these RPTPs may exert this control through the negative regulation of the EGFR (Jeon and Zinn, 2009). Here we show that terminal cells homozygous mutant for both *Ptp4E* and *Ptp10D* display extensive cytoplasmic outgrowth and blebbing, but fail to generate a gas-filled lumen or display luminal overgrowth in our gas-filling assay. We also show that RNAi knockdown of the two known Zpr1 binding partners eEf1α and SMN1 also result in lumenless terminal cells.

Materials and methods

Recombination of PTP mutants onto *FRT*^{19A} chromosome

Trans-heterozygous females containing a chromosome bearing mutations in *Ptp4E* and *Ptp10D* (the double mutant will be referred to as *Ptp4E10D*) over a multiply marked X chromosome (*FRT*^{19A}) were crossed and progeny reared on G418 selection media. This allowed us to select recombination events in which the *FRT*^{19A} chromosome had been included (Figure 4.1). Single viable females with the visible markers indicating that a recombination event had occurred within our interval of interest were used to establish individual balanced lines. These lines were then tested for lethality and subsequently used in MARCM (Lee and Luo, 1999) to test the function of *Ptp4E10D* in tracheal terminal cells.

RNAi knockdown of known Zpr1 interacting proteins

The tracheal specific promoter *breathless* (Shiga et al., 1996) was used to drive UAS-RNAi transgenes directed against individual Zpr1-binding partners. Expression of

GFP was used to assay terminal cell branching and brightfield microscopy for gas-filling defects. Lethality was assayed by using the Actin-promoter to ubiquitously drive the expression of GAL4 mediated-RNAi knockdown. Individual fly lines used for RNAi experiments are listed in Table 4.1.

Molecular cloning and generation of UAS-Zpr1-RNAi transgenic flies

To generate a Zpr1-RNAi targeting construct we used the primer pairs Zpr1RNAi A and Zpr1RNAi B (Table 4.2) to generate 448bp amplicons of the Zpr1 coding sequence (Table 4.2). We then inserted each of these these amplicons in a reverse tandem orientation into a pUAST+I (a gift from Amin Ghabrial) by using the *NotI*/*KpnI*/*KpnI*/*XbaI* cloning sites in the vector. The construct was then injected into *Drosophila* embryos to generate transgenic flies. All injections were performed by Genetic Services Inc.

Molecular cloning and generation of UAS-Zpr1 site-directed mutants

To generate UAS-Zpr1 constructs harboring previously characterized point mutations, we used a standard PCR-based zippering cloning technique in which point mutations are introduced via custom oligonucleotide primers. Primer pairs ZR303FN, ZR303R, ZR407FN and ZR407R (Table 4.2) were used for the PCR amplification of individual products with overhangs. Primers ZprOUTF and ZprOUTR were then used for the final zippering reaction (Table 4.2). Targeting vectors were injected in embryos harboring the VK0027 site for specific integration (Venkken et al., 2006).

Ultrastructural analysis of mutant terminal cells

The tracheal specific promoter *breathless* was used to drive either a UAS-RNAi transgene directed against Zpr1 or various EGFR and FGFR over-expression transgenes (Table 4.3). For our experiment we used larvae at stage L1 and L2 because of their small size. Larvae were picked at late L1 and early L2 larval stages and kept in PBS buffer before freezing. Animals were then prepared by using a method developed by L. Nikolova in our lab. Briefly, larvae were loaded into the specimen carriers filled with the bacteria *E. coli*, which was used as cryo-protectant. Carriers were then high pressure-frozen using a BAL-TEC HPM 010 freezer (BAL-TEC, Inc., Carlsbad, CA). Larvae were then submitted to a freeze substitution in a pre-cooled to -90°C mix of 1-2% osmium tetroxide (OsO_4) and 0.1% Uranyl Acetate in 97% acetone using Leica EM AFS (Leica Microsystems, Vienna, Austria. Specimens were freeze substituted for 72 hrs at -90°C, then gradually warmed up at the rate of 5°C/hrs to -20°C and incubated at this temperature for another 8-16 hrs. Specimens were then rinsed with pure acetone. Specimen infiltration was performed by incubating the specimens in a gradually increasing concentrations of Epon Araldite epoxy resin (EMS cat. 13940) and then prepared for polymerization at 60°C for 48 hrs. 45-70nm sections were obtained using a diamond knife and collected on coated copper grids. The sections were imaged at 125keV using a Hitachi 7200 electron microscope.

Molecular cloning and generation of fluorescent tagged Zpr1 transgenic flies

To generate fluorescent tagged Zpr1 constructs we used multiple approaches. First, we made two genomic rescue constructs in which we fused the coding sequence of either eGFP or mCherry (Promega) to the N-terminus end of Zpr1. To achieve this, we inserted a KpnI restriction enzyme site before the translational start of Zpr1 using primers Zpr1NtermF, Zpr1NtermR, GAPIF and GAPJ3R (Table 4.2). We then inserted the coding sequence of either eGFP or mCherry into this KpnI site with standard cloning techniques. We inserted this genomic construct into the p[ACMAN] transformation vector (Venkken, et al., 2006) for injection and site-specific integration into the VK00027 genomic locus. Additionally, we generated a UAS-Zpr1 construct in which the coding sequence of eGFP was inserted at the C-terminus of Zpr1. To do this, we first amplified the coding regions of both Zpr1 and GFP with primers eGFP ForwardZPR1, Zpr1RevGFP, Zpr1cDNAF and Zpr1cDNAR (Table 4.2). These PCR products were designed to have overhangs that could then be used to zipper the two products together in a subsequent round of PCR. We then cloned the zippered product into a pUAST+attB targeting construct (a gift from Carl Thummel) by using the *NotI* and *StuI* sites in the plasmid. This targeting construct was then injected for site-specific integration into both the VK00027 and ATTP16 genomic loci. All injections were performed by Genetic Services Inc.

Results

Clonal analysis of PTP double mutants

Mutants homozygous null for the two receptor tyrosine phosphatases expressed in the tracheal system are embryonic lethal (Jeon and Zinn, 2009). To bypass the lethality and assay the effect of these homozygous mutations specifically in tracheal terminal cells we recombined the *Ptp4E10D* mutations onto our FRT^{19A} chromosome and performed clonal analysis using the MARCM system (Figure 4.1). Twenty individual lines were established from the general recombination scheme outlined in Figure 4.1 and tested for lethality. Of these 20 lines, 6 lines tested were viable indicating that we had lost one of the RPTP mutations and were and discarded. These numbers are consistent with the relative positions of the genetic markers used. Of the remaining 14 lethal lines (which contained both RPTP mutations), 7 were used for clonal analysis and all but one displayed a cystic blebbing phenotype or uncontrolled cytoplasmic growth (Figure 4.2). Contrary to our model in which loss of RPTP function would result in an unregulated luminal growth, all homozygous mutant cells scored were unable to generate gas-filled lumens. Interestingly, all of the lumenless cells also displayed varying degrees of cytoplasmic blebbing and outgrowth. One interpretation of this result would be that these RPTPs are simply involved in cytoplasmic growth and not in a lumenogenesis pathway. Another interpretation may be that RPTPs are involved in the regulation of both a cytoplasmic outgrowth program and a lumenogenesis program, but the continued cytoplasmic growth may remove important cues that are necessary for specifying where a cell will make a lumen thus impeding general lumenogenesis.

Generation of a Zpr1 RNAi transgenic line

The tracheal specific promoter *breathless* was used to drive a UAS-RNAi transgene directed against *Zpr1* (V12665). This transgenic line was obtained from the Vienna *Drosophila* RNAi Center (VDRC) and used to assay for terminal cell defects and lethality. Lethality was assayed by using the Actin-promoter to ubiquitously drive the expression of GAL4 mediated-RNAi knockdown. We failed to induce either lethality or see a lumenless phenotype in our RNAi experiment. Since we knew that a null *31ZZ* mutant displayed both lethality and mutant terminal cells that failed to fill with gas, we concluded that this RNAi targeting construct was ineffective. We thus generated a new *Zpr1-RNAi* construct (See Materials and Methods) and found that expression in terminal cells led to ~60% of cells displaying a lumenless phenotype (Figure 4.3). Although this result indicates that the targeting construct is better able to functionally knock-down *Zpr1* in terminal cells when compared to the VDRC line, the low efficiency may prohibit its use in tissue-specific experiments.

RNAi knockdown of known Zpr1 interacting proteins

To better understand the molecular pathway through which Zpr1 mediates lumen formation in tracheal terminal cells, we tested the requirement of the known Zpr1 interacting proteins by RNAi. Previous evidence has shown that mammalian Zpr1 can interact with the eukaryotic translation elongation factor 1A (eEf1α) and form multiprotein complexes with the survival motor neurons 1 (SMN1) protein (Gangwani et al., 1998; Gangwani et al., 2005). Additionally, it has been shown that both of these binding events result in the nuclear redistribution of Zpr1-containing complexes, and the

disruption of these interactions affects cell growth (Gangwani, 2006). Although these interactions clearly play a role in mediating growth, the molecular mechanism through which they exert this control remains uncharacterized.

Drosophila contains a single homologue (*smn*) of the human *SMN1* gene which was identified by its sequence homology to the human gene. In humans, *SMN1* has undergone a duplication event which has resulted in two copies of the *SMN1* gene (*SMN1* and *SMN2*). Mutations in the *SMN1* locus are viable because of the partial redundancy conferred by *SMN2*. In contrast to the human *SMN1* mutant phenotype, mutations in *Drosophila smn* cause embryonic lethality. To test the requirement of *smn* in tracheal terminal cells, we obtained transgenic flies carrying different RNAi constructs directed at *smn*. To assay for RNAi function we first crossed each line to the ubiquitous *Actin-GAL4* driver and found that only one of the three lines displayed a lethal phenotype. We then used the *btl-GAL4* driver to express these RNAi transgenes specifically in the tracheal system. We found of the three lines tested, tracheal cells in one line (K16725R-2) phenocopied *Zpr1* null mutants and displayed a lumenless phenotype (Figure 4.3). The line that displayed a lumenless phenotype is also the only line that caused lethality when driven by the *Actin-GAL4* promoter. This data indicates that that the lack of a lumenless phenotype may arise from inefficient knockdown in the two remaining lines.

The binding interaction between Zpr1 and eEf1α was first indentified and characterized in mammalian cell lines and the yeast *Saccharomyces cerevisiae*. These studies showed that Zpr1 and eEf1α bind one another and redistribute to the nucleus in response to nutrient stimulation (Gangwani et al., 1998). This interaction has been shown to be important for growth in both yeast and mammalian cell lines, since disruption of

this interaction results in cell cycle arrest and defective cell growth (Gangwani, 2006). Previous studies have shown that eEf1α is involved in diverse cellular processes, but a specific role or molecular mechanism for its interaction with Zpr1 has not been identified (Munshi et al., 2001; Newberry et al., 2007). *Drosophila* contains two eEf1α homologues (eEf1α100E and eEf1α48D). To assay the specific requirement of eEf1α in tracheal terminal cells, we used the tracheal specific promoter *btl* to drive RNAi constructs targeting these genes. We obtained a total of five transgenic lines targeting both eEf1α100E or eEf1α48D (the similarity between both of these genes makes targeting each gene individually difficult). All five transgenic lines caused a lumenless defect in tracheal terminal cells. These data indicate that disruption of either of the previously identified Zpr1 binding partners results in lumenless terminal cells.

The observation that Zpr1 re-localizes from the cytoplasm to the nucleus during active signaling has led to the idea that Zpr1 must play an important role in the nucleus. Recently it was discovered that in yeast, the peptidyl-prolyl isomerase Cyclophilin A (CprA) promotes the export of Zpr1 from the nucleus (Ansari et al., 2002). In *Drosophila* there is a single Cyclophilin A homologue named *cyp1*. We hypothesized that if Zpr1's primary role in promoting lumenogenesis was in the nucleus, then if we could inhibit the action of its nuclear exporter *cyp1*, we could sequester Zpr1 in the nucleus and see an overgrown lumen phenotype. To perform this experiment we obtained two transgenic lines with RNAi constructs targeting *cyp1*. We used both the ubiquitous *Actin-GAL4* promoter and the tracheal specific *btl-Gal4* promoter to individually drive the expression of both of these RNAi transgenes and but did not observe either a lethal phenotype or abnormal tracheal development (data not shown).

One simple interpretation of these experiments could be that the extent of *cyp1* knockdown was insufficient to sequester Zpr1 in the nucleus resulting in a wild-type phenotype. Another possibility is that in *Drosophila*, Zpr1 nucelar export may be mediated by a different protein, or multiple redundant proteins. One final interpretation of these experiments could be that the role of Zpr1 in lumen formation is mainly cytoplasmic and the inhibition of its nuclear export may not have an effect on lumenogenesis.

Molecular cloning and generation of UAS-Zpr1 site directed mutants

The initial identification of CprA as the protein responsible for Zpr1 nuclear export in yeast also identified point mutations in the yeast Zpr1 that disrupted this CprA/Zpr1 interaction (Ansari et al., 2002). Independent point mutations resulting in a glycine to aspartic acid change (amino acid position 337) and aspartic acid to asparagine (amino acid position 444) were identified in a screen aimed at identifying mutations that could induce synthetic lethality when placed in a CypA null mutant background (Ansari et al., 2002)). Both mutations resulted in the constitutive nuclear localization of mutant Zpr1 proteins. To investigate the significance of these point mutants in *Drosophila* tracheal terminal cell development we generated the corresponding point mutations in *Drosophila UAS-Zpr1* constructs (amino acid residues 303 and 407 respectively). We first tested whether expression of either of these *Zpr1* point-mutant constructs displayed dominant phenotypes by using the *btl-Gal4* to drive their expression. We find that neither of these transgenes have dominant effects when overexpressed in tracheal terminal cells. We next tested whether either of these transgenes were able to rescue the

loss of *Zpr1*. To do this we made *Zpr1* MARCM mosaics in which the *btl-GAL4* which positively marks mutant cells also drives the expression of the mutant *UAS-Zpr1* transgene. We find that expression of either of these mutant transgenes is not sufficient to rescue the lumenless phenotype of a *Zpr1* homozygous mutant terminal cell (data not shown). Note, we have shown that expression of a wild-type Zpr1 in terminal cells is sufficient to rescue *Zpr1* null mutant.

Ultrastructural analysis of mutant terminal cells

We have previously shown that overexpression of the wild-type version of the EGFR results in an increase in lumen formation. In addition, overexpression of an activated form of the receptor exacerbates this extensive luminal overgrowth defect. However, the extent of luminal growth in both of these phenotypes is difficult to characterize with brightfield optics. To characterize the extensive luminal growth observed upon overexpression of either wild-type or activated forms of the receptor, we prepared larvae expressing these constructs for ultrastructural analysis by electron microscopy. Wild-type tracheal terminal cells have a single lumen which can be readily identified by its dark staining taenidial folds, a modification of the chitinous exoskeleton found in insect trachea (Figure 4.4). However, we found that overexpression of the wild-type EGFR results in terminal cells that have at least one additional air-filled luminal structure observed in each cross-section. Similarly, we find that overexpression of activated EGFR results in the creation of multiple luminal structures. To assay what a functionally lumenless terminal cell looks like by ultrastructural analysis, we prepared animals expressing our *UAS-Zpr1-RNAi* transgene. We find that in the case of Zpr1

knockdown, terminal cells are able to create what structurally appears to be a wild-type lumen with the exception that these lumens have dark staining material where wild-type cells have empty space (Figure 4.4) . This data may indicate that the role of Zpr1 occurs late in the lumenogenesis pathway. Another interpretation of this data is that the ultrastructural phenotype we see in *Zpr1-RNAi* cells is representative of a hypomorphic allele of Zpr1 and that the null mutant would appear more severe.

Molecular cloning and generation of fluorescent tagged Zpr1 transgenic flies

To investigate the subcellular localization and tissue specific requirements of Zpr1, we generated a series of fluorescent tagged Zpr1 constructs. First, we made a genomic rescue construct in which we fused the coding sequence of either eGFP or mCherry to the N-terminus of Zpr1. Both of these constructs were able to fully rescue the lethality associated with Zpr1 mutants(data not shown) as well as the lumenless defect in homozygous mutant terminal cells (Figure 4.5). We then used fluorescence microscopy to visualize tissues expressing these genomic tagged versions of Zpr1. Unfortunately, we were unable to detect the fluorescence from either construct. Previous expression data for *Zpr1* indicates that maternally deposited in the embryo and is widely expressed throughout embryogenesis (FlyAtlas). The lack of fluorescence from both of these constructs may indicate a very low level of expression of *Zpr1* throughout larva. To assay the subcellular localization of Zpr1 in tracheal terminal cells we constructed a *UAS-Zpr1* transgene with a C-terminus eGFP tag. To test whether loss of Zpr1 could be rescued by this *UAS-Zpr1-GFP* transgene we made *Zpr1* MARCM mosaics in which the

btl-GAL4 that positively marks mutant cells also drives the expression of the *UAS-Zpr1-GFP* transgene. We find that expression of this transgene is sufficient to rescue the lumenless defect in *Zpr1* homozygous mutant terminal cells (Figure 4.6). We then employed this *UAS-Zpr1-GFP* transgene to visualize the subcellular localization of Zpr1 in the presence of wild-type Zpr1. For all cells scored, GFP expression seemed to be enriched in the nucleus when compared to a DsRed transgene expressed in the same cell (Figure 4.7). This *UAS-Zpr1-GFP* transgene can be used in future experiments to determine the tissue specific requirement of Zpr1.

Discussion

Zpr1 is an evolutionarily conserved protein that was initially identified by its ability to bind the intracellular tail of the unactivated EGFR. Subsequent analysis showed that, in response to EGFR stimulation, Zpr1 accumulates in the nucleus. The lack of a nuclear localization sequence on Zpr1 led to the finding that both the eukaryotic translation elongation factor 1A (eEf1α) and the survival motor neurons 1 (SMN1) protein could bind Zpr1, and form multiprotein complexes that localize to the nucleus of proliferating cells. A previously conducted forward genetic screen for mutations affecting *Drosophila* terminal cell development identified mutations in *Zpr1* by their primary effect on lumen formation. We show here that the disruption of the two previously identified binding partners of Zpr1 also results in lumenless terminal cells. Additionally we show that the null mutations in the two RPTPs expressed in tracheal system result in excessive cytoplasmic outgrowth and lumenless cells. This result on its own may be interpreted as an indication that these RPTPs are not very specific and may

be affecting other RTKs. But, when these data are taken together with our genetic data showing that multiple RTKs may be feeding into the Zpr1 pathway, a more complex signaling cascade arises. Indeed, the idea that FGFR may be playing a role in the Zpr1 cascade has been tested indirectly by using mutations affecting *smn*. Specifically, Sen et al., showed that tissue specific activation of the FGF pathway ameliorates *smn* defects in *Drosophila* muscle. Although the downstream targets of this rescue were not investigated, it supports the hypothesis that over-activation of Zpr1 may be sufficient to bypass mutations in *smn*. We have now generated some of the tools that will allow us to investigate the downstream effects of Zpr1 and begin to address its specific role in the nucleus.

Table 4.1. RNAi knock-down of Zpr1 interacting proteins

Gene	CG Number	Stock Number	Lethality	Tracheal Defect
SMN1	CG16725	K16725R-2*	Yes	Lumenless
	CG16725	K16725R-3*	No	WT
	CG16725	BL45447	No	WT
eEF1A100E	CG1873	V40157†	Yes	Lumenless
	CG1873	V40156†	Yes	Lumenless
	CG1873	K1873R-4(3)*	Yes	Lumenless
eEF1A48D	CG8280	V24271†	Yes	Lumenless
	CG8280	V49890†	No	Lumenless
Zpr1	CG9060	V12665†	No	No
	CG9060	R284	Yes	Lumenless
Cyp1	CG9916	BL33001	No	WT
	CG9916	BL33950	No	WT

**Drosophila* Genetic Resource Center
†Vienna *Drosophila* RNAi Center
BL- Bloomington Stock center
R-Metzstein Lab

Table 4.2. List of primer sequences used for generating transgenic constructs.

Primer name	Sequence	Purpose
Zpr1RNAiA Forward A	GCGGCCGCGGAGCAGACCGACGAGATAG	Zpr1-RNAi
Zpr1RNAiA Reverse A	CTCGAGCTCCTTTAGGCGGTGCAATC	Zpr1-RNAi
Zpr1RNAiA Forward B	TCTAGAGGAGCAGACCGACGAGATAG	Zpr1-RNAi
Zpr1RNAiA Reverse B	GGTACCCTCCTTTAGGCGGTGCAATC	Zpr1-RNAi
GAPIF	CGGGATGGGGCTATTAGTTC	Zpr1-mCh/GFP
GAPJ3R	TCATTTCCGCATGCATATTT	Zpr1-mCh/GFP
Zpr1NtermF	GTGTGGATAGCAATCAAATCGGTACCATGTCCACCGTGAGCGACCC	Zpr1-mCh/GFP
Zpr1NtermR	GGGTCGCTCACGGTGGACATGGTACCGATTTGATTGCTATCCACAC	Zpr1-mCh/GFP
mCherryF	AGGTACCATGGTGAGCAAGGGCGAGGAGGATAAC	mCherry
mCherryR	GGTACCCTTGTACAGCTCGTCCATGCCGCCG	mCherry
eGFP ForwardZPR1	AGGGCTACGAGGAGAAGGCGGTGAGCAAGGGCGAGGAGCT	U-Zpr1-GFP
eGFPRev	CTTGTACAGCTCGTCCATGCCGAG	U-Zpr1-GFP
Zpr1 RevGFP	GAACAGCTCCTCGCCCTTGCTCACCGCCTTCTCCTCGTAGCCCT	U-Zpr1-GFP
ZprcDNAF	GCGGCCGCAAACAGGAACTTTCGTGTGGA	U-Zpr1-GFP
ZprcDNAR	GATATCGGAAGAGTTTCCGACCATCC	U-Zpr1-GFP
ZR303FN	GACGAACGAAGTGAAGTCCGACGGCGGAGTGGAGGCGCAGGGT	QCR303
ZR303R	GTCGGACTTCACTTCGTTCGTCTT	QCR303
ZR407FN	ATTACGCTGGTGCTGGAGACCCCGGCCGGTAATACCTATGTGCAA	QCR407
ZR407R	GGTCTCCAGCACCAGCGTAATGACTCG	QCR407
ZPROUTF	ATGTCCACCGTGAGCGACCCCAACA	QC
ZPROUTR	ATGAATTAATTGCTATATTTTTGCGAAT	QC

Table 4.3. Transgenic fly lines used for ultrastructural analysis.

Gene	CG Number	Stock Number	Allele Type	Tracheal Phenotype
EGFR	CG10079	BL9535	Over-expression	Extra Lumens
EGFR	CG10079	BL9533	Activated	Extra Lumens
Zpr1	CG9060	R284	RNAi	Lumenless

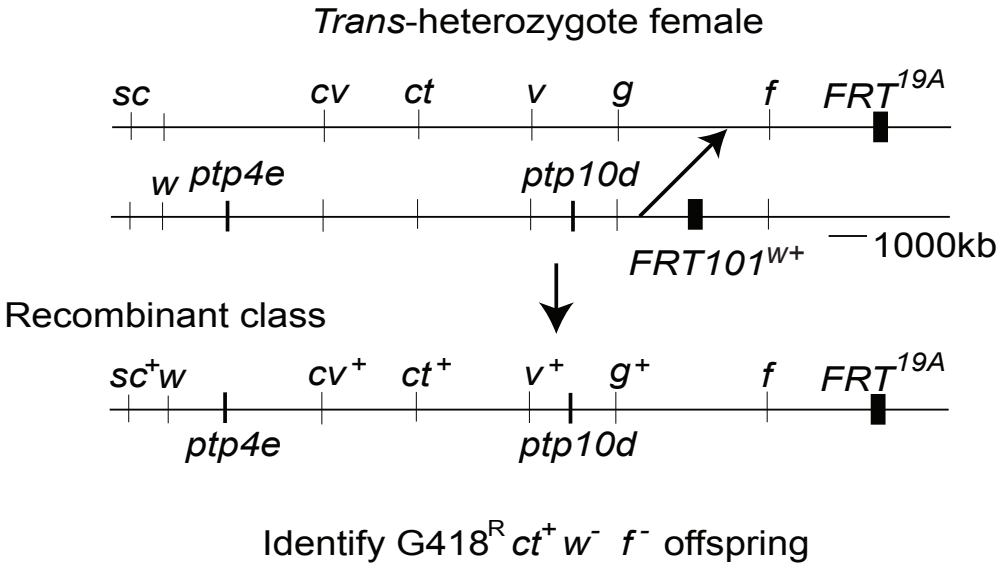

Figure 4.1. Scheme for recombination of PTP mutations onto *FRT*^{19A} chromosome.

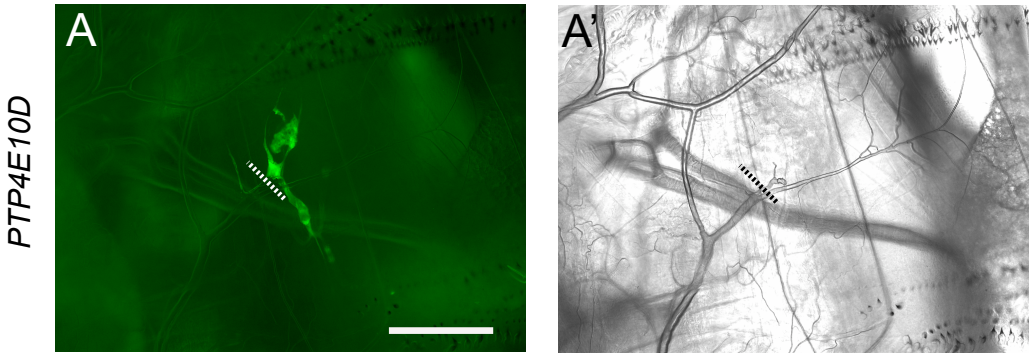

Figure 4.2. Homozygous PTP mutant terminal cells display cytoplasmic blebbing and fail to fill with gas.
Moscaic L3 larvae were generated using the MARCM system. Homozygous mutant cells are positively marked by the expression of GFP through the tracheal specific *btl* promoter. Tracheal cell branching and gas-filling patterns are characterized by using GFP (A) and brightfield microscopy (A'), respectively. Dashed lines represent the proximal end of the GFP labeled cell. Bar: 200μm.

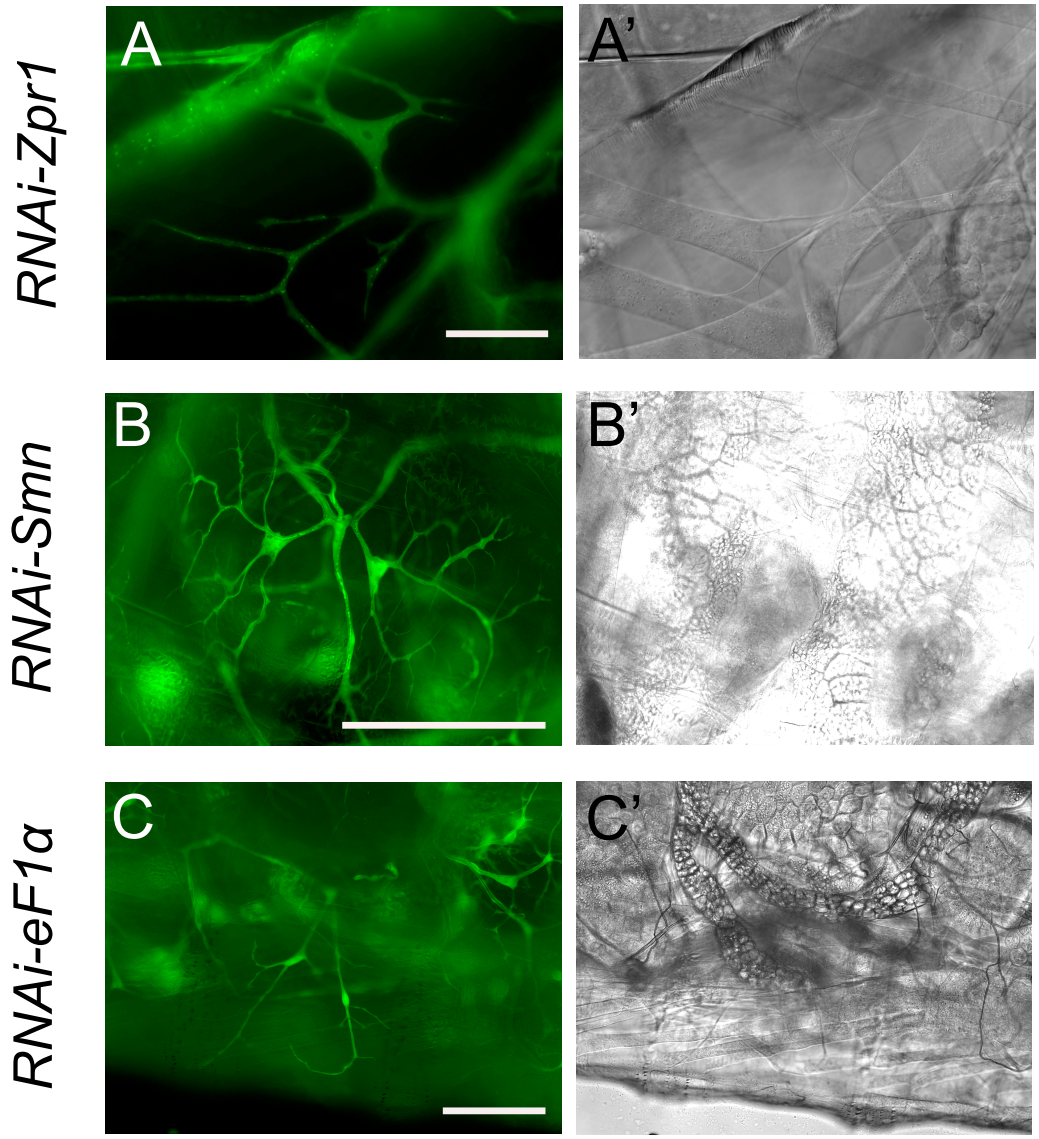

Figure 4.3. RNAi knockdown of *Zpr1* and known binding proteins.
The tracheal specific *btl* promoter is was used to express dsRNA against *Zpr1* and known interacting proteins. Tracheal cell branching and gas-filling patterns are characterized by using GFP (A, B and C) and brightfield microscopy (A', B', and C'), respectively. Bars: 50μm (A) and 200μm (B and C).

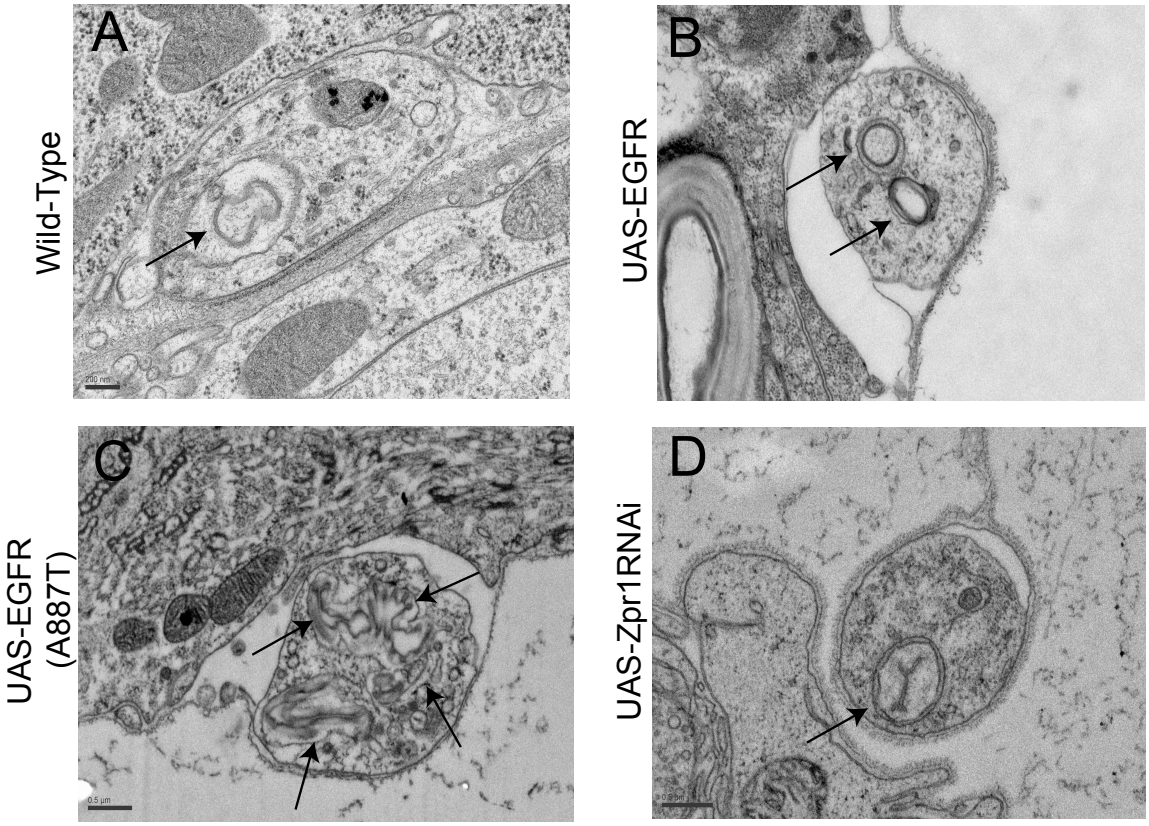

Figure 4.4. Ultrastructural analysis of EGFR overexpression and knockdown of Zpr1.

To characterize the structures of luminal overgrowth and lumenless phenotypes, larvae expressing different UAS transgenes with the tracheal specific *btl* promoter were prepared for analysis by electron microscopy. Tracheal terminal cell lumens are visualized by EM (A, B, C, and D). Arrows indicate lumen structures. Bars: 200nm (A) and 500nm (C and D).

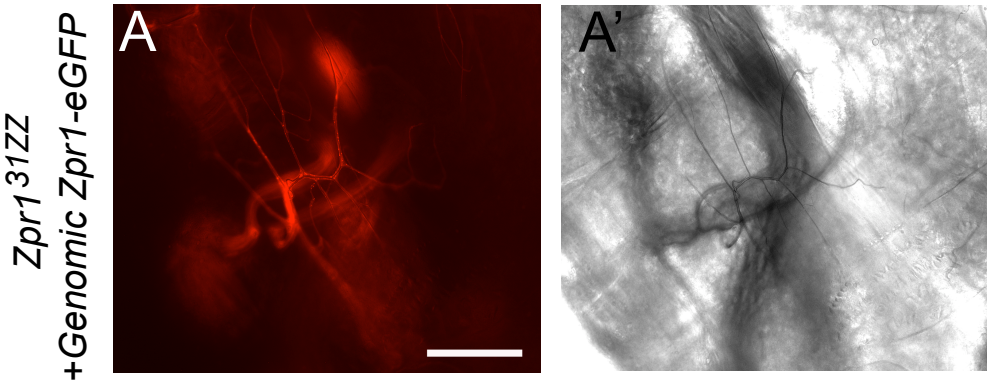

Figure 4.5. Genomic N-terminus GFP tagged Zpr1 rescue of *Zpr1*^{31ZZ} mutant cells. Moscaic L3 larvae were generated using the MARCM system. A single copy of the genomic N-terminus GFP tagged Zpr1 is in the background of the heterozygous animal. Tracheal cell branching and gas-filling patterns are characterized by using DsRed (A) and brightfield microscopy (A'), respectively. Bar: 200μm.

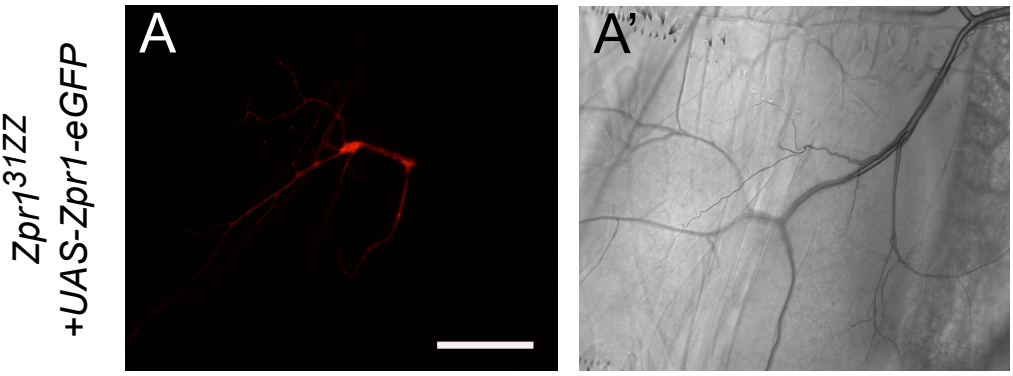

Figure 4.6. UAS-C-terminus GFP tagged Zpr1 rescue of *Zpr1*^{31ZZ} mutant cells. Moscaic L3 larvae were generated using the MARCM system. The tracheal specific *btl* promoter is used to positively label *Zpr1* homozygous mutant cells through the expression of a UAS-DsRed and simultaneously drive the expression of a C-terminus tagged Zpr1-GFP transgene. Tracheal cell branching patterns and air-filled lumens are characterized using DsRed (A) and brightfield microscopy (A'), respectively. Bar: 200μm.

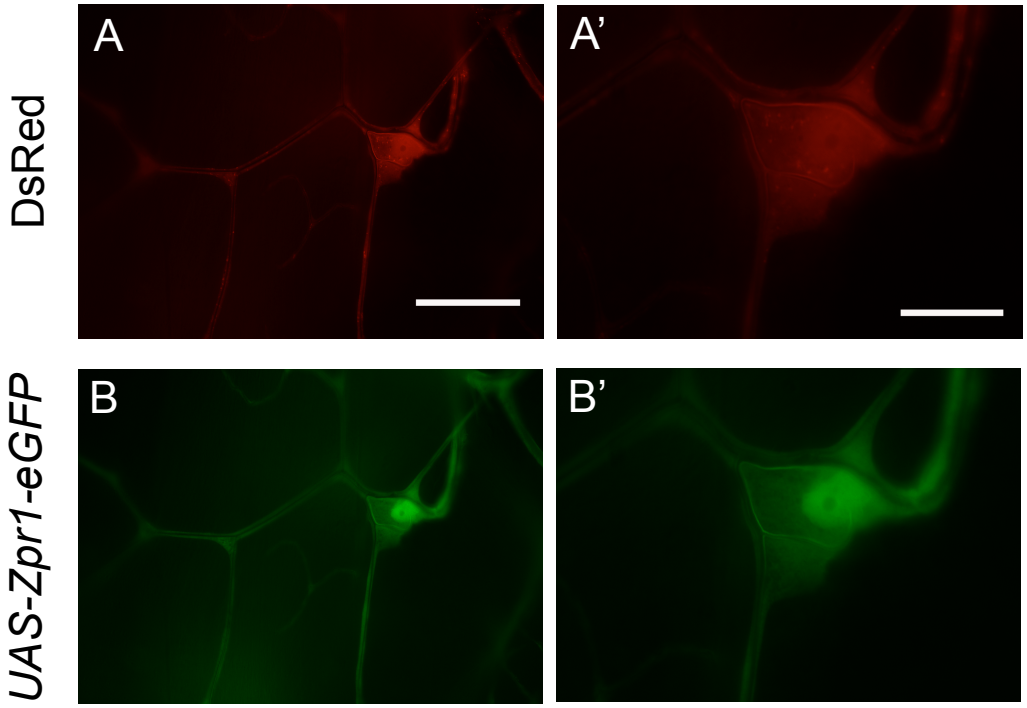

Figure 4.7. UAS-C-terminus GFP tagged Zpr1 localization in wild-type terminal cells.
The tracheal specific *btl* promoter is used to dirve the expression of DsRed and a UAS-C-terminus GFP tagged Zpr1 transgene. The subcellular localization of a DsRed transgene (A and A') can be used to compare to the localization of GFP tagged-Zpr1 construct (B and B'). Bars: 50μm (A and B) and 20μm (A' and B').

References

Ansari, H., G. Greco and J. Luban (2002). Cyclophilin A peptidyl-prolyl isomerase activity promotes Zpr1 nuclear export. Molecular and Cell Bio *22*, 6993-7003.

Galcheva-Gargova, Z., L. Gangwani, K.N., R.J. Davis et al. (1998). The cytoplasmic zinc finger protein ZPR1 accumulates in the nucleolus of proliferating cells. Molecular Biology of the Cell *9*, 2963-2971.

Galcheva-Gargova, Z., et al. (1996). Binding of zinc finger protein ZPR1 to the epidermal growth factor receptor. Science *21*, 1797-802.

Gangwani, L. (2006). Deficiency of the zinc finger protein ZPR1 causes defects in transcription and cell cycle progression. Journal of Bio Chem *52*, 40330-40340.

Gangwani, L., et al. (1998). Interaction of ZPR1 with translation elongation factor-1alpha in proliferating cells. Journal of Cell Bio *143*, 1471-1484.

Gangwani, L., R. Flavell and R.J. Davis (2005). ZPR1 is essential for survival and is required for localization of survival motor neurons (SMN) protein to Cajal bodies. Mol and Cell Bio *25.7*, 2744-2756.

Jeon, M., and K. Zinn (2009). Receptor tyrosine phosphatases control tracheal tube geometries through negative regulation of EGFR signaling. Development *136*, 3121-3129.

Lee, T., and L. Luo (1999). Mosaic analysis with a repressible cell marker for studies of gene function in neuronal morphogenesis. Neuron *22*, 45-61.

Munishi R., et al. (2001). Overexpression of the translation elongation factor factor 1A affects the organization and function of the actin cytoskeleton in yeast. Genetics *157*, 1425-1436.

Newberry, H.J., et al. (2007). Translation elongation eF1A2 is essential for post-weaning survival in mice. Jour. Biological Chem *282*, 28951-28959.

Shiga, Y., M. Tanaka-Matakats and S. Hayashi (1996). A nuclear GFP/β-galactosidase fusion protein as a marker for morphogenesis in living Drosophila. Dev. Growth Differ. *38*, 99-106.

Shiia, N., et al. (1994). Microtuble servering by elongation factor 1alpha. Science. *266*, 282-285.

Sen, A., et al. (2011) Modeling spinal muscular atrophy in Drosophila links smn to FGF signaling. JCB *192*, 481-495.

Venken K.J., et al. (2006). P[acman]: a BAC transgenic platform for targeted insertion of large DNA fragments in D. melanogaster. Science *15*, 1747-51.

CHAPTER 5

MUTATIONS IN 2 DISTINCT GENETIC PATHWAYS RESULT IN CEREBRAL CAVERNOUS MALFORMATIONS IN MICE

Reprint of: Chan AC, Drakos SG, Ruiz OE, Smith AC, Gibson CC, Ling J, Passi SF, Stratman AN, Sacharidou A, Revelo MP, Grossmann AH, Diakos NA, Davis GE, Metzstein MM, Whitehead KJ, Li DY (2011). Mutations in 2 distinct genetic pathways result in cerebral cavernous malformations in mice. J. Clin. Invest. 121:1871–1881.

Reprinted with permission

Research article

Mutations in 2 distinct genetic pathways result in cerebral cavernous malformations in mice

Aubrey C. Chan,[1,2] Stavros G. Drakos,[1,3] Oscar E. Ruiz,[4] Alexandra C.H. Smith,[1,4] Christopher C. Gibson,[1,5] Jing Ling,[1] Samuel F. Passi,[1] Amber N. Stratman,[6] Anastasia Sacharidou,[6] M. Patricia Revelo,[7] Allie H. Grossmann,[1,7] Nikolaos A. Diakos,[1] George E. Davis,[6] Mark M. Metzstein,[4] Kevin J. Whitehead,[1,3] and Dean Y. Li[1,2,3,4]

[1]Molecular Medicine Program, [2]Department of Oncological Sciences, [3]Division of Cardiology, Department of Medicine, [4]Department of Human Genetics, and [5]Department of Bioengineering, University of Utah, Salt Lake City, Utah, USA. [6]Department of Medical Pharmacology and Physiology, School of Medicine, University of Missouri School of Medicine, Columbia, Missouri, USA. [7]Division of Anatomic Pathology, Department of Pathology, University of Utah, Salt Lake City, Utah, USA.

Cerebral cavernous malformations (CCMs) are a common type of vascular malformation in the brain that are a major cause of hemorrhagic stroke. This condition has been independently linked to 3 separate genes: Krev1 interaction trapped (*KRIT1*), Cerebral cavernous malformation 2 (*CCM2*), and Programmed cell death 10 (*PDCD10*). Despite the commonality in disease pathology caused by mutations in these 3 genes, we found that the loss of *Pdcd10* results in significantly different developmental, cell biological, and signaling phenotypes from those seen in the absence of *Ccm2* and *Krit1*. PDCD10 bound to germinal center kinase III (GCKIII) family members, a subset of serine-threonine kinases, and facilitated lumen formation by endothelial cells both in vivo and in vitro. These findings suggest that CCM may be a common tissue manifestation of distinct mechanistic pathways. Nevertheless, loss of heterozygosity (LOH) for either *Pdcd10* or *Ccm2* resulted in CCMs in mice. The murine phenotype induced by loss of either protein reproduced all of the key clinical features observed in human patients with CCM, as determined by direct comparison with genotype-specific human surgical specimens. These results suggest that CCM may be more effectively treated by directing therapies based on the underlying genetic mutation rather than treating the condition as a single clinical entity.

Introduction

Cerebral cavernous malformations (CCMs) are common vascular malformations with a prevalence of 1 in 200 to 250 individuals in unselected populations (1, 2). CCMs can lead to focal neurological deficits, seizures, and hemorrhagic stroke, but no pharmacologic therapy currently exists (3). CCMs predominantly occur in the central nervous system and are characterized by subclinical bleeding and consequential hemosiderin deposits that are detected by MRI (4). MRI is the primary clinical modality for detection, diagnosis, and management of CCMs. Hemosiderin deposits give CCMs an MRI appearance of a central mass with a dark perilesional halo, whose appearance is nearly diagnostic (pathognomonic) of cavernous malformation (5). Cavernous malformations are characterized by a complex of vascular channels of varying sizes lined by a single layer of endothelial cells without any abnormally large arteries, arterialized veins, or large venous outflow vessels. Although dense fibrillary neuroglial tissue may penetrate the mass, vascular channels are generally arranged in a back-to-back pattern with little or no intervening brain parenchyma. There is often a peripheral margin of gliotic tissue containing hemosiderin-laden macrophages (6).

CCMs can occur sporadically or be inherited in an autosomal dominant pattern. Familial CCM has been linked to heterozygosity for any of 3 genes: Krev1 interaction trapped (*KRIT1*), Cerebral cavernous malformation 2 (*CCM2*), and Programmed cell death 10 (*PDCD10*) (7). All 3 proteins bind each other in coimmunoprecipitation experiments on cells overexpressing these proteins, leading to the hypothesis that they function as a complex to affect a common signaling mechanism (8). Both Krit1 and Ccm2 are required for proper connection of the developing heart with the aorta to establish circulation in the mouse embryo (9, 10). Mice lacking either Krit1 or Ccm2 fail to form a lumenized first branchial arch artery to link the heart and aorta; as a result, mice lacking either gene die at the same age. The requirement for Ccm2 is endothelial autonomous (9, 11). In the endothelium, both KRIT1 and CCM2 suppress the activity of the small GTPase RhoA (9, 12). Loss of either gene leads to RhoA activation and signaling through Rho kinase (ROCK) resulting in increased actin stress fibers, impaired cell-cell interactions, and increased vascular permeability (9, 12, 13). These defects can be reversed in cell culture and in mice with inhibitors of RhoA including HMG-CoA reductase inhibitors (statins) (9, 12).

A recent report suggested a similar mechanism of Rho activation for PDCD10 (14). However, other studies have suggested a different cell-signaling role for PDCD10. While KRIT1, CCM2, and PDCD10 all occupy the cytoplasmic compartment of the cell, unique subcellular localization for each has been described, including nuclear localization of KRIT1 (15) and Golgi localization of PDCD10 (16). Each protein has also been found to have unique binding partners (17–19). PDCD10's binding partners include members of the germinal center kinase III (GCKIII) subfamily of serine-threonine kinases with homology to yeast sterile-20 (STE20) kinase (16, 20–23). Furthermore, the clinical features of CCM in *KRIT1*, *CCM2*, and *PDCD10* families have important differences (24, 25), with *PDCD10* resulting in the most severe disease (24, 26). It is possible that CCM disease is the common result of multiple unique mechanisms and may require unique therapeutic strategies to target the underlying disturbed cellular and signaling pathways.

Conflict of interest: The University of Utah seeks to commercialize this technology and has filed patent applications related to this manuscript.

Citation for this article: *J Clin Invest.* 2011;121(5):1871–1881. doi:10.1172/JCI44393.

Table 1
Early growth arrest and death in embryos lacking *Pdcd10*

Cross	*Pdcd10*$^{+/-}$ × *Pdcd10*$^{+/-}$			
Genotype	*Pdcd10*$^{+/+}$	*Pdcd10*$^{+/-}$	*Pdcd10*$^{-/-}$	Total litters
No. of progeny				
E7.5	75	114	52	27
E8.0	9	13	0[A]	4
E8.5	27	45	0[A]	13
E9.0	1	5	0	1
>E9.0	7	8	0	3

The numbers of normal-appearing and viable offspring by genotype in matings between *Pdcd10*$^{+/-}$ parents are shown. [A]Ages at which growth-arrested embryos could be obtained.

Though the signaling and cellular mechanisms associated with the 3 known CCM proteins may be different, a common genetic mechanism of loss of heterozygosity (LOH) has been suggested for familial CCM disease (27–29). Familial CCM is more aggressive than sporadic disease, with an earlier age of onset, increased risk of hemorrhage and seizure, and an increased number of lesions (3, 30–32). These observations have led to the hypothesis that CCM disease occurs by the Knudson 2-hit mechanism, similar to retinoblastoma (33). There is limited evidence from human pathologic specimens to support an association of LOH with CCM lesions. In a series of challenging experiments, a number of investigators have identified biallelic mutations, 1 somatic and 1 germline, in the endothelium of a subset of patient samples (27, 28, 34). While LOH could not be confirmed for a number of samples, a total of 4 cases have been described for *KRIT1* and 1 case each for *CCM2* and *PDCD10*. Mice heterozygous for *Krit1* or *Ccm2* do not develop cavernous malformations, and no examples of secondary somatic mutations have been reported (35, 36).

To determine whether endothelial LOH is not simply associated with, but is causative for, CCM pathology, requires an animal model with a controlled genetic mutation that can be directed and detected in a tissue-specific manner. In this work, we use drug-inducible, tissue-specific strains of Cre recombinase to target conditional null alleles of the CCM genes to test directly the 2-hit hypothesis for cavernous malformations. We demonstrate that *Pdcd10* differs substantially from *Ccm2* in development, cell biology, and signaling, yet LOH is the common genetic mechanism to cause CCMs in both genotypes. These findings suggest that PDCD10 influences different endothelial signaling pathways from KRIT1/CCM2 to lead to a common histopathology and imply that medical treatment to stabilize familial CCM may need to be developed and evaluated in a genotype-specific manner.

Results

Loss of Pdcd10 results in embryonic lethal phenotypes distinct from loss of Krit1 or Ccm2. To determine the role of *Pdcd10* in development and disease, we developed a conditional null allele, *Pdcd10*^{flox}, in which exons 4–8 are flanked with LoxP sites (Supplemental Figure 1; supplemental material available online with this article; doi:10.1172/JCI44393DS1). This strategy also allowed us to generate a constitutive null allele, *Pdcd10*$^{-}$, by crossing mice carrying *Pdcd10*^{flox} with a mouse strain expressing Cre recombinase in the germline (37). To characterize the role of *Pdcd10* in development, we intercrossed *Pdcd10*$^{+/-}$ mice and harvested embryos at varying stages of development. Surprisingly, we found that mice lacking *Pdcd10* died at a much earlier age than those deficient for either *Krit1* or *Ccm2*. Whereas *Krit1* and *Ccm2* mice show growth arrest at E9.0 and die at E11 (9–11), the loss of *Pdcd10* leads to growth arrest at E8.0, after gastrulation, but prior to the onset of circulation or the requirement for cardiovascular function (Table 1 and Supplemental Figure 1).

An earlier requirement for *Pdcd10* than *Krit1* or *Ccm2* in development does not preclude a shared role in the vascular system. Mice with endothelial loss of *Ccm2* phenocopy the constitutive null mutant (9, 11), so we sought to determine whether mice with endothelial loss of *Pdcd10* would also recapitulate the *Ccm2* phenotype. Using the endothelial Tie2-Cre driver, the same Cre driver that we used to ablate *Ccm2* (9), we found that although mice with endothelial loss of *Pdcd10* (*Pdcd10*$^{flox/-}$*;Tie2-Cre*) did not survive to birth, they had patent branchial arch arteries, a developed circulatory system, and were indistinguishable from control littermates at E9.5 (Supplemental Figure 2). Instead, we found that loss of *Pdcd10* in the endothelium leads to progressive enlargement of the cardinal vein and other veins of the rostral embryo at E11.5 (Figure 1). Venous enlargement was not due to abnormal cardiac structure or function (Figure 1 and Supplemental Figure 2), nor were defects observed in arteries of the embryo (Figure 1 and Supplemental Figure 2). Death occurred due to hemorrhage from venous rupture by E13.5 (Table 2). Additionally, mice with loss of *Pdcd10* in neural and glial tissues induced by Nestin-Cre showed no vascular or any other obvious defects and were born alive (Supplemental Figure 2 and Supplemental Table 1). These observations suggest that *Pdcd10* is required in the endothelium for control of venous size and integrity, yet *Pdcd10* differs from *Ccm2* in that it is not required for the establishment of circulation.

Loss of PDCD10 does not affect RhoA signaling but results in lumen formation defects. To explore the role of PDCD10 in endothelial cells, we depleted *PDCD10* in human dermal microvascular endothelial cells (HMVEC) with siRNA (Supplemental Figure 3). Whereas the loss of CCM2 leads to an increase in actin stress fibers as a result of RhoA activation (9, 12, 13) and phosphorylation of myosin light chain-2 by Rho kinase (Figure 2), we observed none of these indicators of RhoA activation with the loss of PDCD10 (Figure 2). Thus, the role of PDCD10 in endothelial cell biology and signaling differs from that of CCM2.

Having found that PDCD10's function in development differs from that of CCM2, we sought to identify defects associated with PDCD10 depletion in assays relevant to vascular development. PDCD10-depleted HUVECs showed defective function in a 3D angiogenesis assay. Endothelial cells plated in a collagen matrix spontaneously organize into complex multicellular capillary-like networks with lumens (38), but cells depleted of PDCD10 failed to organize themselves into a lumenized network (Supplemental Figure 4, A and B). We explored potential downstream signaling pathways using this assay. A growing body of evidence suggests that PDCD10 interacts with the GCKIII subfamily of serine-threonine kinases (16, 21–23); we used siRNA to deplete cells of each of the subfamily members (Supplemental Figure 3). We observed no effect on lumen formation with the knockdown of STK25, STK24, or MST4 in HUVECs (Supplemental Figure 4C).

Pdcd10 functionally associates with GCKIII in lumen formation. Because the GCKIII family members may be functionally redundant, we sought to validate the importance of the PDCD10-GCKIII interaction in vivo and in a simpler genetic model. We chose the fruit fly, *Drosophila melanogaster*, in which the GCKIII family is represented by

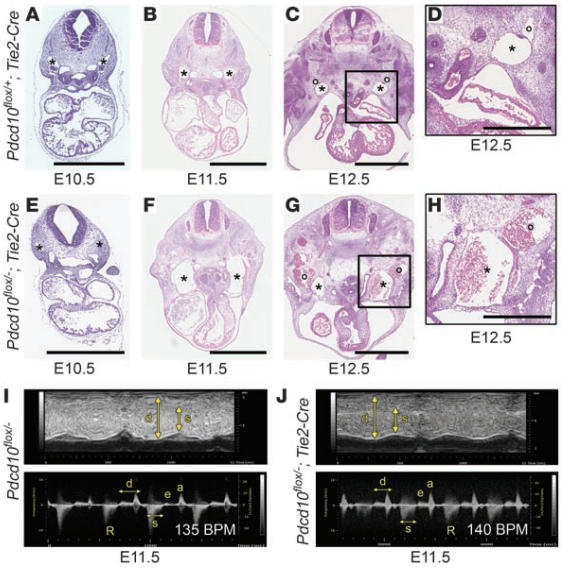

Figure 1
Pdcd10 is required in the endothelium for venous integrity. (**A**–**H**) H&E staining of developmental time course of *Pdcd10* endothelial knockout. *Pdcd10*$^{flox/+}$*;Tie2-Cre* is shown in **A**–**D**. *Pdcd10*$^{flox/–}$*;Tie2-Cre* is shown in **E**–**H**. Close-up images of the cardinal vein at E12.5 are shown in **D** and **H**. Asterisks denote the cardinal veins. Circles denote the external jugular veins. (**I** and **J**) Echocardiography of hearts from *Pdcd10*$^{flox/–}$ (**I**) and *Pdcd10*$^{flox/–}$*;Tie2-Cre* (**J**) mice at E11.5. Top panels show M-mode images of hearts contracting over time. Bottom panels show waveforms corresponding to blood flow across the atrioventricular valves. s, systole; d, diastole; e, early filling; a, atrial contraction; R, valvular regurgitation. Scale bars: 1 mm (**A**–**C** and **E**–**G**); 500 μm (**D** and **H**). $n \geq 6$ embryos at each age.

a single protein, GCKIII. This model avoids the complexity of human or mouse, which has 3 GCKIII kinases, or zebrafish, which has 2 orthologs for *Pdcd10*, 2 orthologs for *STK25*, and single orthologs for *STK24* and *MST4* (23). Furthermore, the *Drosophila* genome contains a single ortholog of *PDCD10*, but no orthologs for *KRIT1* or *CCM2*. Thus, *Drosophila* represents a simple model organism for studying Pdcd10-specific biology. To ensure that the biochemical interaction between PDCD10 and GCKIII was conserved in *Drosophila*, we performed immunoprecipitation assays with the *Drosophila* proteins. *Drosophila* Pdcd10 binds to GCKIII (Supplemental Figure 4D) in a manner analogous to that of human, mouse, or zebrafish protein (21, 23). A human disease PDCD10 mutation exists, which deletes 18 amino acids crucial for PDCD10-GCKIII binding (21). Removal of the analogous 18 amino acids from the *Drosophila* Pdcd10 protein abrogated binding to GCKIII (Supplemental Figure 4D).

Whereas *Drosophila* do not develop a vascular system, they do form a branched, lumenized network of tubes in the tracheal (respiratory) system. This epithelial network requires coordinated cell-cell interactions and specialized cell-cell junctions, analogous to the mammalian vascular system (39, 40). To determine the necessity of Pdcd10 in developing fly tracheal tubes, we expressed a dsRNA directed against *Pdcd10* (41) under the control of the tracheal-specific *Breathless* promoter (42) using the GAL4-UAS system (43). We found that tracheal tubes lacking Pdcd10 grow and branch normally, but fail to lumenize and fill with air (Supplemental Figure 5), indicating that Pdcd10 is required for normal lumen formation in fly tracheal tubes as it is in human endothelial tubes. This effect is highly penetrant; nearly all dsRNA-expressing flies show lack of lumenization in multiple tracheal tubes (Supplemental Figure 4E). The specificity of this effect is confirmed, as it could be rescued by coexpression of *Drosophila* Pdcd10 in RNAi-expressing cells (Supplemental Figure 4E). Notably, coexpression of the 18–amino acid deletion form of *Drosophila* Pdcd10, which does not bind to GCKIII, fails to rescue this phenotype (Supplemental Figure 4E). We used the same RNAi strategy to inactivate *GCKIII* (44) in the developing tracheal system. Tracheal tubes lacking GCKIII exhibit failure of lumenization (Supplemental Figure 5), and the phenotype appears very similar to that of Pdcd10-deficient tubes. Thus, Pdcd10 is essential for normal lumen formation in the absence of Krit1 and Ccm2 and in a manner that requires interaction with GCKIII kinases.

Our experiments in *Drosophila* suggested that GCKIII kinases are required for lumen formation but that functional redundancy in mammalian cells may have accounted for the lack of a lumen formation defect when any single kinase was lost. We therefore performed combinatorial knockdown experiments for pairs of the GCKIII kinases. Consistent with our hypothesis, we found that the loss of STK25, if coupled with the loss of either STK24 or MST4, was sufficient to reproduce the lumen formation defects seen with PDCD10 depletion (Supplemental Figure 4). Thus, PDCD10 interaction with GCKIII kinases is critical in lumen formation.

LOH of either Pdcd10 or Ccm2 causes murine cavernous malformations that phenocopy human CCMs. Pdcd10 and Ccm2's functions clearly differ in embryonic development, in endothelial cell culture, and in signaling, and Pdcd10 is necessary for lumen formation in a system that lacks Ccm2 or Krit1. The 3 genes, however, are linked

Table 2
Loss of *Pdcd10* in the endothelium leads to embryonic death after E12.5

Cross	*Pdcd10*$^{flox/flox}$ × *Pdcd10*$^{+/–}$*;Tie2-Cre*			
Genotype	***Pdcd10***$^{flox/+}$	***Pdcd10***$^{flox/–}$	***Pdcd10***$^{flox/+}$***;Tie2-Cre***	***Pdcd10***$^{flox/–}$***;Tie2-Cre***
No. of progeny				
E9.5	14	14	7	11
E12.5	13	28	16	16
E15.5	8	8	20	0
P21	26	20	20	0

Live offspring by genotype at embryonic and postnatal time points resulting from matings between *Pdcd10*$^{flox/flox}$ and *Pdcd10*$^{+/–}$*;Tie2-Cre* parents.

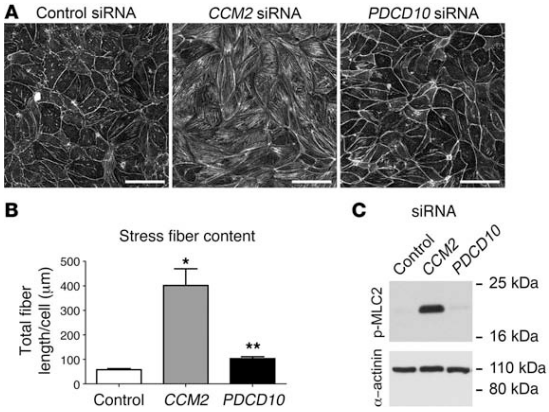

Figure 2
PDCD10 differs from CCM2 in downstream signaling. (**A**) Phalloidin staining of human microvascular endothelial cells treated with siRNA directed against *CCM2*, *PDCD10*, or nonsense control. (**B**) Quantification of stress fiber response of HMVEC cells. Stress fiber content is determined by adding the total length of stress fibers divided by the total number of cells. Results indicate mean ± SEM and are representative of at least 3 independent experiments. $^{*}P < 0.001$ versus control or *PDCD10*; $^{**}P$ = NS versus control. (**C**) Immunoblot for phospho-myosin light chain-2 (with α-actinin immunoblot as a loading control). Results are representative of 3 independent experiments. Scale bars: 100 μm.

to the same human disease. Limited human genetics suggested an association between LOH and CCM disease, so we investigated whether *Pdcd10* and *Ccm2* share this genetic mechanism for causing disease. To control the timing of the endothelial "second-hit," we used a drug-inducible Cre strain under the control of the *PDGF-B* promoter. This *PDGFb-iCreER*^{T2} strain expresses a Cre recombinase activated only after administration of the drug tamoxifen. Consistent with the original report describing this recombinase (37), we found that the administration of tamoxifen on the first postnatal day (P1) led to efficient, endothelial-specific recombination throughout the entire brain vasculature (Supplemental Figure 6). The induction of endothelial LOH of either *Pdcd10* or *Ccm2* by this Cre at birth resulted in CCMs in mice as early as 1 month of age (Figure 3). Induction of endothelial LOH of either *Pdcd10* or *Ccm2* resulted in a spectrum of vascular malformations, from capillary telangiectasias, to isolated caverns, to multiple back-to-back caverns with thrombosis, hemorrhage, and formation of secondary channels (Supplemental Figure 7). Loss of protein product via LOH was confirmed by antibody staining (Supplemental Figure 8). The retinal vasculature is another location for human CCMs, and murine cavernous malformations were also observed in mouse retinal vasculature (Supplemental Figure 9). To formally prove LOH in the endothelium of these CCMs, we performed laser capture microdissection to obtain tissue-specific DNA as previously done in human studies of CCM (28). We found that DNA from lesion endothelium had lost the conditional allele for either *Pdcd10* or *Ccm2*, confirming LOH, whereas this allele could still be detected in adjacent neuronal tissue (Figure 3). In contrast, loss of *Ccm2* in neural tissues using Nestin-Cre did not result in the development of vascular malformations (Supplemental Figure 10).

We characterized the histopathologic features of cavernous malformations in mice with induced endothelial loss of either *Pdcd10* (Figure 4) or *Ccm2* (Figure 5). We compared mouse CCMs with surgical specimens from CCM patients with germline mutations of either *PDCD10* (Figure 4) or *CCM2* (Figure 5). Cavernous malformations in these induced mouse models share all of the key histologic features of CCM lesions with human specimens. Furthermore, both *Pdcd10* and *Ccm2* resulted in identical pathologic findings for all of these defining characteristics in both human and mouse (Table 3). Mouse specimens showed numerous

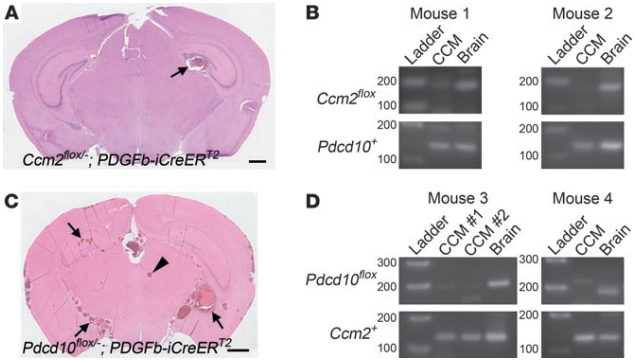

Figure 3
Cavernous malformations result from LOH of either *Ccm2* or *Pdcd10*. (**A**) Cavernous malformation (arrow) shown in an H&E-stained section of brain cerebrum from a mouse with induced endothelial knockout of *Ccm2*. (**B**) Confirmation of LOH of *Ccm2* in 2 mice with loss of *Ccm2*^{flox} allele by PCR, compared with *Pdcd10* wild-type allele as a control. (**C**) Cavernous malformations (arrows) and a less complex telangiectasia (arrowhead) shown in an H&E-stained section of brain cerebrum from a mouse with induced endothelial knockout of *Pdcd10*. (**D**) Confirmation of LOH of *Pdcd10* in 2 mice by PCR with loss of *Pdcd10*^{flox} allele compared with *Ccm2* wild-type allele as a control. Samples in **B** and **D** were obtained via laser capture microdissection of sectioned mouse brains. Scale bars: 1 mm.

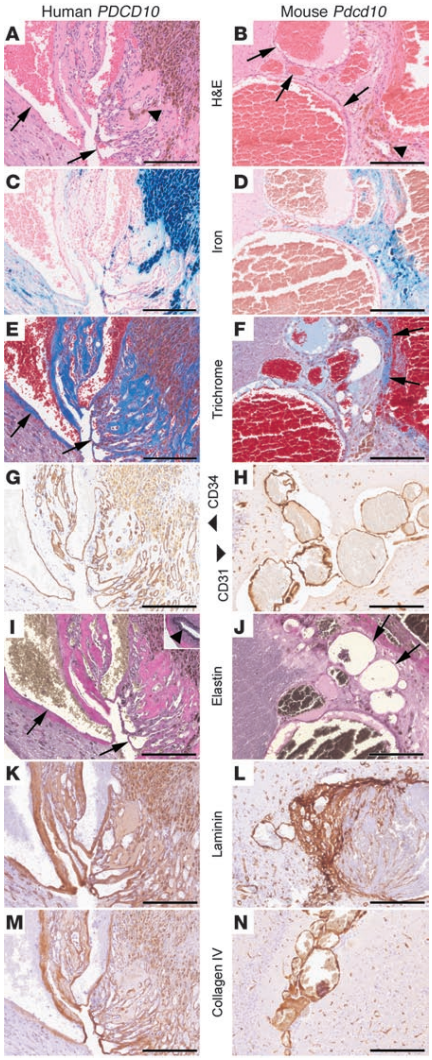

Figure 4
Pathologic analysis of mouse and human *PDCD10*-associated CCM. Paired analysis of histologic sections with human tissue on the left and mouse on the right. (**A** and **B**) H&E staining revealing back-to-back vascular channels (arrows) and hemosiderin pigment (arrowheads) in surrounding tissues. (**C** and **D**) Iron (blue) detected by Prussian blue stain highlights hemosiderin deposits in macrophages and surrounding brain tissue. (**E** and **F**) Fibrous matrix deposits (blue) identified by Masson's trichrome staining with fibrous tissue surrounding vascular channels (arrows) and in surrounding gliotic brain. (**G** and **H**) Endothelial staining for CD34 (**G**) or CD31 (**H**) is positive in the cells lining the channels. (**I** and **J**) Elastin staining shows that vascular channels lack elastic laminae (arrows) unlike normal vessels of similar caliber (arrowhead, inset in **I**). The fibrous matrix surrounding channels includes laminin (**K** and **L**) and collagen IV (**M** and **N**). Scale bars: 200 μm.

vascular channels of variable diameter (Figure 4, A and B, and Figure 5, A and B), some of them with organized thrombi. Immunohistochemical stains for endothelium highlighted endothelial cells in the channels, with focal attenuation or loss of endothelial cells in larger channels (Figure 4, G and H, and Figure 5, G and H). Iron stain highlighted the presence of hemosiderin-laden macrophages and hemosiderin in the wall of the channels as well as in the periphery and brain tissue (Figure 4, C and D, and Figure 5, C and D). Additionally, we also examined gliosis, trichrome staining, elastin, laminin, and collagen type IV, and these features were all identical between mouse and human lesions (Figure 4, E and N, Figure 5, E and N, and Table 3).

We also examined mouse lesions at the ultrastructural level using transmission electron microscopy. Murine cavernous malformations showed endothelial cells lining vascular channels with associated basal lamina (Figure 6A). Some of the larger channels showed segmental multilayering (lamellated appearance) of the basal lamina (Figure 6B). The most dilated channels showed focally marked attenuation of the endothelial cells (Figure 6C); however, tight junctions were identified between cells, and definitive gaps were not seen. Connective tissue composed mainly of collagen fibers separated the vascular channels (Figure 6D). Pericytes or astrocytic foot processes were missing, as seen in human lesions. Foci of mononuclear inflammatory cells were also seen (Figure 6E), including hemosiderin-laden macrophages (Figure 6F). Ultrastructural analysis of murine CCM lesions was similar to that described in human CCMs (45), further solidifying the fidelity of the mouse model to the human disease.

Murine cavernous malformations can be detected and followed noninvasively by MRI. MRI is used to document the natural history of human cavernous malformations and will be necessary for prospective therapeutic trials in both mice and humans. We thus employed monthly live MRI studies to follow the onset and progression of disease in mice until at least 6 months of age (Figure 7). As in humans (24), mice lacking *Pdcd10* had an earlier onset of disease, with a more severe phenotype than *Ccm2*. All *Pdcd10* mice studied at 1 month of age had lesions, whereas no *Ccm2* mice had yet developed lesions by 2 months of age (Figure 7K). Mice with *Pdcd10* mutations had a greater disease burden when assessed by total lesion burden (Figure 7L) or by number of complex lesions (increased signal intensity within the lesion; Figure 7M). Cavernous malformations were fully penetrant in mice with *Ccm2* LOH at 6 months of age and most had lesions at 4 months, at which time the disparity between the genotypes began to narrow. This parity reflected not only the increased burden of disease in *Ccm2*, but also the onset of death in the most severely affected *Pdcd10* mice. Mice of both genotypes began to die of hemorrhage, but mortality was greater in mice with LOH for *Pdcd10* (Figure 7N), a finding that reflects the reported experience in humans (24).

Discussion

Although CCM has been associated with mutations in 3 distinct loci, it has been clinically treated as a single pathophysiologic entity. In this manuscript, we describe for what we believe is the first time the pathologic features of CCM in a genotype-specific manner. We

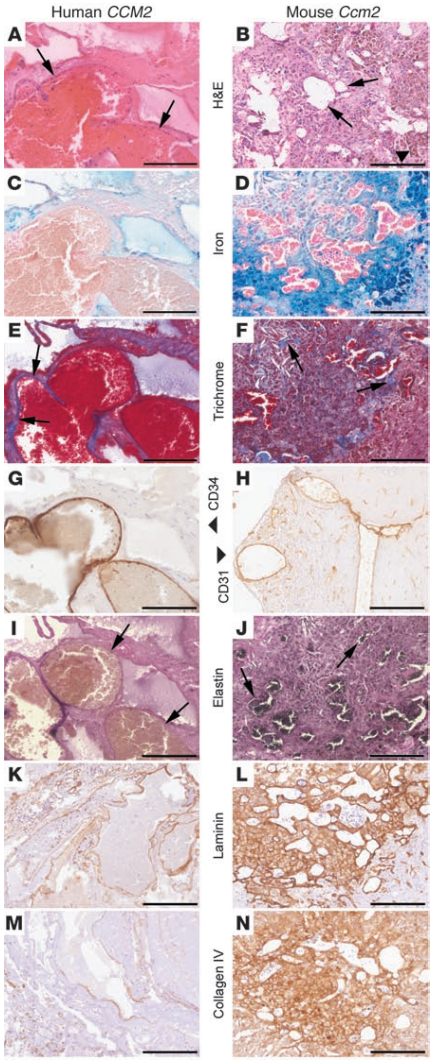

Figure 5
Pathologic analysis of mouse and human *CCM2*-associated CCM. Paired analysis of histologic sections with human tissue on the left and mouse on the right. (**A** and **B**) H&E staining revealing back-to-back vascular channels (arrows) and hemosiderin pigment (arrowhead) in surrounding tissues. (**C** and **D**) Iron (blue) detected by Prussian blue stain highlights hemosiderin deposits in macrophages and surrounding brain tissue. (**E** and **F**) Fibrous matrix deposits (blue) identified by Masson's trichrome staining with fibrous tissue surrounding vascular channels (arrows) and in surrounding gliotic brain. (**G** and **H**) Endothelial staining for CD34 (**G**) or CD31 (**H**) is positive in the cells lining the channels. (**I** and **J**) Elastin staining shows that vascular channels lack elastic laminae (arrows). The fibrous matrix surrounding channels includes laminin (**K** and **L**) and collagen IV (**M** and **N**). Scale bars: 200 μm.

find that mutations of both *PDCD10* and *CCM2* result in a common pathologic expression of disease in both humans and mice. Surprisingly, this common disease endpoint does not constitute proof of a common disease mechanism. Whereas our previous work and the work of others found that Ccm2 and Krit1 play similar roles in embryonic development, in vitro cell biology, and cell signaling (9, 10, 12, 13), these roles differ from those we observe with Pdcd10. Unlike Krit1 and Ccm2, Pdcd10 is not required for development of the branchial arch arteries that connect the heart to the aorta. Rather, Pdcd10 has an essential, nonendothelial role in development not shared with Krit1 or Ccm2 as well as an essential function in venous maturation. We further observe differences in cell biology and signaling between PDCD10 and KRIT1 or CCM2; whereas the loss of KRIT1 or CCM2 leads to RhoA activation, increased Rho kinase activity, myosin light chain phosphorylation, and actin stress fiber formation (9, 12, 13), we do not observe activation of this signaling pathway in cells depleted of PDCD10. Instead, we found that PDCD10 signals primarily through the GCKIII family of kinases.

The similarity in human CCM disease caused by mutations in *KRIT1*, *CCM2*, and *PDCD10* have led to an assumption that the proteins encoded by these genes function in a common signaling pathway. This assumption has been supported by experimental evidence showing binding between ectopically expressed, epitope-tagged proteins (7, 8). However, the complexities of signaling pathways and pathophysiology allow for multiple mechanisms to converge on a common disease phenotype (Figure 8A). An example is hypertrophic cardiomyopathy, which was considered 1 disease until molecular genetics revealed that 2 different mechanisms (sarcomere function or metabolism), each affected by distinct genes, both result in pathologic hypertrophy (Figure 8B and ref. 46). We propose that a similar scenario is involved in the pathogenesis of CCM (Figure 8C).

There is controversy concerning the signaling pathways affected by PDCD10. Several reports suggest an essential role for binding GCKIII family serine-threonine kinases (16, 21–23). However, a recent characterization of mice carrying a different conditional allele of *Pdcd10* showed that the loss of Pdcd10 in endothelial cells substantially blocks VEGFR2 signaling and inhibits the earliest stages of developmental angiogenesis (47). The implication of VEGFR2 signaling through MAP kinases agrees with a previous report linking GCKIII kinases and ERK signaling (20). Our data contrast with these reports; we observe that the absence of Pdcd10 in vivo leads to a localized vascular defect at a much later developmental stage, inconsistent with a panendothelial block of VEGF signaling. In cell culture, we have not found any interaction between PDCD10 and VEGF or ERK signaling (Supplemental Figure 11). We suspect that this disparity may be due to a difference in knockout strategy; however, our confidence in our allele is bolstered by our ability to induce CCM disease. Our data support the model that PDCD10 signals through the GCKIII family kinases, as we have observed in human endothelial cells and in *Drosophila* that PDCD10 binds to GCKIII family kinases and both are required for lumen formation. Previous reports have further suggested that GCKIII signals through RhoA to converge

Table 3
Pathologic findings in human and murine CCMs

Genotype	Human *CCM2*	Murine *Ccm2*	Human *PDCD10*	Murine *Pdcd10*
Trichrome	+	+	++	++
Iron	+	+	++	++
Elastin	–	–	–	–
CD34	+	NA	+	NA
CD31	NA	+	NA	+
Laminin	+	+	+	+
Collagen IV	+	+	+	+

The pathologic findings compared for human and murine CCMs associated with mutations of either *CCM2* or *PDCD10*.

with KRIT1/CCM2 signaling (23). By direct comparison of Ccm2 and Pdcd10 in mouse and cell biology, however, our data suggest that PDCD10 signaling is distinct from the CCM2-RhoA axis.

The nature and severity of disease in familial forms of CCM in comparison with sporadic CCM suggested a genetic mechanism consistent with Knudson's 2-hit hypothesis (33): LOH for a CCM gene induces lesions. Limited evidence to support this theory has come from a few human surgical samples amid multiple cases in which the second genetic hit could not be found (27, 28). Further supportive evidence comes from mice with heterozygous mutations for *Krit1* or *Ccm2* that have been mated into strains with high rates of spontaneous mutations. Mice heterozygous for *Krit1* develop CCM lesions on either a p53- or Msh2-null background, whereas mice heterozygous for *Ccm2* develop lesions only on the p53-, but not the Msh2-null background (35, 36). Whereas these models provide suggestive evidence of LOH and employ stochastic events to induce CCM formation, LOH was not demonstrated at either locus, nor can the LOH hypothesis be supported for all CCM genes, as *Ccm2*$^{+/-}$;*Msh2*$^{-/-}$ mice do not develop CCMs. These models also do not rule out a role for mutations in other, non-CCM genes and do not control tissue specificity of mutation. The penetrance of CCMs in these models is incomplete, complicating the use of these models in prospective trials to study therapeutics or natural history of CCM disease. Concurrent development of neoplasms in both the p53- and the Msh2-null backgrounds also adds confounding physiological stressors and increases the mortality of the animals. In contrast, we employ a strategy that allows direct testing of the LOH mechanism in CCM disease. Using an inducible Cre-recombinase, we have targeted gene-specific LOH for both *Pdcd10* and *Ccm2* to the endothelium of mice. In the case of both genes, we have found that LOH is sufficient to cause a fully penetrant CCM phenotype that recapitulates every key pathologic and radiologic hallmark of human disease.

Much work remains to translate the observations and insights regarding disease signaling mechanisms into viable therapeutic strategies in patients. This work underscores the importance of carefully considering disease mechanisms in a genotype-specific manner. The availability of faithful, genotype-specific, and highly penetrant mouse models of CCM disease unlocks the tremendous opportunities to study the natural history of lesion genesis and progression as well as opportunities for preclinical testing of therapeutic interventions. In order for mouse models of CCM disease to be useful in informing human studies, the same tools used to follow patients with CCM need to be developed for serial observation of affected mice. We have demonstrated that noninvasive MRI of live mice, the same modality used to follow CCM in humans, can detect and follow murine CCMs. Although our mouse models share a measurable mortality, as with humans, they are compatible with prolonged survival and serial, noninvasive observation. The ability to follow these mice noninvasively over time is a crucial prerequisite for judging the effectiveness of any preclinical therapeutic strategy in the future and for testing the timing and intensity of LOH required for lesion formation. Our mouse models of CCM phenocopy human disease closely, supplanting previously available surrogate phenotypes, and are a powerful new tool in the armamentarium to decipher and combat CCM disease.

Methods

Mouse strains. The *Ccm2* conditional knockout mice have been previously described (9). A construct for the conditional allele of *Pdcd10* was derived from genomic sequence obtained from a BAC clone (RP22 library; Invitrogen). The construct extended from a SacII site 5′ of exon 4 through an ApaI site 3′ of exon 8. The construct contained inserts as outlined in Supplemental Figure 1, including LoxP sequences at a KasI site just 5′ of exon 4 and at a EcoRI site just 3′ of exon 8. All mice were backcrossed into the C57BL/6J strain. Experiments performed prior to the fifth cross were performed with littermate controls. *LacZ* reporter mice (R26R1), *Tie2-Cre*

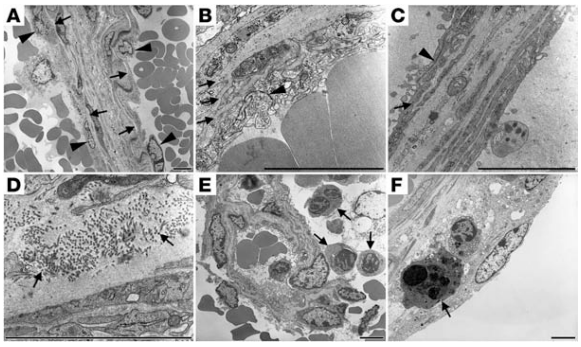

Figure 6
Ultrastructural findings in murine cavernous malformations. (**A**) Dilated vascular channels are lined by endothelial cells (arrowheads) with associated basal lamina (arrows). (**B**) Occasional channels have segments with a multilayered appearance (arrows indicate lamellae of endothelium with basal laminae). Tight junctions appear intact (arrowhead). (**C**) Focal areas of endothelial attenuation are observed (arrow) without apparent gaps or disruption of tight junctions (arrowhead indicates a junctional complex). (**D**) Channels are separated by loose connective tissue composed mostly of collagen (arrows). (**E**) Foci of mononuclear inflammatory cells are present (arrows). (**F**) Hemosiderin-laden macrophages (arrow) are among the inflammatory cells observed. Images are representative of 5 lesions from 3 *Pdcd10* mice. Scale bars: 4 μm.

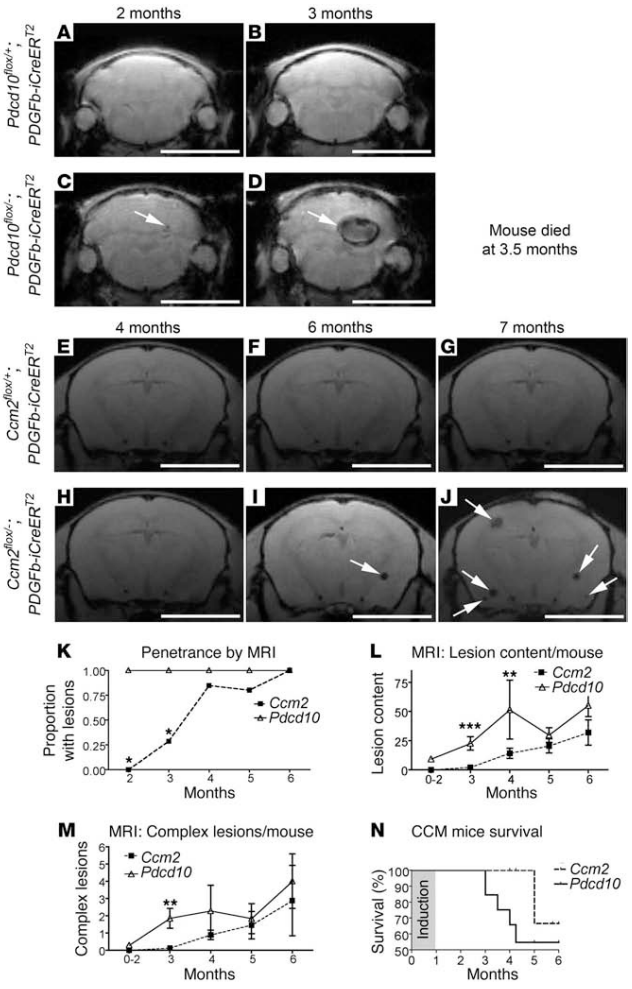

Figure 7
Natural history of murine CCM by MRI — *Pdcd10* onsets earlier and is more severe than *Ccm2*. (**A**–**D**) Live MRI scans of the same *Pdcd10*$^{flox/+}$;*PDGFb-iCreER*^{T2} mouse at 2 months and 3 months (**A** and **B**) and its *Pdcd10*$^{flox/-}$;*PDGFb-iCreER*^{T2} littermate (**C** and **D**). Both mice were given tamoxifen at birth. (**E**–**J**) Live MRI scans of the same *Ccm2*$^{flox/+}$;*PDGFb-iCreER*^{T2} mouse (**E**–**G**) and its *Ccm2*$^{flox/-}$;*PDGFb-iCreER*^{T2} littermate (**H**–**J**) at 4, 6, and 7 months. Both mice were given tamoxifen at birth. Arrows indicate CCM lesions. (**K**) Disease penetrance (proportion affected) by age in *Ccm2* and *Pdcd10* induced knockout mice as assessed by live MRI. (**L**) Lesion burden assessed as total number of lesions observed on each tomographic view (slice) of the MRI per mouse. (**M**) Number of complex lesions (lesions with bright cores) per mouse. (**N**) Kaplan-Meier survival curve of *Ccm2* and *Pdcd10* induced knockout mice. For **K**–**N**, $n = 11$ *Ccm2*, $n = 13$ *Pdcd10*. Data in **L** and **M** represent mean ± SEM. $^{*}P < 0.01$; $^{**}P < 0.05$; $^{***}P < 0.001$. Scale bars: 1 mm.

mice, and *PDGFb-iCreER*^{T2} mice were generously provided by Phil Soriano (Fred Hutchinson Cancer Research Center, Seattle, Washington, USA, and Mount Sinai School of Medicine, New York, New York, USA), Masashi Yanagisawa (University of Texas Southwestern Medical Center at Dallas, Dallas, Texas, USA), and Marcus Fruttiger (University College London Institute of Ophthalmology, London, United Kingdom) via Holger Gerhardt (London Research Institute — Cancer Research UK, London, United Kingdom), respectively. *HPRT-Cre*, *Nestin-Cre*, and *Tomato-EGFP* reporter mice were obtained from The Jackson Laboratory. Genotypes were determined by PCR analysis of genomic DNA isolated from either ear biopsies or yolk sac tissues using primers outlined in Supplemental Figure 1. Primer sequences were as follows: primer W: 5′-GCAATCCATCTTGTTCAATGGC-3′, primer X: 5′-CGTAGGTCAGGGTGGTCACG-3′, primer Y: 5′-TGAAAGAGGACATACTGGAGAGGC-3′, primer Z: 5′-AAGGACAAGAAAGCACTGTTGACC-3′. Tamoxifen (Sigma-Aldrich) was resuspended in corn oil (Sigma-Aldrich), and 40 ng was given as an i.p. injection to mouse pups on perinatal day 1.

MRI of mouse brains. All MRI experiments were conducted on a 7T Bruker Biospec 70/30 USR scanner (Bruker Biospin MRI Inc.) equipped with a BGA12S gradients set. A combination of volume-transmit–only radio frequency coil (internal diameter: 72 mm) and a quad-surface-receive–only coil (internal diameter: 1.5 cm) were used. For live scans, mice were anesthetized in 2.5% isoflurane and then placed into the scanner on top of circulating heated water. During the scans, mice were monitored for temperature and respiration, with isoflurane concentration and water bath temperature adjusted to maintain a body temperature between 35.8°C and 37.6°C and respiration between 75 and 100 breaths/min. A gradient recalled echo sequence was used to acquire coronal slices spanning the whole brain. Sequence parameters were as follows: repetition time, 328 ms; echo time, 5.4 ms; flip-angle, 40°; 12 averages, in-plane-resolution, 125 μm × 125 μm; and slice thickness, 0.5 mm.

For postmortem specimens, mouse skulls were fixed in 4% formaldehyde for at least 3 days before the brain was imaged with the skull intact. Postmortem MRI scanning allows a high-resolution coverage of the brain at the expense of longer scan time. High-resolution 3D gradient echo was acquired using the same scanner configuration described above, with isotropic voxel size of 78 μm × 78 μm × 78 μm over 9 hours. Other sequence parameters were as follows: repetition time, 250 ms; echo time, 7.5 ms; flip angle, 30°; and 2 averages.

Histology. Embryo and mouse CCM lesions were studied with antibodies to PECAM (1:250 dilution, clone MEC13.3; BD Biosciences) and PDCD10 (1:50 dilution, Prestige Antibody; Sigma-Aldrich). Improved visualization on paraffin sections was obtained using a biotinylated tyramide signal

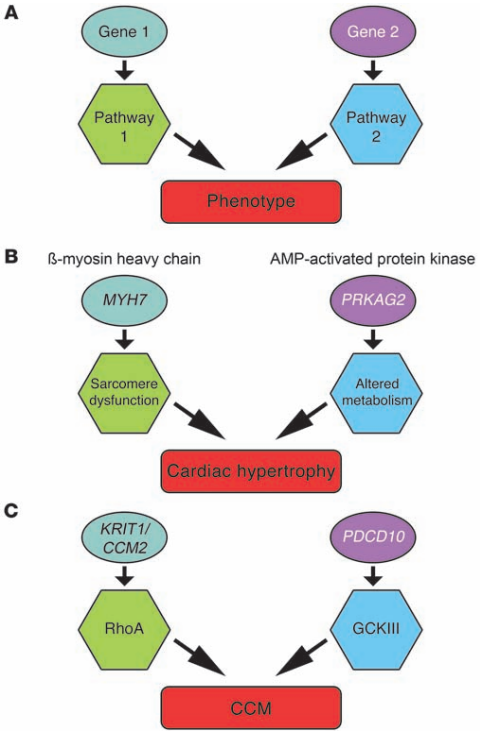

Figure 8
Convergence of different mechanistic pathways in common pathology. (**A**) Proposed schema for different genes acting on separate mechanistic pathways, yet ultimately resulting in a common expression of disease. (**B**) Genetic studies of hypertrophic cardiomyopathy highlight genes that can be grouped broadly into 2 separate mechanistic pathways: sarcomeric proteins such as β-myosin heavy chain (MYH7), and metabolic genes including adenosine monophosphate-activated protein kinase (PRKAG2). (**C**) Studies of mouse development, cell biology, and signaling suggest that KRIT1 and CCM2 signal through RhoA GTPase, while PDCD10 signals through GCKIII kinases to lead to cavernous malformations.

amplification (TSA) kit (PerkinElmer) according to the manufacturer's instructions. To demonstrate tissue specificity of *PDFGb-iCreER*^{T2}, brains from mice carrying a *LacZ* reporter allele were fixed and then stained with X-gal as previously described (48). Brains from mice carrying the *Tomato-EGFP* reporter allele were fixed and then embedded into OCT (Fisher Scientific) for fluorescent frozen sections. H&E staining of embryos was performed using standard procedures.

For histology of adult mouse brains, mouse skulls were fixed in 4% formaldehyde for at least 3 days or zinc-buffered formalin overnight before the brain was removed and sliced into 4 coronal sections. These sections were embedded into paraffin by standard techniques. Prussian blue staining for iron and Masson's trichrome staining of mouse brain sections were performed using the Artisan system (DAKO) according to manufacturer's instructions. Staining for elastin, laminin, and collagen IV was performed by the Immunohistochemistry Research and Development Lab at ARUP Laboratories. Human CCM samples were stained in the same way as adult mouse brains except for CD34 staining, which was performed by the Central Labs at Intermountain Medical Center (Murray, Utah, USA).

Fluorescent staining of mouse retinas. Mice were anesthetized using Avertin (2,2,2-tribromoethanol, 0.4 mg/g; Acros Organics) and perfused with fluorescently conjugated tomato lectin (Vector Labs) as previously described (49) at a dose of 5 μg/g body weight. After 5 minutes, mice were perfused with saline and then with 4% formaldehyde. Retinas were then extracted, stained, and mounted as previously described (50).

Analysis of mouse embryos. Confocal immunofluorescence of embryos and fetal ultrasound were performed as previously described (9).

Transmission electron microscopy. Samples were fixed in 1% formaldehyde, 2.5% glutaraldehyde in 0.1 M sodium cacodylate buffer with 8 mM $CaCl_2$ and 2.4% sucrose, pH 7.4, for at least 3 days. Samples were then rinsed in 0.1 M cacodylate buffer, postfixed in 2% osmium tetroxide in 0.1 M cacodylate buffer, rinsed in type I water, and then enbloc stained with saturated aqueous uranyl acetate. Samples were dehydrated through a graded series of ethanols, followed with final dehydration in acetone, and then infiltrated and embedded in an epoxy resin.

Thick sections and thin sections were cut on a Leica EM UC6 ultramicrotome (Leica Microsystems). The thick sections were cut with glass and the thin sections were cut with a diatome diamond knife. Thick sections were dried on glass slides and were stained with 1% toluidine blue O in 1% aqueous sodium borate. Thin sections were placed on 135 mesh copper hex grids and stained sequentially with saturated aqueous uranyl acetate and Reynolds lead citrate.

Sections were examined on an FEI Tecnai T-12 transmission electron microscope (FEI) at 80 KV. Images were taken on Kodak 4489 electron microscope film, developed with Kodak D-19 developer, fixed, washed, and dried. The negatives were scanned on an Epson Perfection Photo 4990 flatbed scanner.

Cell culture. HUVEC and HMVEC were obtained from Lonza and grown according to the manufacturer's instructions in EGM-2 media (HUVEC) or EGM-2MV media (HMVEC). Human embryonic kidney (HEK 293T) cells (ATCC) were grown in DMEM (Gibco; Invitrogen) with 10% fetal bovine serum (Bio-West) supplemented with antibiotics. EAHY cells were generously provided by Andrew Weyrich (University of Utah) and were grown in DMEM with 10% fetal bovine serum and HAT supplement (Sigma-Aldrich).

Transfection of ECs with siRNAs. Human *CCM2* and *PDCD10* siRNAs were obtained from Dharmacon. Luciferase GL2 duplex or nontargeting siRNA (Dharmacon) were used as controls. EC transfection with siRNAs was carried out in growth media with 1% serum. Details of the siRNA transfection protocol have been described previously (51).

RT-PCR. Total RNA was extracted from EC vasculogenesis assay at indicated time points or from siRNA-treated ECs using the ToTALLY RNA Isolation Kit (Ambion) according to the manufacturer's instructions. RNA (1 μg) was reverse transcribed using AccuScript High Fidelity 1st strand cDNA synthesis kit (Stratagene; Agilent). RT-PCR amplification used the following primers: forward: 5′-AGACTTCACGGAGTCCCTTC-3′, reverse: 5′-AGAAGGTCTGAAGTATTAAGTTGG-3′. For quantitative real-time PCR, total RNA was extracted from cultured endothelial cells or from embryos using the NucleoSpin RNA II Kit (Clontech) according to the manufacturer's instructions. Reverse transcription was performed with random primers using the RETROScript Kit (Ambion). Quantitative PCR was performed with TaqMan assays (Applied Biosystems) for human *CCM2*, *PDCD10*, *GAPDH*, *STK24*, *STK25*, and *MST4* or mouse *Pdcd10* and *Gapdh*. Quantification was performed by standard curve method, and

CCM2 and *PDCD10* transcripts were normalized to *GAPDH* for comparisons. RT-PCR primers for embryonic *Pdcd10* transcripts were as follows: primer 4F: 5′-TTCACCGAGTCCCTCCTTCG-3′; primer 7/8R: 5′-GAACACATTTATTGCCTTGCCATC-3′; primer 1F: 5′-AAGTCCGTGCCTCAGTTGCC-3′; and primer EGFP-R: 5′-TCCTCGCCCTTGCTCACC-3′.

Immunofluorescent cell staining. Glass chamber slides (Nalge Nunc; Thermo Fisher) were coated with human fibronectin (Biomedical Technologies Inc.), and transfected cells were seeded at 50,000 cells per well. Cells were fixed in 4% formaldehyde and actin cytoskeleton was visualized using fluorescently conjugated phalloidin (Molecular Probes; Invitrogen). Images were obtained with an Olympus FV300 confocal microscope.

Endothelial cell vasculogenesis in 3D collagen matrices. This assay was performed as previously described (9, 38).

Immunoprecipitation and Western blotting. An expressed sequence tag (EST) for human *PDCD10* (IMAGE: 3050540) was obtained from ATCC and cloned into a pcDNA3.1 Hygro$^+$ plasmid (Invitrogen) modified to encode an N-terminal FLAG tag. ESTs for *Drosophila Pdcd10* and *GCKIII* were obtained from the Drosophila Genomics Resource Center and cloned into a pcDNA3.1 Hygro$^+$ plasmid modified to encode an N-terminal FLAG tag (*Pdcd10*) or HA tag (*GCKIII*). PDCD10Δ18 constructs were made using nested PCR with primers designed to overlap and omit the 54 nucleotides encoding those 18 amino acids. Plasmids were transfected into EAHY or HEK 293T cells using Lipofectamine 2000 (Invitrogen) according to the manufacturer's instructions, with a reduced dosage of DNA and lipofectamine for EAHY cells. Two days after transfection, cells were scraped into lysis buffer (50 mM Tris-HCl at pH 7.5, 100 mM NaCl, 0.5% Triton X-100) supplemented with protease and phosphatase inhibitors and 1 mM DTT. A portion of cell lysate was retained as whole cell lysate and the rest precleared with normal mouse IgG conjugated to agarose beads (Santa Cruz Biotechnology Inc.) at 4°C for 1 hour, then incubated with anti-FLAG resin at 4°C for 2 hours. The beads were washed 3 times with lysis buffer, and bound proteins were eluted using Laemmli sample buffer. Presence of FLAG-tagged PDCD10 proteins was detected using the anti-FLAG M2 antibody (Sigma-Aldrich). Presence of HA-tagged GCKIII was detected using an anti-HA antibody (Santa Cruz Biotechnology Inc.). Near-infrared secondary antibodies (LI-COR Biosciences) were used to probe the blots, which were visualized using the Odyssey system (LI-COR Biosciences).

Rabbit polyclonal antibody against PDCD10 was from Proteintech Group. Rabbit antibodies against phospho-myosin light chain (Thr18/Ser19), phospho-VEGFR2 (Tyr1175), total VEGFR2, phospho-PLCγ (Tyr783), total PLCγ, phospho-ERK1/2 (Thr202/Tyr204), and total ERK1/2 were from Cell Signaling Technology. α-Actinin antibody (clone H-2) was from Santa Cruz Biotechnology Inc. HRP-conjugated secondary antibodies were from Jackson ImmunoResearch. Western blots were developed using the ECL Plus Western blotting reagent (GE Healthcare) and Kodak Biomax MR film.

Drosophila strains. The GAL4/UAS system was used for tissue-specific RNAi knockdown (43). The driver used was *btl-GAL4* (42), and RNAi targeting constructs v109453 (against *Pdcd10*) (41), v106841 (against *Pdcd10*) (41), and v49559 (against *GCKIII*) (44) were obtained from the Vienna Drosophila RNAi Center. For rescue experiments, full-length cDNAs for *Drosophila Pdcd10* were cloned into a pUAST transformation vector containing an attb site for site-specific transformation (52) provided by Carl Thummel (University of Utah). Transgenes were injected into docking sites VK00027 (53) and attp0016 (52) by Genetic Services Inc., and homozygous lines were established by standard methods.

For cDNA rescue experiments, flies homozygous for the cDNA rescuing construct on the third chromosome were crossed to a homozygous *btl-GAL4*, *UAS-GFP* driver line on the second chromosome to generate transheterozygote flies (*btl-GAL4*, *UAS-GFP/+*; *UAS-Rescue/+*). Males of this genotype were then crossed to virgin females homozygous for the RNAi targeting construct located on the second chromosome. GFP expression indicated the presence of the *btl-GAL4*, *UAS-GFP* transgenes. All of these larvae contain 1 copy of the RNAi targeting construct, and half also have the cDNA rescue transgene. Results shown used the v109453 line, which targets the 3′ UTR of *Pdcd10*. The v106841 line showed similar results.

Analysis of tracheal tube formation in Drosophila larvae. Animals were scored at the prewandering third instar larval stage for tracheal defects. Animals were graded by scoring air filling in primary sprouts emanating from the dorsal trunk. All primary sprouts were scored bilaterally (at least 12 per larva). The animals were categorized as having severe, moderate, or mild defects or wild-type if they had 3 or more of the following defects: (a) severe defects were truncations before the first bifurcation of the primary side branches or immediately after branching; (b) moderate defects represented gaps in air filling with filled tubes on both sides; (c) mild defects were loss of air filling only in the fine terminal tubes. In the event that more than 1 criterion was met, the more severe category was selected. If animals had fewer than 3 branches with a given defect, the less severe category was selected. Only animals with no defects were categorized as wild type.

Mouse and human experiments. All mouse experiments were approved by the University of Utah Institutional Animal Care and Use Committee. Human tissue samples were obtained with written informed consent and provided by Connie Lee and Amy Akers (Angioma Alliance, Norfolk, Virginia, USA) and Randy Jensen (University of Utah). Human experiments were approved by the Institutional Review Board of the University of Utah.

Statistics. For actin stress fiber content, and for in vitro lumen formation with GCKIII kinases, we performed ANOVA with Tukey's post hoc analysis with an α value of 0.05. For in vitro lumen formation time course for PDCD10, we performed statistical comparisons between treatment groups with a 2-tailed paired-sample *t* test with an α value of 0.05. For the tracheal tube formation rescue experiment, we performed a χ^2 test for independence with an α value of 0.05 (degrees of freedom = 9). For CCM penetrance and lesion content, we performed a 2-tailed *t* test with an α value of 0.05.

Acknowledgments

We thank N. London, S. Navankasattusas, L. Shi, Y. Xiong, C. Jensen, J. Zhu, D. Zurcher, A. Fang, T. Mleynek, and D. Lim for technical assistance; O. Abdullah and E. Hsu and the University of Utah Small Animal Imaging Facility; C. Rodesch and the University of Utah Cell Imaging/Fluorescence Facility; N. Chandler and the University of Utah Electron Microscopy Facility; S. Tripp and the Immunohistochemistry Research and Development Lab at ARUP Laboratories; J. Hansen at Central Labs at Intermountain Medical Center; K. Thomas and S. Odelberg for critical comments and helpful scientific discussions; and S. Chin for helpful scientific discussions. This work was funded by the US NIH (to G.E. Davis, M.M. Metzstein, K.J. Whitehead, and D.Y. Li), including training grant T32-GM007464 (to A.C. Chan and O.E. Ruiz), the Hellenic Cardiological Society (to N.A. Diakos), the American Heart Association (to K.J. Whitehead and D.Y. Li), the H.A. and Edna Benning Foundation, the Juvenile Diabetes Research Foundation, and the Burroughs Wellcome Fund (to D.Y. Li).

Received for publication July 16, 2010, and accepted in revised form March 2, 2011.

Address correspondence to: Kevin J. Whitehead, Room 4A100, 30 N 1900 East, Salt Lake City, Utah 84132, USA. Phone: 801.581.7715; Fax: 801.581.7735; E-mail: kevin.whitehead@u2m2.utah.edu. Or to: Dean Y. Li, Building 533 Room 4220, 15 N 2030 East, Salt Lake City, Utah 84112, USA. Phone: 801.585.5505; Fax: 801.585.0701; E-mail: dean.li@u2m2.utah.edu.

1. Otten P, Pizzolato GP, Rilliet B, Berney J. A propos de 131 cas d'angiomes caverneux (cavernomes) du S.N.C. repérés par l'analyse rétrospective de 24 535 autopsies. *Neurochirurgie*. 1989;35(2):82–83.
2. Vernooij MW, et al. Incidental findings on brain MRI in the general population. *N Engl J Med*. 2007;357(18):1821–1828.
3. Hasegawa T, McInerney J, Kondziolka D, Lee JY, Flickinger JC, Lunsford LD. Long–term results after stereotactic radiosurgery for patients with cavernous malformations. *Neurosurgery*. 2002;50(6):1190–1197.
4. Chappell PM, Steinberg GK, Marks MP. Clinically documented hemorrhage in cerebral arteriovenous malformations: MR characteristics. *Radiology*. 1992;183(3):719–724.
5. Burger PC, Scheithauer BW. *Tumors of the Central Nervous System*. Washington, DC, USA: American Registry of Pathology; 2007.
6. Wang H, Gujrati M. Pathology of cerebral cavernous malformations. In: Lanzino G, Spetzler RF, eds. *Cavernous Malformations of the Brain and Spinal Cord*. New York, New York, USA: Thieme Medical Publishers, Inc; 2008:22–25.
7. Faurobert E, Albiges-Rizo C. Recent insights into cerebral cavernous malformations: a complex jigsaw puzzle under construction. *FEBS J*. 2010;277(5):1084–1096.
8. Hilder TL, et al. Proteomic identification of the cerebral cavernous malformation signaling complex. *J Proteome Res*. 2007;6(11):4343–4355.
9. Whitehead KJ, et al. The cerebral cavernous malformation signaling pathway promotes vascular integrity via Rho GTPases. *Nat Med*. 2009;15(2):177–184.
10. Whitehead KJ, Plummer NW, Adams JA, Marchuk DA, Li DY. Ccm1 is required for arterial morphogenesis: implications for the etiology of human cavernous malformations. *Development*. 2004; 131(6):1437–1448.
11. Boulday G, et al. Tissue-specific conditional CCM2 knockout mice establish the essential role of endothelial CCM2 in angiogenesis: implications for human cerebral cavernous malformations. *Dis Model Mech*. 2009;2(3–4):168–177.
12. Stockton RA, Shenkar R, Awad IA, Ginsberg MH. Cerebral cavernous malformations proteins inhibit Rho kinase to stabilize vascular integrity. *J Exp Med*. 2010;207(4):881–896.
13. Glading A, Han J, Stockton RA, Ginsberg MH. KRIT-1/CCM1 is a Rap1 effector that regulates endothelial cell cell junctions. *J Cell Biol*. 2007; 179(2):247–254.
14. Borikova AL, et al. Rho kinase inhibition rescues the endothelial cell cerebral cavernous malformation phenotype. *J Biol Chem*. 2010;285(16):11760–11764.
15. Zawistowski JS, et al. CCM1 and CCM2 protein interactions in cell signaling: implications for cerebral cavernous malformations pathogenesis. *Hum Mol Genet*. 2005;14(17):2521–2531.
16. Fidalgo M, Fraile M, Pires A, Force T, Pombo C, Zalvide J. CCM3/PDCD10 stabilizes GCKIII proteins to promote Golgi assembly and cell orientation. *J Cell Sci*. 2010;123(pt 8):1274–1284.
17. Zhang J, Clatterbuck RE, Rigamonti D, Chang DD, Dietz HC. Interaction between krit1 and icap1alpha infers perturbation of integrin beta1-mediated angiogenesis in the pathogenesis of cerebral cavernous malformation. *Hum Mol Genet*. 2001;10(25):2953–2960.
18. Zawistowski JS, Serebriiskii IG, Lee MF, Golemis EA, Marchuk DA. KRIT1 association with the integrin-binding protein ICAP-1: a new direction in the elucidation of cerebral cavernous malformations (CCM1) pathogenesis. *Hum Mol Genet*. 2002;11(4):389–396.
19. Uhlik MT, et al. Rac-MEKK3-MKK3 scaffolding for p38 MAPK activation during hyperosmotic shock. *Nat Cell Biol*. 2003;5(12):1104–1110.
20. Ma X, et al. PDCD10 interacts with Ste20-related kinase MST4 to promote cell growth and transformation via modulation of the ERK pathway. *Mol Biol Cell*. 2007;18(6):1965–1978.
21. Voss K, et al. Functional analyses of human and zebrafish 18-amino acid in-frame deletion pave the way for domain mapping of the cerebral cavernous malformation 3 protein. *Hum Mutat*. 2009;30(6):1003–1011.
22. Goudreault M, et al. A PP2A phosphatase high-density interaction network identifies a novel striatin-interacting phosphatase and kinase complex linked to the cerebral cavernous malformation 3 (CCM3) protein. *Mol Cell Proteomics*. 2008;8(1):157–171.
23. Zheng X, et al. CCM3 signaling through sterile 20-like kinases plays an essential role during zebrafish cardiovascular development and cerebral cavernous malformations. *J Clin Invest*. 2010;120(8):2795–2804.
24. Denier C, et al. Genotype-phenotype correlations in cerebral cavernous malformations patients. *Ann Neurol*. 2006;60(5):550–556.
25. Sirvente J, Enjolras O, Wassef M, Tournier-Lasserve E, Labauge P. Frequency and phenotypes of cutaneous vascular malformations in a consecutive series of 417 patients with familial cerebral cavernous malformations. *J Eur Acad Dermatol Venereol*. 2009;23(9):1066–1072.
26. Labauge P, et al. Multiple dural lesions mimicking meningiomas in patients with CCM3/PDCD10 mutations. *Neurology*. 2009;72(23):2044–2046.
27. Akers AL, Johnson E, Steinberg GK, Zabramski JM, Marchuk DA. Biallelic somatic and germline mutations in cerebral cavernous malformations (CCMs): evidence for a two-hit mechanism of CCM pathogenesis. *Hum Mol Genet*. 2009;18(5):919–930.
28. Gault J, et al. Cerebral cavernous malformations: somatic mutations in vascular endothelial cells. *Neurosurgery*. 2009;65(1):138–144.
29. Pagenstecher A, Stahl S, Sure U, Felbor U. A two-hit mechanism causes cerebral cavernous malformations: complete inactivation of CCM1, CCM2 or CCM3 in affected endothelial cells. *Hum Mol Genet*. 2009;18(5):911–918.
30. Rigamonti D, et al. Cerebral cavernous malformations. Incidence and familial occurrence. *N Engl J Med*. 1988;319(6):343–347.
31. Labauge P, Brunereau L, Levy C, Laberge S, Houtteville JP. The natural history of familial cerebral cavernomas: a retrospective MRI study of 40 patients. *Neuroradiology*. 2000;42(5):327–332.
32. Del Curling O Jr, Kelly DL Jr, Elster AD, Craven TE. An analysis of the natural history of cavernous angiomas. *J Neurosurg*. 1991;75(5):702–708.
33. Knudson AG Jr. Mutation and cancer: statistical study of retinoblastoma. *Proc Natl Acad Sci U S A*. 1971;68(4):820–823.
34. Gault J, Shenkar R, Recksiek P, Awad IA. Biallelic somatic and germ line CCM1 truncating mutations in a cerebral cavernous malformation lesion. *Stroke*. 2005;36(4):872–874.
35. Shenkar R, et al. Advanced magnetic resonance imaging of cerebral cavernous malformations: part II. Imaging of lesions in murine models. *Neurosurgery*. 2008;63(4):790–797.
36. McDonald DA, et al. A novel mouse model of cerebral cavernous malformations based on the two-hit mutation hypothesis recapitulates the human disease. *Hum Mol Genet*. 2011;20(2):211–222.
37. Claxton S, Kostourou V, Jadeja S, Chambon P, Hodivala-Dilke K, Fruttiger M. Efficient, inducible Cre-recombinase activation in vascular endothelium. *Genesis*. 2008;46(2):74–80.
38. Davis GE, Camarillo CW. An alpha 2 beta 1 integrin-dependent pinocytic mechanism involving intracellular vacuole formation and coalescence regulates capillary lumen and tube formation in three-dimensional collagen matrix. *Exp Cell Res*. 1996;224(1):39–51.
39. Ghabrial A, Luschnig S, Metzstein MM, Krasnow MA. Branching morphogenesis of the Drosophila tracheal system. *Annu Rev Cell Dev Biol*. 2003;19:623–647.
40. Manning G, Krasnow MA. Development of the Drosophila tracheal system. In *The Development of Drosophila melanogaster*. Bate M, Martinez Arias A, eds. Plainview, New York, USA: Cold Spring Harbor Laboratory Press; 1993:609–685.
41. Mummery-Widmer JL, et al. Genome-wide analysis of Notch signalling in Drosophila by transgenic RNAi. *Nature*. 2009;458(7241):987–992.
42. Shiga Y, Tanaka-Matakatsu M, Hayashi S. A nuclear GFP/beta-galactosidase fusion protein as a marker for morphogenesis in living Drosophila. *Dev Growth Differ*. 1996;38(1):99–106.
43. Brand AH, Perrimon N. Targeted gene expression as a means of altering cell fates and generating dominant phenotypes. *Development*. 1993;118(2):401–415.
44. Dietzl G, et al. A genome-wide transgenic RNAi library for conditional gene inactivation in Drosophila. *Nature*. 2007;448(7150):151–156.
45. Clatterbuck RE, Eberhart CG, Crain BJ, Rigamonti D. Ultrastructural and immunocytochemical evidence that an incompetent blood-brain barrier is related to the pathophysiology of cavernous malformations. *J Neurol Neurosurg Psychiatry*. 2001;71(2):188–192.
46. Wang L, Seidman JG, Seidman CE. Narrative review: harnessing molecular genetics for the diagnosis and management of hypertrophic cardiomyopathy. *Ann Intern Med*. 2010;152(8):513–520.
47. He Y, et al. Stabilization of VEGFR2 signaling by cerebral cavernous malformation 3 is critical for vascular development. *Sci Signal*. 2010;3(116):ra26.
48. Navankasattusas S, et al. The netrin receptor UNC5B promotes angiogenesis in specific vascular beds. *Development*. 2008;135(4):659–667.
49. di Tomaso E, et al. PDGF-C induces maturation of blood vessels in a model of glioblastoma and attenuates the response to anti-VEGF treatment. *PLoS ONE*. 2009;4(4):e5123.
50. Jones CA, et al. Robo4 stabilizes the vascular network by inhibiting pathologic angiogenesis and endothelial hyperpermeability. *Nat Med*. 2008;14(4):448–453.
51. Saunders WB, Bayless KJ, Davis GE. MMP-1 activation by serine proteases and MMP-10 induces human capillary tubular network collapse and regression in 3D collagen matrices. *J Cell Sci*. 2005;118(pt 10):2325–2340.
52. Groth AC, Fish M, Nusse R, Calos MP. Construction of transgenic Drosophila by using the site-specific integrase from phage phiC31. *Genetics*. 2004;166(4):1775–1782.
53. Venken KJ, He Y, Hoskins RA, Bellen HJ. P[acman]: a BAC transgenic platform for targeted insertion of large DNA fragments in D. melanogaster. *Science*. 2006;314(5806):1747–1751.

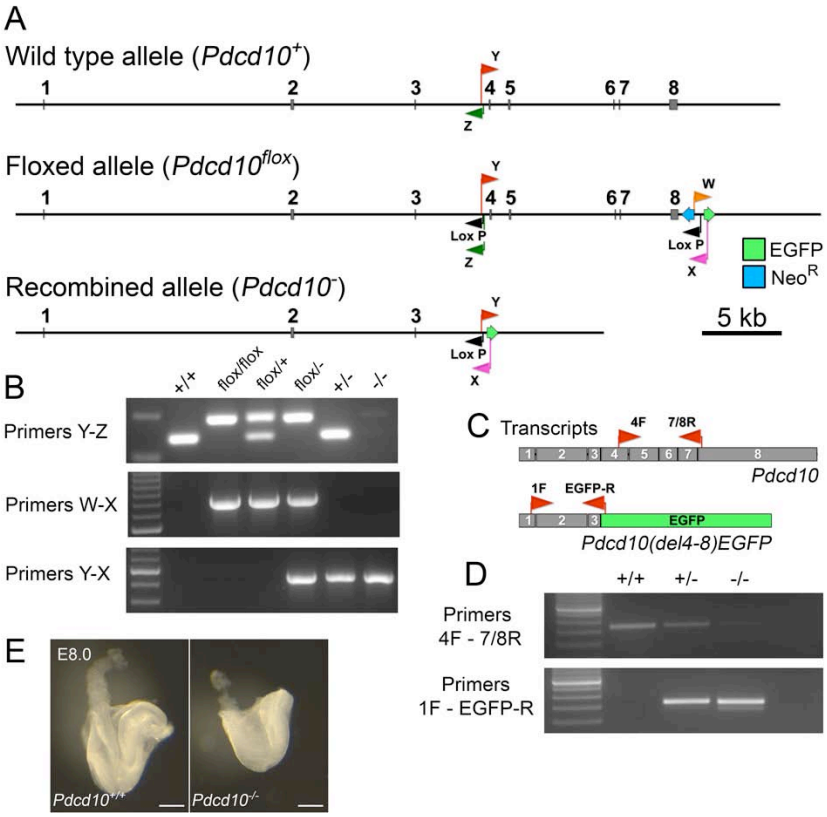

Supplemental Figure 1. Knockout design for *Pdcd10*. Ubiquitous deletion of *Pdcd10* results in early embryonic death. (**A**) Alleles of *Pdcd10* are shown. The floxed allele resulting from the targeting strategy includes loxP sites flanking exons 4-8 and places the enhanced green fluorescent protein (EGFP) in position to splice onto exon 3 in a fusion transcript resulting from the recombined allele. Genotyping primers are indicated by the letters W, X, Y and Z. (**B**) Genotyping by PCR using combinations of primers W, X, Y, and Z distinguishes the possible genotypes. (**C**) The wildtype and fusion transcripts are illustrated with exons outlined. The location of primers for RT-PCR are shown. (**D**) Results of RT-PCR performed on cDNA from embryos pooled by genotype that resulted from a mating of $Pdcd10^{+/-}$ vs. $Pdcd10^{+/-}$ mice. (**E**) Gross photos of E8.0 mouse embryos on dissection. Wildtype is shown in (**E**, left panel), *Pdcd10* knockout in (**E**, right panel). Even at this early stage, the knockout embryo has growth arrested and is smaller than its wildtype littermate. Scale bars = 200 μm.

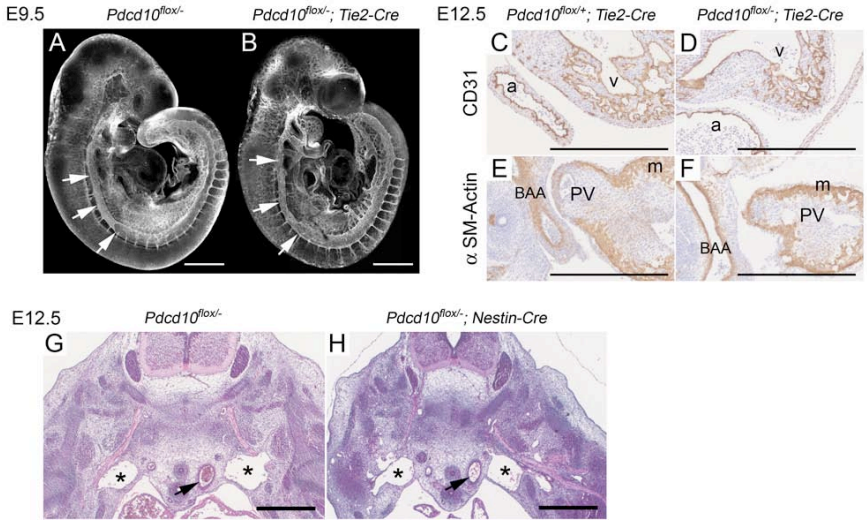

Supplemental Figure 2. Endothelial knockout of *Pdcd10* does not affect establishment of circulation or cardiac structure. Neural knockout of *Pdcd10* is viable. (**A-B**) Whole-mount fluorescent staining for CD31 in E9.5 *Pdcd10*$^{flox/-}$ (**A**) and *Pdcd10*$^{flox/-}$*; Tie2-Cre* (**B**) embryos. Arrows denote the dorsal aorta. (**C-D**) Hematoxylin and CD31 staining in E12.5 *Pdcd10*$^{flox/+}$*; Tie2-Cre* (**C**) and *Pdcd10*$^{flox/-}$*; Tie2-Cre* (**D**) embryos. (**E-F**) Hematoxylin and α-smooth muscle actin staining in E12.5 *Pdcd10*$^{flox/+}$*; Tie2-Cre* (**E**) and *Pdcd10*$^{flox/-}$*; Tie2-Cre* (**F**) embryos. a, atrium; v, ventricle; BAA, branchial arch artery; m, myocardium; PV, pulmonary valve. (**G-H**) Hematoxylin and eosin staining in E12.5 *Pdcd10*$^{flox/+}$*; Nestin-Cre* (**G**) and *Pdcd10*$^{flox/-}$*; Nestin-Cre* (**H**) embryos. Asterisks denote the cardinal veins. Arrows denote the dorsal aorta. Scale bars = 500 μm.

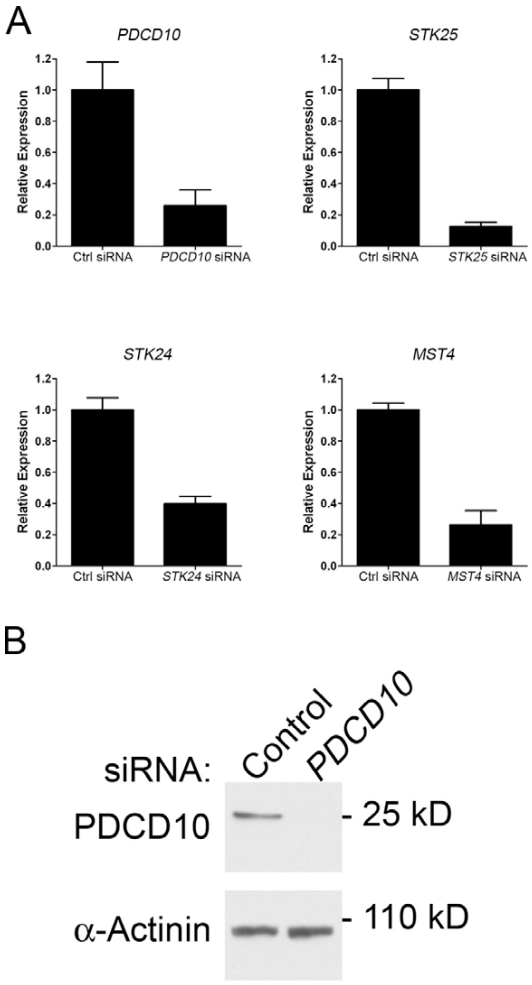

Supplemental Figure 3. siRNA effectively reduces levels of *PDCD10*, *STK25*, *STK24*, and *MST4*. (**A**) Quantitative PCR to detect *PDCD10*, *STK25*, *STK24*, and *MST4* was performed on cDNA made from the RNA of human endothelial cells to assess knockdown. (**B**) Western blot for PDCD10 to confirm knockdown.

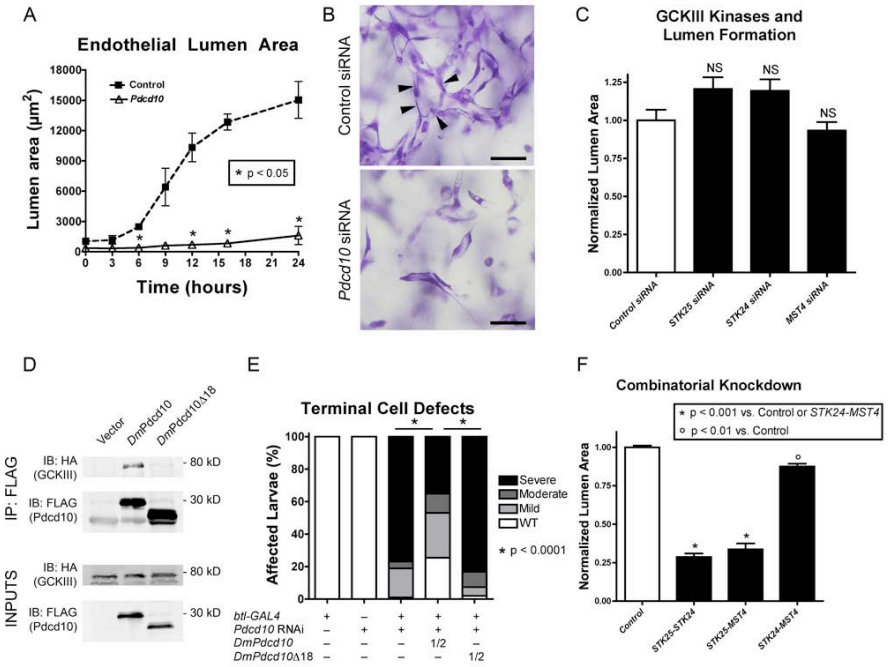

Supplemental Figure 4. Pdcd10 signals through GCKIII kinases in lumen formation. (**A**) Quantification of lumen area over time for human umbilical vein endothelial cells after treatment with *PDCD10* siRNA or control siRNA directed against Luciferase. (**B**) Toluidine blue staining of lumen formation assay. Lumens are shown with arrowheads. (**C**) Quantification of lumen area at 24 hours for cells treated with siRNA directed against each of the GCKIII kinases or Luciferase control (5 fields per time point in 3 independent experiments). (**D**) Immunoprecipitation for HA-tagged *Drosophila* GCKIII using full length *Drosophila* Pdcd10 (*Dm*Pdcd10) or *Drosophila* Pdcd10 with 18 amino acid deletion (*Dm*Pdcd10Δ18). Results are representative of 3 independent experiments. (**E**) Quantification of tracheal tube lumen formation defects in *Drosophila* with RNAi knockdown of *Pdcd10* with or without rescue constructs (N ≥ 64 for each genotype). Note: for rescue experiments only ~50% of all larvae contained the corresponding rescue transgene since they were generated by mating rescue heterozygous males (*btl-GAL4*, *UAS-GFP/+*; *UAS-Rescue/+*) to homozygous *UAS-RNAi* virgin females. (**F**) Quantification of 3D endothelial cell lumen area with combinatorial knockdown of human GCKIII kinases (5 fields per time point in 3 independent experiments). Data indicate mean ± SD. Scale bars = 50 μm.

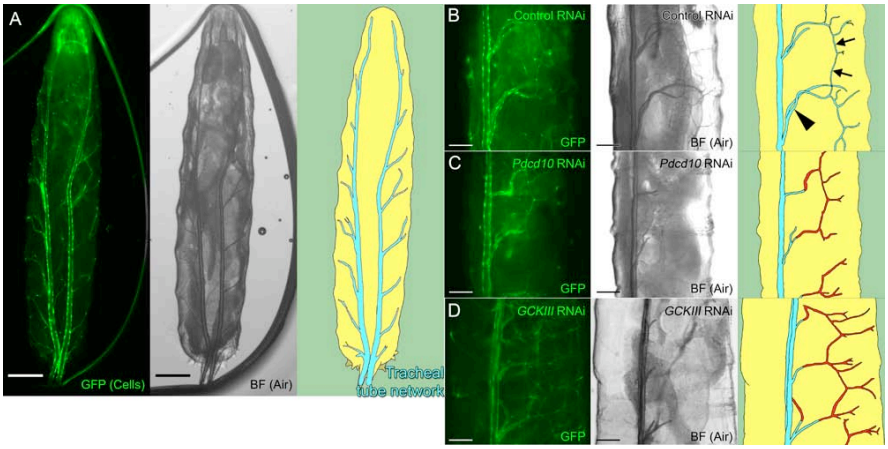

Supplemental Figure 5. Loss of Pdcd10 or GCKIII results in failure of tracheal tube lumenization in *Drosophila*. (**A**) The tracheal network of a *Drosophila* larva. A *UAS-GFP* transgene was used to label tracheal cells (left panel). Brightfield images of the same larva show air filling in lumens (middle panel). A cartoon representing the lumenized tube network (cyan) appears in the rightmost panel. (**B-D**) Tracheal tube lumen formation in flies expressing control RNAi (**B**), RNAi directed against *Pdcd10* (**C**), or RNAi directed against *GCKIII* (**D**) under the control of the tracheal-specific *btl-GAL4* driver. Arrowhead (in cartoon panel of **B**) indicates the primary trunk of a tracheal tube (where lumen truncation would indicate a severe phenotype), and arrows indicate the fine terminal branches (where lumen truncation would indicate a mild phenotype). Loss of *Pdcd10* or *GCKIII* results in similar air-filling defects. GFP expressing tracheal cells that lack air-filled lumens are outlined in red on the cartoon panels of **C-D**. Scale bars in (**A**) = 500 μm. Scale bars in (**B-D**) = 200 μm.

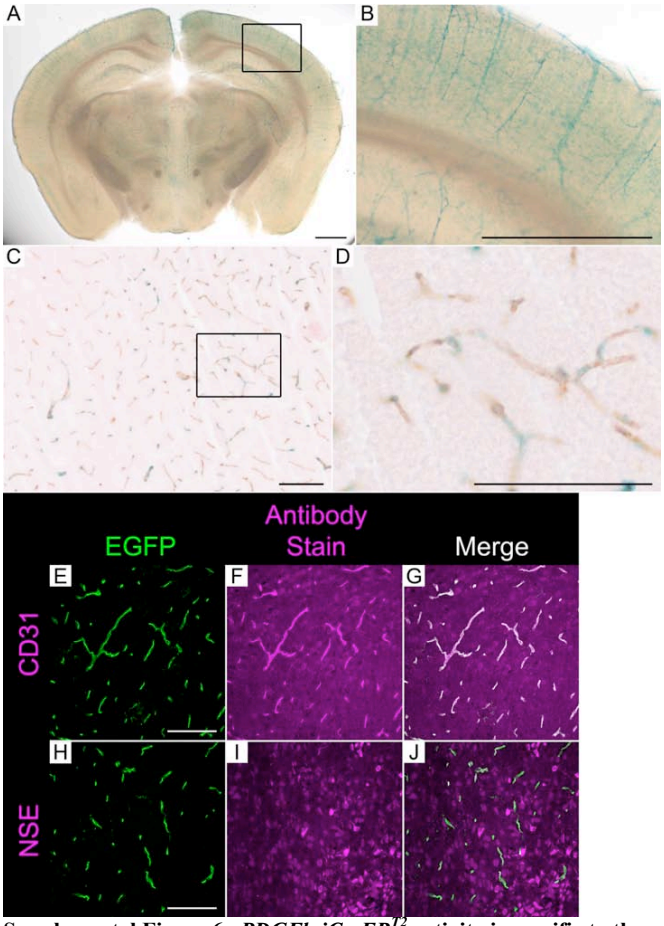

Supplemental Figure 6. *PDGFb-iCreER^{T2}* activity is specific to the endothelium. (**A**) X-gal staining (blue) of brain from a 6 month old *PDGFb-iCreER^{T2}; Rosa26-LacZ* mouse that was given tamoxifen at birth. (**B**) Close-up of the boxed area in panel (**A**). (**C-D**) X-gal (blue) and CD31 (brown) staining of brain from a 6 month old *PDGFb-iCreER^{T2}; Rosa26-LacZ* mouse that was given tamoxifen at birth. (**E-G**) CD31 (magenta) staining of brain from a 12 day old *PDGFb-iCreER^{T2}; Rosa26-ACTB-tdTomato,-EGFP* mouse that was given tamoxifen at birth. Cre activation converts ubiquitous tomato expression (not shown) to EGFP expression (green). (**H-J**) Neuron-specific enolase (NSE, magenta) staining of brain from a 12 day old *PDGFb-iCreER^{T2}; Rosa26-ACTB-tdTomato,-EGFP* mouse that was given tamoxifen at birth. Cre activation converts ubiquitous tomato expression (not shown) to EGFP expression (green). Scale bars in (**A-B**) = 1 mm. Scale bars in (**C-J**) = 100 μm.

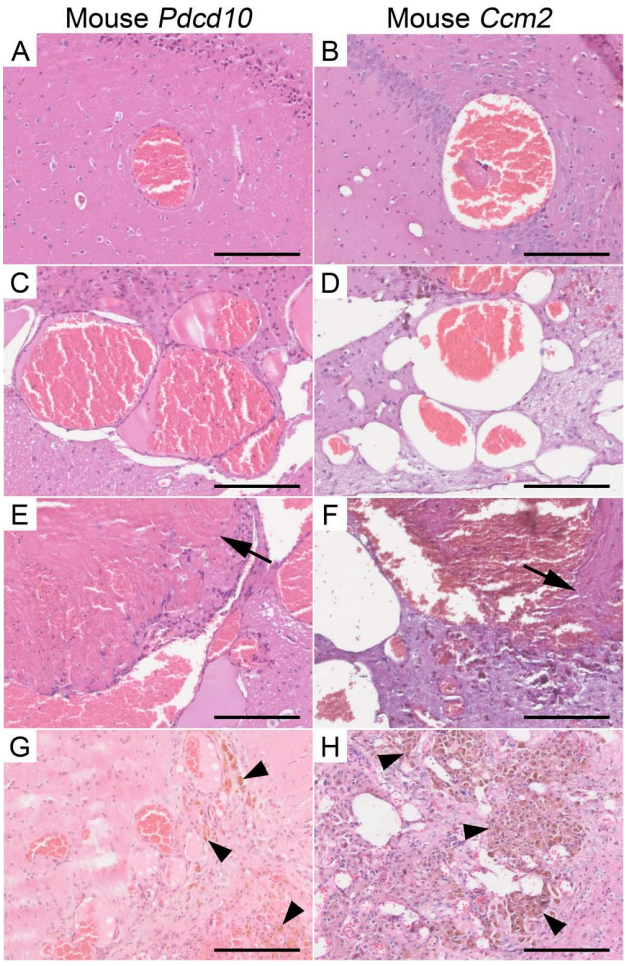

Supplemental Figure 7. LOH of either *Ccm2* or *Pdcd10* results in a range of vascular malformations. Both mouse models of CCM exhibit the same spectrum of pathology. Both the *Pdcd10* (**A**, **C**, **E**, and **G**) and *Ccm2* (**B**, **D**, **F**, and **H**) induced endothelial knockout models develop vascular lesions that exhibit the previously described spectrum of CCM pathology. Examples shown here include lesions consistent with solitary telangiectasias (**A-B**), multichannel "pristine" caverns (**C-D**), complex multichannel lesions with organizing thromboses (arrows in **E-F**), and multiple small caverns associated with heavy hemosiderin staining (arrowheads in **G-H**). Scale bars = 200 µm.

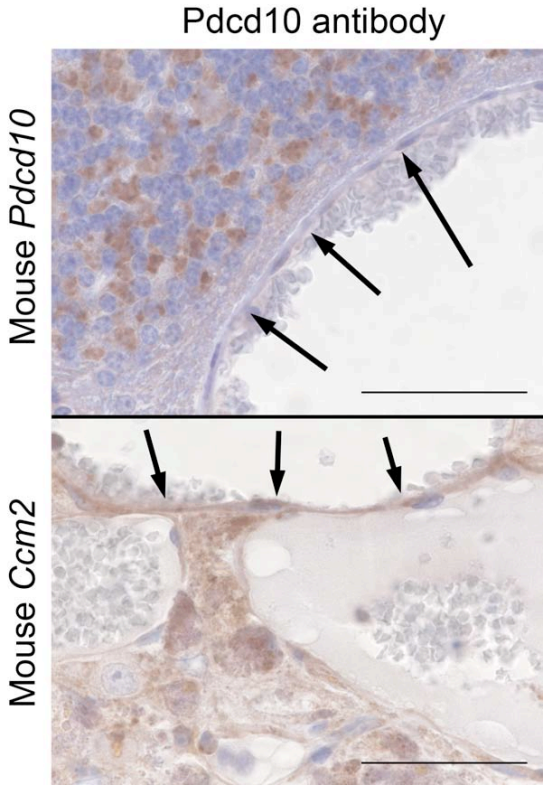

Supplemental Figure 8. Loss of Pdcd10 protein from *Pdcd10* (but not *Ccm2*) vascular lesions. An antibody against Pdcd10 does not stain endothelial cells of a CCM lesion from a *Pdcd10* induced knockout mouse (upper panel) but does stain the endothelial cells of a CCM from a *Ccm2* induced knockout mouse (bottom panel). Arrows indicate endothelial cells. Scale bars = 50 μm.

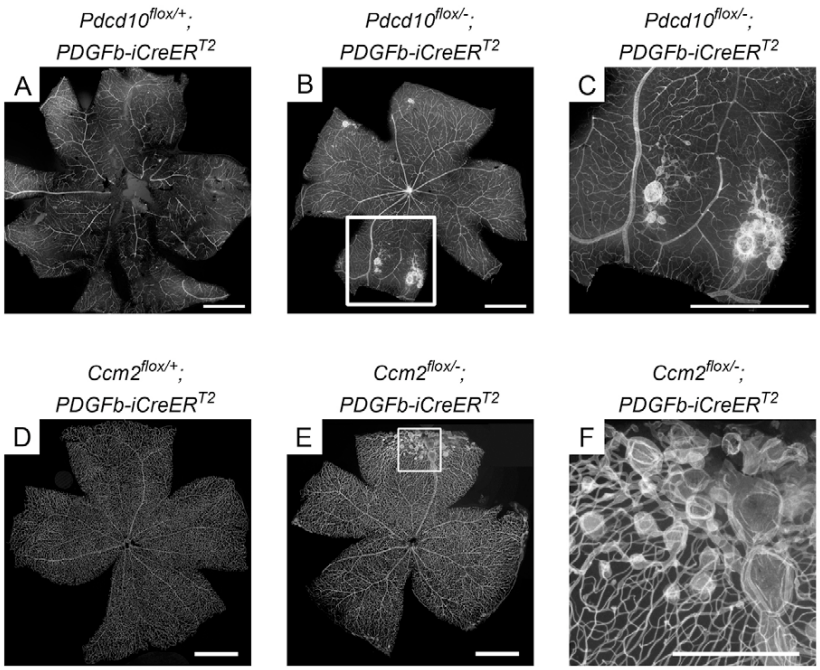

Supplemental Figure 9. Murine CCMs occur in the retinal vasculature. Lectin stained retinal flat mounts from a 5 month old *Pdcd10$^{flox/+}$; PDGFb-iCreER^{T2}* mouse (**A**), a 5 month old *Pdcd10$^{flox/-}$; PDGFb-iCreER^{T2}* mouse (**B-C**), a 7 month old *Ccm2$^{flox/+}$; PDGFb-iCreER^{T2}* mouse (**D**), and a 7 month old *Ccm2$^{flox/-}$; PDGFb-iCreER^{T2}* mouse (**E-F**). All mice were given tamoxifen at birth. (**C**) Close-up of the boxed, CCM-containing area in (**B**). (**F**) Close-up of the boxed, CCM-containing area in (**E**). Scale bars for all panels = 1 mm, except for panel (**F**), which is 500 μm.

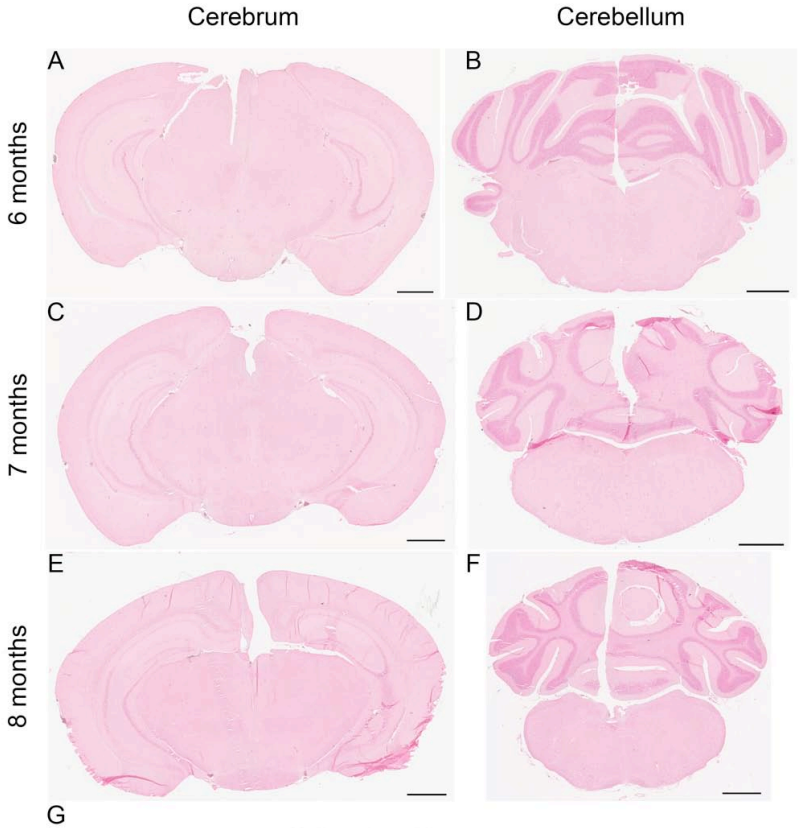

G

$Ccm2^{flox/-}$	CCM postive	CCM negative	Total
Nestin-Cre	0	6	6
PDGFb-iCreER^{T2}	16	0	16
Total	16	6	22

Fisher's exact test – $p < 0.0001$

Supplemental Figure 10. Neural-specific deletion of *Ccm2* does not result in CCMs. (**A-F**) Histology of *$Ccm2^{flox/-}$; Nestin-Cre* mouse brain at 6 months (**A-B**), 7 months (**C-D**), and 8 months (**E-F**). Staining is Prussian blue for hemosiderin with nuclear fast red counterstain. No lesions are found in these brains, and no hemosiderin is apparent. Scale bars = 1 mm. (**G**) Table comparing prevalence of CCMs in neural knockout (*Nestin-Cre*) vs. inducible endothelial knockout (*PDGFb-CreER^{T2}*).

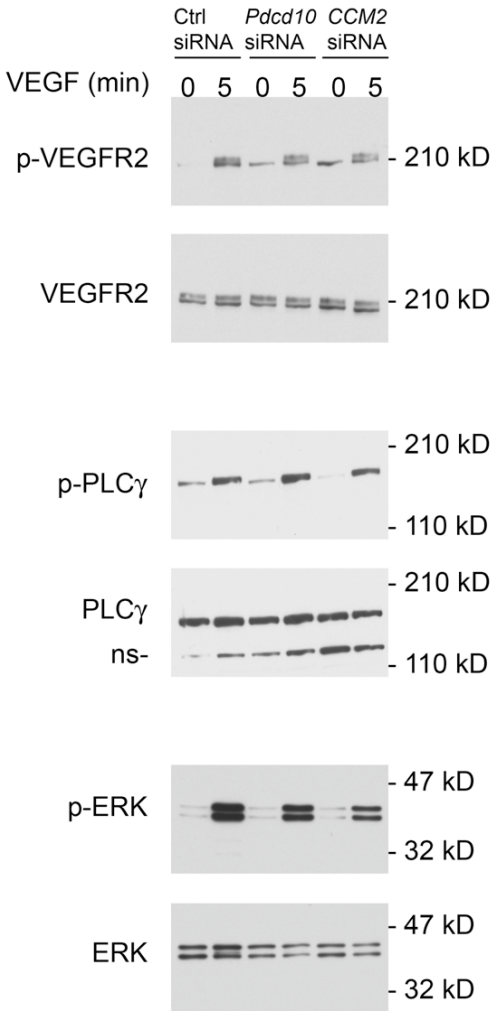

Supplemental Figure 11. Loss of PDCD10 does not affect VEGFR2-MAPK signaling. Western blot for VEGFR2, PLCγ, and ERK1/2 phosphorylation after stimulation of HMVECs with 10 ng/mL VEGF for the indicated amounts of time. ns, non-specific band.

Cross	*Pdcd10*$^{flox/flox}$ X *Pdcd10*$^{+/-}$; *Nestin-Cre*			
Genotype	*Pdcd10*$^{flox/+}$	*Pdcd10*$^{flox/-}$	*Pdcd10*$^{flox/+}$; *Nestin-Cre*	*Pdcd10*$^{flox/-}$; *Nestin-Cre*
# of progeny				
E12.5	2	7	9	8
P1	12	17	7	7

Supplemental Table 1. Table showing numbers of living offspring by genotype in matings between *Pdcd10*$^{flox/flox}$ and *Pdcd10*$^{+/-}$*; Nestin-Cre* parents.

CHAPTER 6

SUMMARY AND CONCLUSIONS

The *Drosophila* larval tracheal system is composed of approximately 10,000 interconnected tubes that serve to transport oxygen and other gases throughout the body. In order to achieve this complete interconnectivity, the tracheal system must first undergo extensive branching and fusion steps that begin during embryogenesis and continue throughout larval development (Samakovlis et al., 1996). The genes involved in mediating these processes may also control similar processes seen in other organisms. A forward genetic screen of the X chromosome was previously conducted to isolate lethal mutations affecting branching and lumen formation in tracheal terminal cells (Metzstein and Krasnow, unpublished results). Tracheal terminal cells are specialized cells that undergo subcellular branching and tubulogenesis, and are responsible for transporting gases and exchanging gases in hypoxic tissues (Jarecki et al., 1999). Thirty-two lines with mutations affecting different aspects of branching and lumen formation were identified. Of these thirty-two, we focused on five lines in which terminal cells undergo essentially normal branching, but are unable to generate a functional lumen.

Our mapping and sequencing data allowed us to identify specific candidate genes. Some of these genes may use known cellular processes that are thought to regulate lumen formation, while other candidates represent unknown functions.

Mapping experiments have also allowed for the identification and molecular cloning of one causative gene as *Zpr1* (*Zinc-finger protein 1*), an evolutionarily conserved protein characterized by two C4 zinc fingers and two conserved homology domains. We show here that Zpr1 is required for lumenogenesis in terminal cells, and is also involved in regulating branch outgrowth.

Zpr1 was initially identified as a protein that was able to bind the intracellular tail of the inactive EGFR (Galcheva-Gargova et al. 1996). The EGFR has previously been shown to be involved early in tracheal cell migration, and is necessary for maintaining the structural of the tracheal system, but specific downstream effectors have not been identified in the tracheal system (Cela and Llimargas, 2006; Nishimura et al., 2007). We show by epistasis experiments as well as in our air-filling assay, that mutations in the *EGFR* phenocopy *Zpr1* lumenless mutants. To our knowledge, this is the first *in vivo* evidence that demonstrates that Zpr1 functions downstream of the EGFR, and that Zpr1 activity is required for a specific developmental process. We have yet to show whether there is a direct physical interaction between Zpr1 and the FGFR, but we show that that Zpr1 lies downstream of the FGFR, a previously uncharacterized interaction.

Consistent with out data that Zpr1 lies downstream of multiple RTKs, we show that the null mutations in the two receptor tyrosine phosphatases (RPTPs) expressed in tracheal system result in excessive cytoplasmic outgrowth and lumenless cells (Jeon and Zinn, 2009). This result on its own may be interpreted as an indication that these RPTPs are not very specific and may be affecting other RTKs. Combining our genetic evidence showing that multiple RTKs ar feeding into the Zpr1 pathway with the previous data supporting a negative regulation by RPTPs, a more complex signaling cascade arises.

The finding that Zpr1 lies downstream of multiple RTKs allows us to propose a model that provides the cell with a method for interpreting various positional cues that help the cell determine whether it has reached hypoxic target tissue. In our model, hypoxic tissue secreting FGF serves as a long-range signaling molecule that instructs the outgrowth and active migration of terminal cells towards hypoxic tissue. Hypoxic tissue then secretes EGF as a short-range signaling molecule that induces lumen formation. Since lumen formation is an important step in mediating gas exchange between hypoxic tissue, the possible cross talk or redundancy between the FGFR and EGFR signaling cascades provide the cell with both, a fail safe that can ensure lumen formation occurs as well as an alternative method for modifying the amount of lumenogenesis that occurs during hypoxic conditions.

Evidence also shows that upon EGFR activation, Zpr1 can interact with the eukaryotic translation elongation factor 1A (eEF1A) or bind multiprotein complexes formed by the survival motor neurons 1 (SMN1) protein and that both of these interactions result in the redistribution and nuclear accumulation of Zpr1 (Gangwani, et al., 1998; Galcheva-Gagova et al., 1998). We show that RNAi knockdown of the two other known Zpr1 binding partners eEf1α and SMN1 also result in lumenless terminal cells. These results support previously published reports suggesting that FGFR is a genetic modifier of *smn* mutants, and its over-expression may be sufficient to bypass mutations in *smn*.

We have now generated some of the tools that will allow us to investigate the downstream effects of Zpr1 and begin to address its specific role in the nucleus. The generation of tagged versions of Zpr1 will allow us to investigate changes in its

subcellular localization in response to different genetic insults. Specifically it will be interesting to test whether over-expression of Zpr1is able to rescue mutations in *smn in vivo* and whether this is can be controlled by FGF signaling. Altogether we have constructed the genetic tools necessary to answer long-standing questions in the SMA field. It remains to be seen if our lumenless terminal cell phenotype adequately recapitulates the known phenotypes of *Zpr1* loss-of-function mutations in mammalian systems, although it may still provide an *in vivo* system for studying these important interactions.

References

Cela, C., and M. Llimargas (2006). Egfr is essential for maintaining epithelial integrity during tracheal remodeling in Drosophila. Development *133*, 3115-3125.

Galcheva-Gargova, Z., et al. (1996). Binding of zinc finger protein ZPR1 to the epidermal growth factor receptor. Science *21*, 1797-802.

Galcheva-Gargova, Z., et al. (1998). The cytoplasmic zinc finger protein ZPR1 accumulates in the nucleolus of proliferating cells. Molecular Biology of the Cell *9*, 2963-2971.

Gangwani, L., R. Flavell and R.J. Davis (1998). Interaction of ZPR1 with translation elongation factor1-alpha in proliferating cells. Journal of Cell Bio *143*, 1471-1484.

Jarecki, J., et al. (1999). Oxygen regulation of airway branching in Drosophila is mediated by branchless FGF. Cell *99*, 211-20.

Jeon, M., and K. Zinn (2009). Receptor tyrosine phosphatases control tracheal tube geometries through negative regulation of EGFR signaling. Development *136*, 3121-3129.

Samakovlis, C., et al. (1996). Development of the Drosophila tracheal system occurs by a series of morphologically distinct but genetically coupled branching events. Development *122*, 1395-407.

Sen, A., et al., (2011) Modeling spinal muscular atrophy in Drosophila links smn to FGF signaling. JCB *192*, 481-495.